Susceptibilities in materials with multiple strongly correlated orbitals

Dissertation

zur Erlangung des Doktorgrades

des Fachbereiches Physik
an der Fakultät für Mathematik, Informatik
und Naturwissenschaften
der Universität Hamburg

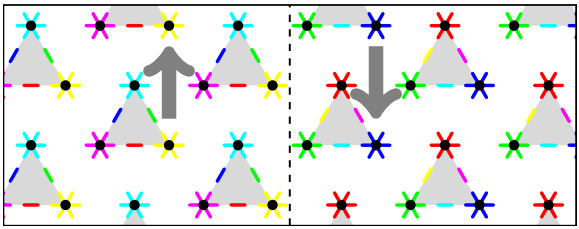

vorgelegt von

Lewin Volker Boehnke

Hamburg
2015

Gutachter der Dissertation:	Dr. Frank Lechermann Prof. Dr. Alexander Lichtenstein Prof. Dr. Xi Dai
Gutachter der Disputation:	Dr. Frank Lechermann Prof. Dr. Michael Potthoff
Datum der Disputation: 28.10.2014	
Vorsitzende des Prüfungsausschusses:	Prof. Dr. Daniela Pfannkuche
Vorsitzende des Promotionsausschusses:	Prof. Dr. Daniela Pfannkuche
Dekan der Fakultät für Mathematik, Informatik und Naturwissenschaften:	Prof. Dr. Heinrich Graener

Kurzfassung

Die Arbeit, die in dieser Dissertation vorgestellt wird, hebt die Anwendbarkeit der Bestimmung und die Interpretation der Gittersuszeptibilitäten in stark korrelierten Materialien auf das Niveau, das auch der Dynamischen Molekularfeldtheorie, unterstützt durch moderne zeitkontinuierliche Quantum Monte Carlo Algorithmen, zugänglich ist.

Numerische Mittel werden vorgestellt, um diese Berechnungen für mehrorbitalige Modelle zu ermöglichen und Interpretationen des resultierenden allgemeinen Frequenz- und Wellenzahlvektor-abhängigen orbitalen Suszeptibilitätstensors werden im Hinblick auf experimentell beobachtbare Größen und auf intern fluktuiernde Moden diskutiert.

Dies wird angewandt auf verschiedene reale Systeme, um die orbitalen Beiträge zu der Spin Suszeptibilität an inkommensurablen Wellenvektoren in Sr_2RuO_4, den Übergang des Charakters der magnetischen Suszeptibilität mit Dotierung in Na_xCoO_2 und die nichtlokalen Ordnungsfluktuationen des $\sqrt{3}\times\sqrt{3}$ Gitter-Reorganisationsübergangs in $LiVS_2$ zu diskutieren.

Abstract

The work presented in this thesis elevates the applicability of the calculation and interpretations of lattice susceptibilities of strongly correlated materials to a similar ground as that accessible to dynamical mean field theory supplemented with modern continuous time quantum Monte Carlo algorithms.

Numerical means are introduced to facilitate these calculations for multiorbital models and interpretations of the resulting general frequency and wave vector dependent orbital tensor susceptibility are discussed in terms of experimental observables and intrinsic fluctuating modes.

Subsequently, these are applied to several realistic materials, to discuss orbital contributions to the incommensurate spin susceptibility peaks in Sr_2RuO_4, the cross-over of magnetic excitation character with doping in Na_xCoO_2 and the non local order fluctuations of the $\sqrt{3}\times\sqrt{3}$ lattice reconstruction transition in $LiVS_2$.

Contents

1 Preface **9**

2 Theoretical framework **13**
2.1 On linear response 13
2.2 Lattice susceptibilities from a local approximation . . . 18

Peer reviewed work: Orthogonal polynomial representation of imaginary-time Green's functions 22

2.3 On the CT-Hyb algorithm 36

3 Susceptibilities **39**
3.1 Extracting dominant contributions to the susceptibility tensor 40
3.2 The simple case of one orbital per site 41

4 Incommensurate spin susceptibility in Sr_2RuO_4 **43**
4.1 Numeric setup for Sr_2RuO_4 46
4.2 An addendum to the use of Legendre coefficients - Shifting frequencies 46
4.3 Dynamical spin susceptibility spectrum for Sr_2RuO_4 . . 56
4.4 Orbital contributions to the spin susceptibility 58
4.5 Outlook 62

5 Ordering tendencies on the square Hubbard bilayer **65**

6 Lattice correlations and thermal properties of Na_xCoO_2 **73**

Peer reviewed work: Competing orders in Na_xCoO_2 from strong correlations on a two-particle level 76

Invited article: Getting back to Na_xCoO_2: Spectral and thermoelectric properties 82

7 Hidden spin-orbital hexagonal ordering induced by strong correlations in $LiVS_2$ **89**

Preprint: Hidden spin-orbital hexagonal ordering induced by strong correlations in $LiVS_2$ 92

7.1 The fluctuation eigenbasis 100

8 Conclusion **105**

Appendix

A List of publications and author contributions **109**

Bibliography **113**

One

Preface

The term 'generalized' susceptibility is used with vastly different meanings throughout the different fields of condensed matter physics. While it is unambiguous that the susceptibility χ is the response of some observable to some applied force, with the probably easiest example being the response of the magnetization to an applied uniform static magnetic field, the notion of a 'generalization' thereof depends on what you consider standard.

Inelastic neutron scattering (INS) experiments highlight the wavevector $\mathbf{q}$ dependence of the spin susceptibility as *generalized*, as opposed to the uniform susceptibility ($\chi(\mathbf{q} = 0)$) available through e.g. measurements with a superconducting quantum interference device (SQUID) and the local susceptibility ($\sum_{\mathbf{q}} \chi(\mathbf{q})$) available from nuclear magnetic resonance (NMR) experiments.

In accordance with the notion that a generalized Hubbard model is one with several orbital degrees of freedom per site (which also is an ambiguous notation), a orbital tensor susceptibility χ_{ijkl} has been called a *generalized* susceptibility [Pav14]. This quantity describes the response of a very general field with two orbital degrees of freedom F_{lk} on an equally general expectation value and is too general to compare to experimental observables, yet contains those when traced out correctly.

When diagrammatic schemes for the calculation of susceptibilities are sought, it is necessary to also consider not only the 'traced out' quantity $\chi(\omega)$, but also the fermionic inner degrees of free-

dom (details in section 2.1). In that context, *generalized* is used [KL10, RVT12] to distinguish between the full three frequency susceptibility $\chi(\mathrm{i}\nu_n, \mathrm{i}\nu_{n'}, \mathrm{i}\omega_m)$ in fermionic ($\mathrm{i}\nu_n$, $\mathrm{i}\nu_{n'}$) and bosonic ($\mathrm{i}\omega_m$) Matsubara frequencies and the traced out, physical quantity $\chi(\mathrm{i}\omega_m)$.

While for model studies that target one specific of these aspects, an isolated, model based treatment might be sufficient, a physically sound description of strongly correlated multiorbital materials has to account for all those of the above mentioned properties that appear in the material at hand.

This work addresses all of the above, the most general susceptibility $\chi^{\sigma\sigma'}_{ijkl}(\mathbf{q}, \mathrm{i}\nu_n, \mathrm{i}\nu_{n'}, \mathrm{i}\omega_m)$ and adds one more possible meaning of what *generalized* means to this plethora by identifying the dominant contribution to this general susceptibility detached from experimental practicability, but enriched with insight about the nature of the inner fluctuations.

After establishing the toolbox necessary for the calculation and handling of this quantity in chapter 2, with special emphasize on a numerical advancement in its representation through Legendre polynomials in section 2.2, which greatly reduces the numerical expense and thus facilitates the calculations in the remainder of this work, a great part of this work thematizes the interpretation of such general quantities, by example or by careful analysis.

Starting in chapter 3, an interpretation of a multiorbital susceptibility is presented in terms of eigenmodes. This gives access to the internal fluctuations of a system dispatched from the existence of a corresponding experimental means of measurement.

In chapter 4, this is used to resolve the orbital contributions to the magnetic fluctuations of Sr_2RuO_4, revealing non-trivial behavior for different features throughout the Brillouin zone, of which the most prominent is a pronounced incommensurate peak in the spin susceptibility. Additionally, section 4.2 introduces a further numerical benefit for the calculation of dynamical susceptibilities by including knowledge about the structure of the fermionic degrees of freedom in the transformation. Determining the dynamical spin susceptibility of this

three-orbital model in a quality apt for analytic continuation would hardly be possible otherwise.

Chapter 5 discusses a simple two-orbital model. Its fluctuating modes are considered for illustrative purposes, giving a physical picture for all of them, thus establishing means of interpretation for the fourth rank spin-orbital susceptibility tensor.

This work climaxes in the thorough investigation of two further realistic strongly correlated materials, Na_xCoO_2 and $LiVS_2$.

The former, discussed in chapter 6, while being seemingly innocent with its one strongly correlated a_{1g}-like orbital per site, has a surprisingly rich multitudinousness of physical regimes, most of which will be addressed here, namely ferromagnetic correlation for low sodium doping, a temperature dependent cross-over to antiferromagnetic correlations for high doping that lead to an A-type antiferromagnetic phase at low temperatures, a large Seebeck coefficient with an unusual temperature dependence and a kagome charge ordering at $x = \frac{2}{3}$. Experimentally, many of these properties are only observed indirectly, e.g. the antiferromagnetic correlation at low doping by the Korringa ratio. The full $\mathbf{q}$ and ω dependence adds to the physical picture by clarifying the notion of 'antiferromagnetic' in this frustrated material along the doping x and even discovering an unprecedented excitation mode in the imaginary part of the dynamical K-point susceptibility at unusually high energy.

The latter, $LiVS_2$, which is discussed in chapter 7, shows fewer, yet more intricate physical effects, that really requires the whole 'general' susceptibility for a complete physical picture. Below $T \approx 310$K, a $\sqrt{3} \times \sqrt{3}$ reconstruction on the layered quasi two-dimensional triangular vanadium layers appears, described by an inherently nonlocal order parameter of vanadium t_{2g} orbitals. In a considerable numerical effort, this order parameter is unveiled.

Two

Theoretical framework

2.1 On linear response

Suppose a generalized force $\delta F'_\Delta(\mathbf{r},\tau)$ in space coordinates $\mathbf{r}'$ and imaginary time τ enters the Hamiltonian $\mathcal{H}$ by coupling to an operator $\delta\hat{X}'_\Delta(\mathbf{r},\tau)$.[1]

$$\mathcal{H} = \mathcal{H}_0 + \mathcal{H}_{\delta \mathrm{F}'_\Delta}, \qquad \mathcal{H}_{\delta F'_\Delta} = \int d\mathbf{r}\delta F'_\Delta(\mathbf{r},\tau)\delta\hat{X}'_\Delta(\mathbf{r},\tau)\ .$$

where $\mathcal{H}_0$ denotes the unperturbed Hamiltonian. $\delta\hat{X}(\mathbf{r},\tau) = \hat{X}(\mathbf{r},\tau) - \left\langle \hat{X}(\mathbf{r})\right\rangle_0$ and $\left\langle \cdots \right\rangle_0$ denotes the thermal expectation value in the absence of perturbation.

The simplest example is a (potentially staggered) magnetic field in z-direction ($\delta F'_\Delta(\mathbf{r},\tau) = H_z(\mathbf{r},\tau)$) that couples through the spin operator ($\delta\hat{X}'_\Delta(\mathbf{r}) = S^z(\mathbf{r})$). Within a linear response formulation, the effect on the deviation of an expectation value of a different operator $\hat{X}_\Gamma$ from its unperturbed reference point

$$\delta X_\Gamma(\mathbf{r},\tau) = \left\langle \hat{X}_\Gamma(\mathbf{r},\tau) - \left\langle \hat{X}_\Gamma(\mathbf{r},\tau)\right\rangle_0 \right\rangle$$

will depend on this generalized force $\delta F'_\Delta$ to linear order, which is a reasonable approximation to realistic materials as long as the generalized force is weak compared to the internal correlations of the system.

$$\delta X_\Gamma(\mathbf{r},\tau) = \int d\mathbf{r}'d\tau'\delta F'_\Delta(\mathbf{r}',\tau')\chi_{\Gamma\Delta}(\mathbf{r},\tau;\mathbf{r}',\tau') + \mathcal{O}(F'^2_\Delta) \qquad (2.1)$$

[1] The notations here loosely follow that of [AS10]

A very large part of this present work addresses the problem to determine these susceptibilities $\chi_{\Gamma\Delta}$ from microscopic considerations for realistically modeled strongly correlated materials and the question what physical insight can be gained from them once they are determined in a physically sound approximation.

To this end, it is worthwhile to note one implication already observable in equation (2.1). Later chapters will repeatedly deal with cases in which some susceptibility $\chi_{\Gamma\Delta}$ diverges when approaching a critical model parameter like interaction strength or temperature. In that cases, even an infinitesimal fluctuation in the generalized force $\delta F'_\Delta$ (which will always be present in a realistic surroundings) can lead to a sizable expectation value δX_Γ, hence the system can spontaneously develop an non-zero expectation value δX_Γ, indicating a phase transition.

The one-particle operators $\hat{X}_\Gamma(\mathbf{r},\tau)$ and $\hat{X}'_\Delta(\mathbf{r}',\tau')$ have the second quantized form

$$\begin{aligned}\hat{X}_\Gamma(\mathbf{r},\tau) &= \sum_{AB} c^\dagger_A(\mathbf{r},\tau) X^{(\Gamma)}_{AB} c_B(\mathbf{r},\tau) \\ \hat{X}'_\Delta(\mathbf{r}',\tau') &= \sum_{CD} c^\dagger_C(\mathbf{r}',\tau') X'^{(\Delta)}_{CD} c_D(\mathbf{r}',\tau') \ .\end{aligned} \tag{2.2}$$

The uppercase Latin indices denote some previously chosen one-particle basis, often indicating a set of quantum numbers, e.g. spin and orbital degree of freedom.

The action in Grassmann variables $\bar{c}$ and c

$$S[\delta F'_\Delta, \bar{c}, c] = S_0[\bar{c}, c] + \delta S[\delta F'_\Delta, \bar{c}, c]$$

consists of the unperturbed action S_0 and

$$\delta S'[F'_\Delta, \bar{c}, c] = \int d\tau \mathcal{H}_{\delta F'_\Delta} = \int d\mathbf{r}' d\tau' \delta F'_\Delta(\mathbf{r}',\tau') \delta \hat{X}'_\Delta(\mathbf{r}',\tau') \ .$$

To get the response of the expectation value

$$\delta X_\Gamma(\mathbf{r},\tau) = \mathcal{Z}^{-1} \int \mathcal{D}\left[\bar{c}, c\right] e^{-S_0} \delta \hat{X}_\Gamma(\mathbf{r},\tau) e^{-\int d\mathbf{r}' d\tau' \delta F'_\Delta(\mathbf{r}',\tau') \delta \hat{X}_\Delta(\mathbf{r}',\tau')}$$

to linear order in $\delta F'_\Delta$, compare

$$\begin{aligned}\delta X_\Gamma(\mathbf{r},\tau) =& \mathcal{Z}^{-1}\int \mathcal{D}\left[\bar{c},c\right] e^{-S_0}\delta\hat{X}_\Gamma(\mathbf{r},\tau)\\ &(1-\int d\mathbf{r}'d\tau'\delta F'_\Delta(\mathbf{r}',\tau')\delta X'_\Delta(\mathbf{r}',\tau')+\mathcal{O}(\delta F'^2_\Delta))\end{aligned}$$

to equation (2.1), which yields (with $\left\langle\delta\hat{X}_\Gamma\right\rangle_0 = 0$ by definition)

$$\begin{aligned}\chi_{\Gamma\Delta}(\mathbf{r},\tau,\mathbf{r}',\tau) =& -\left\langle\left(\hat{X}_\Gamma(\mathbf{r},\tau)-\left\langle\hat{X}_\Gamma\right\rangle_0\right)\left(\hat{X}'_\Delta(\mathbf{r}',\tau')-\left\langle\hat{X}'_\Delta\right\rangle_0\right)\right\rangle_0\\ =& -\left\langle\delta\hat{X}_\Gamma(\mathbf{r},\tau)\delta\hat{X}'_\Delta(\mathbf{r}',\tau')\right\rangle_0 . \qquad (2.3)\end{aligned}$$

Hereafter, within the linear response regime, all expectation values are evaluated in the unperturbed system and the corresponding index on the angle brackets will be dropped. In most cases of interest, the unperturbed expectation values $\left\langle\hat{X}_\Gamma\right\rangle$ and $\left\langle\hat{X}'_\Delta\right\rangle$ will be zero, e.g. when dealing with the magnetization $\hat{X} = S^z$ in a paramagnetic state.

Of more physical insight than the equation (2.3) is usually its Fourier transform

$$\chi_{\Gamma\Delta}(\mathbf{q},\mathrm{i}\omega_m) = \int d(\mathbf{r}-\mathbf{r}')d(\tau-\tau')e^{\mathrm{i}\mathbf{q}(\mathbf{r}-\mathbf{r}')}e^{\mathrm{i}\omega_m(\tau-\tau')}\chi_{\Gamma\Delta}(\mathbf{r}-\mathbf{r}',\tau-\tau')$$

where $\omega_m = 2m\pi T$ is a bosonic Matsubara frequency and use was made of the fact that for homogeneous materials with no explicit time-dependence of the Hamiltonian $\chi(\mathbf{r},\tau,\mathbf{r}',\tau') = \chi(\mathbf{r}-\mathbf{r}',\tau-\tau')$ depends on spatial- and (imaginary) time-differences only.

Numerical approaches (like the dynamical mean field theory (DMFT)-like approximation explained in section 2.2, which is used throughout this work) will produce an approximate expression for the general susceptibility tensor

$$\begin{aligned}\chi_{ABCD}(\mathbf{q},\mathrm{i}\omega_n) = -\int & d(\mathbf{r}-\mathbf{r}')d(\tau-\tau')e^{\mathrm{i}\mathbf{q}(\mathbf{r}-\mathbf{r}')}e^{\mathrm{i}\omega_n(\tau-\tau')}\\ &\left\langle\mathcal{T}_\tau c^\dagger_A(\mathbf{r},\tau)c_B(\mathbf{r},\tau)c^\dagger_C(\mathbf{r}',\tau')c_D(\mathbf{r}',\tau')\right\rangle .\end{aligned}$$

Specific susceptibilities like the spin susceptibility $\chi^{\mathrm{m}} = \langle S^z S^z \rangle$ or the charge susceptibility $\chi^{\mathrm{c}} = \langle \delta N \delta N \rangle$ ($\delta N = N - \langle N \rangle_0$ is the deviation of the occupation from its unperturbed value) can be obtained by using the corresponding operators through equation (2.2) and equation (2.3). This will be demonstrated explicitly for a simple case in the following. Later on, in chapter 3, a more conclusive way to resolve the relevant contributions to χ_{ABCD} will be presented.

But before coming to that, it is instructive to separate flavor- and index part of χ_{ABCD}. The notation with this separation is an ongoing source of trouble. The notation used throughout this work is that a *flavor* denotes a quantity conserved for each lattice site[2], in which the susceptibility is quadratic, while it is quartic in an *index*. A flavor will in all the cases discussed in this work be a spin and notation will accordingly be σ, but in certain cases also other quantum numbers may qualify. In cubic crystal symmetry for example, with an (somewhat artificial) electronic interaction of the type

$$\mathcal{H}_{\mathrm{int}} = U \sum_i n_{\uparrow i} n_{\downarrow i}$$

the susceptibility will also depend only quadratic on orbitals. In that case, an *flavor* will consist of a pair of spin- and orbital quantum numbers. In all cases discussed in this work however, spins will be the only quadratic dependence of the susceptibility and consequently, *flavor* will be used synonymously to *spin* and *index* synonymously to *orbital*.

The way the flavor part dependence reduces can be seen by writing the susceptibility tensor $\chi_{ABCD} = \chi_{i\,j\,k\,l}^{\sigma\sigma'\sigma''\sigma'''}$ as a matrix $\underline{\underline{\chi}}$ in super-indices $\binom{\sigma\sigma'}{i\,j}$ and $\binom{\sigma'''\sigma''}{l\,k}$ (Note the switched order in the second super-

[2]In a Hubbard model, e.g. the spin per site is not a conserved quantity, in a mean-field treatment however, it is.

index) which yields the structure[3]

$$\underline{\underline{\chi}} = \begin{array}{c} \\ \uparrow\uparrow \\ \downarrow\downarrow \\ \downarrow\uparrow \\ \uparrow\downarrow \end{array} \begin{array}{c} \begin{array}{cccc} \uparrow\uparrow & \downarrow\downarrow & \downarrow\uparrow & \uparrow\downarrow \end{array} \\ \begin{pmatrix} A1 & B1 & 0 & 0 \\ B2 & A2 & 0 & 0 \\ 0 & 0 & C1 & 0 \\ 0 & 0 & 0 & C2 \end{pmatrix} \end{array} .$$

The flavor part is explicitly noted (again the example used is for spins, but the arguments do not rely on that) and the elements are to be understood as blocks in $\{ij\}$ and $\{lk\}$. Several blocks are zero due to conservation of flavor, decoupling 'longitudinal' ($\sigma\sigma\sigma'\sigma'$) and 'transversal' ($\sigma\sigma'\sigma'\sigma$) part which thus justifies to treat those separately. This work focuses onto the longitudinal part, dropping one spin-index per super-index, e.g. using the shorthand notation $\chi^{\sigma\sigma'}_{ijkl} \equiv \chi^{\sigma\sigma\sigma'\sigma'}_{i\,j\,k\,l}$.

In a paramagnetic state, $A1 = A2$, $B1 = B2$, $C1 = C2$ and $A1 = A1^T$, $A2 = A2^T$, $B2 = B2^T$, $C1 = C1^T$, $C2 = C2^T$. Thus $\underline{\underline{\chi}}$ is not Hermitian in general but symmetric in the $\omega = 0$-case, where it is also real. Note how this matrix splits into smaller blocks

Touching ground again with experimentally observable susceptibilities, the magnetic susceptibility

$$\chi^{\mathrm{m}}(\mathbf{q} = \Gamma, \omega = 0) \equiv \frac{\partial \langle S^z \rangle}{\partial H_z}$$

will serve as an example for the orbital contributions to these. Here, the generalized force $\delta F'_\Delta(\mathbf{r}) = H_z$ couples to the magnetic moment $\delta \hat{X}'_\Delta(\mathbf{r}) = S^z$. Also, the variation in $\delta X_\Gamma(\mathbf{r}) = \langle S^z \rangle$ is sought.

In such a case the relevant concretion of the physical susceptibility

[3] Wave vector dependence and (Matsubara) frequency have been dropped in this structure discussion

$\chi^{\sigma\sigma'}_{ijkl}(\omega)$ is readily available from equation (2.3)

$$\chi^{\mathrm{m}}(\mathbf{q}, \mathrm{i}\omega_n) = \int d(\mathbf{r}-\mathbf{r}')d(\tau-\tau')e^{\mathrm{i}\mathbf{q}(\mathbf{r}-\mathbf{r}')}e^{\mathrm{i}\omega_n(\tau-\tau')}\left\langle \mathcal{T}_\tau S^z(\mathbf{r},\tau)S^z(\mathbf{r}',\tau')\right\rangle$$

$$= \frac{\hbar^2}{4}\Big\langle \mathcal{T}_\tau \sum_i (c^\dagger_{\uparrow i}c_{\uparrow i} - c^\dagger_{\downarrow i}c_{\downarrow i}) \sum_i (c^\dagger_{\uparrow i}c_{\uparrow i} - c^\dagger_{\downarrow i}c_{\downarrow i})\Big\rangle_{\mathbf{q},\mathrm{i}\omega_n} .$$

The second line introduces a shorthand notation for the Fourier transformation and includes the representation of the operators in line with equation (2.2).

E.g. for a two-orbital problem

$$\begin{aligned}\chi^{\mathrm{m}} = \quad & \chi^{\uparrow\uparrow}_{1111} + \chi^{\uparrow\uparrow}_{1122} + \chi^{\uparrow\uparrow}_{2211} + \chi^{\uparrow\uparrow}_{2222} \\ & -\chi^{\uparrow\downarrow}_{1111} - \chi^{\uparrow\downarrow}_{1122} - \chi^{\uparrow\downarrow}_{2211} - \chi^{\uparrow\downarrow}_{2222} \\ & -\chi^{\downarrow\uparrow}_{1111} - \chi^{\downarrow\uparrow}_{1122} - \chi^{\downarrow\uparrow}_{2211} - \chi^{\downarrow\uparrow}_{2222} \\ & +\chi^{\downarrow\downarrow}_{1111} + \chi^{\downarrow\downarrow}_{1122} + \chi^{\downarrow\downarrow}_{2211} + \chi^{\downarrow\downarrow}_{2222} ,\end{aligned}$$

which can be cumbersome but is straightforward.

2.2 Lattice susceptibilities from a local approximation

After the introduction of DMFT [MV89, GK92] and the introduction of the calculation of lattice susceptibilities [ZH90, Jar92] in a corresponding manner only very shortly after, several reviews have been given on both subjects [GKKR96, MJPH05, KSH+06], putting them well within the canon of available formalism for the investigation of strongly correlated materials and models.

Yet, while DMFT blossomed, only very few uses of a rigorous calculation of lattice susceptibilities through a local approximation to the irreducible vertex have been published (e.g. [Jar92, JMHM01,

MJPH05, HAH08]) and those that were addressed problems with one orbital per site only. Recently, a new wave of publications [HBR+08, BHR+08, LLM08] addressing susceptibilities in DMFT (and extensions thereof) appeared, when the two-particle Green's function was also identified as a vital ingredient in extensions around DMFT, such as dual fermion [RKL08, RKLG09] and the dynamical vertex approximation (DΓA) [TKH07] and thus doubled in that role.

Similarly, although most analytic properties of the two-particle Green's function and vertex have been long known [AGD75], a rigorous account of these properties for the use within DMFT and its extensions was not until very recently [RVT12].

Even fewer publications addressed rigorous DMFT susceptibilities in realistic materials [LLFH11, WLH+14]. Susceptibilities for a two-orbital model have been studied by Kuneš *et al.* [KA14]. They did so by separating the low- and high-frequency parts of the Bethe-Salpeter equation (BSE) and consider an asymptotic form for the latter [Kun11].

The manuscript [BHF+11], that is reprinted in the following, discusses the calculation of lattice susceptibilities in a DMFT-like local approximation and addresses the numerical challenges. It proposes an orthogonal Legendre-polynomial based basis for the numerical representation of the one- and two-particle Green's function and assesses their use on concrete examples.

Many subsequent work has directly profited from the use of this basis for DMFT calculations of various systems [DFM+12, GPPL12, HPW12, HWD12, HW12, KR12, KW12, NAAvdL12, FGKP13, SYŞ+13, HA13, XRvR+13, BGJV14, BL15, GAC14, HBS+14, HWW14, NA14, NSA14, SH14], while a widespread adoption of the Legendre basis for two-particle quantities has yet to happen. In this work, three publications that went this route will be discussed [BL12, BL14, BLKL14] and an additional two systems will be discussed in the following chapters. This will hopefully do away with the longstanding prejudice that such calculations are too cumbersome for realistic material focused applications.

Additionally, some works investigate further improvements and advantages of the representation of the Green's function also for cases other than its Monte Carlo accumulation. Huang and Du [HD12] investigated the use of integral kernels to filter fluctuations caused by the truncation in Legendre coefficients. This trades the property that the transformation between the polynomial basis and Matsubara frequencies is unitary for a faster converging expansion. While the unitarity of the transformation is analytically satisfactory, the expansion for the one-particle Green's function does not existencially rely on it. For the two-particle Green's function however, this approach is not applicable.

Arsenault *et al.* [ALBvLM14] benefited from the small number of parameters that carry already the full information about the one-particle Green's function, when applying machine learning methods to the Anderson impurity model.

An improvement for the Legendre basis for the calculation of dynamical susceptibilities will be discussed in section 4.2.

Orthogonal polynomial representation of imaginary-time Green's functions

Reprinted with permission from

L. Boehnke, H. Hafermann, M. Ferrero,
F. Lechermann, and O. Parcollet
Physical Review B **84**, 075145 (2011) (Editor's Suggestion).

The reference numbering used in this reprinted article is only valid within this specific article.

PHYSICAL REVIEW B **84**, 075145 (2011)

Orthogonal polynomial representation of imaginary-time Green's functions

Lewin Boehnke,[1] Hartmut Hafermann,[2] Michel Ferrero,[2] Frank Lechermann,[1] and Olivier Parcollet[3]
[1]*I. Institut für Theoretische Physik, Universität Hamburg, D-20355 Hamburg, Germany*
[2]*Centre de Physique Théorique, Ecole Polytechnique, CNRS, F-91128 Palaiseau Cedex, France*
[3]*Institut de Physique Théorique (IPhT), CEA, CNRS, URA 2306, F-91191 Gif-sur-Yvette, France*
(Received 16 April 2011; published 12 August 2011)

We study the expansion of single-particle and two-particle imaginary-time Matsubara Green's functions of quantum impurity models in the basis of Legendre orthogonal polynomials. We discuss various applications within the dynamical mean-field theory (DMFT) framework. The method provides a more compact representation of the Green's functions than standard Matsubara frequencies, and therefore significantly reduces the memory-storage size of these quantities. Moreover, it can be used as an efficient noise filter for various physical quantities within the continuous-time quantum Monte Carlo impurity solvers recently developed for DMFT and its extensions. In particular, we show how to use it for the computation of energies in the context of realistic DMFT calculations in combination with the local density approximation to the density functional theory (LDA+DMFT) and for the calculation of lattice susceptibilities from the local irreducible vertex function.

DOI: 10.1103/PhysRevB.84.075145 PACS number(s): 71.27.+a, 71.10.Fd

In recent years, significant progress has been made in the study of strongly correlated fermionic quantum systems with the development of methods combining systematic analytical approximations and modern numerical algorithms. The dynamical mean-field theory (DMFT) (for a review, see Ref. 1) and its various extensions[2–6] serve as successful examples for this theoretical advance. On the technical side, important progress was made in the solution of quantum impurity problems, i.e., local quantum systems coupled to a bath (self-consistently determined in the DMFT formalism). In particular, a new generation of continuous-time quantum Monte Carlo (CTQMC) impurity solvers[7–10] has emerged that provide unprecedented efficiency and accuracy (for a recent review, see Ref. 11).

In practice, several important technical issues still remain. First, while the original DMFT formalism is expressed in terms of single-particle quantities (Green's function and self-energy), two-particle quantities play a central role in the formulation of some DMFT extensions [e.g., dual fermions[4,12–14] and DΓA (Ref. 3)] and in susceptibility and transport computations in DMFT itself. They typically depend on three independent times or frequencies, and spatial indices. Therefore, they are quite large objects that are hard to store, manipulate, and analyze, even with modern computing capabilities. Developing more compact representations of these objects and using them to solve, e.g., the Bethe-Salpeter equations is therefore an important challenge.

A natural route is to use an orthogonal polynomial representation of the imaginary-time dependence of these objects. While the application of orthogonal polynomials has had productive use in other approaches to correlated electrons,[15,16] in this paper we show how to use Legendre polynomials to represent various imaginary-time Green's functions in a more compact way and show their usefulness in some concrete calculations.

A second aspect is that modern CTQMC impurity solvers still have limitations. One well-known problem is the high-frequency noise observed in the Green's function and the self-energy (see, e.g., Fig. 6 of Ref. 17). Even though this is in general of little concern for the DMFT self-consistency itself, it can become problematic when computing the energy, since the precision depends crucially on the high-frequency expansion coefficients of the Green's function and self-energy. An important field of application involves realistic models of strongly correlated materials in through the combination with the local density approximation (LDA+DMFT).[18] In this paper, we show that physical quantities such as the Green's function, kinetic energy, and even the coefficients of the high-frequency expansion of the Green's function can be measured directly in the Legendre representation within CTQMC, and that the basis truncation acts as a very efficient noise filter: the statistical noise is mostly carried by high-order Legendre coefficients, while the physical properties are determined by the low-order coefficients.

This paper is organized as follows: Section I is devoted to single-particle Green's functions. More precisely, in Sec. I A, we introduce the Legendre representation of the single-particle Green's function and how it appears in the CTQMC context; we then illustrate the method on the imaginary-time (Sec. I B) and imaginary-frequency (Sec. I C) Green's function of a standard DMFT computation; in Sec. I D, we discuss the use of the Legendre representation to compute the energy in a realistic computation for $SrVO_3$. Section II is devoted to two-particle Green's functions: We first present the expansion in Sec. II A and illustrate it on an explicit DMFT computation of the antiferromagnetic susceptibility in Sec. II B, followed by the example of a calculation of the dynamical wave-vector resolved magnetic susceptibility. Additional information can be found in the appendixes. Appendix A gives some properties of the Legendre polynomials relevant for this work. Appendix B discusses the rapid decay of the Legendre coefficients of the single-particle Green's function. Appendix C first derives the accumulation formulas for the single-particle and two-particle Green's functions in the hybridization expansion CTQMC (CT-HYB) algorithm[8] (while these formulas have been given before,[8,17] the proof presented here aims to explain their resemblance to a Wick's theorem). We then give the explicit formulas in the Legendre basis. For completeness, we provide an accumulation formula for the continuous-time interaction expansion (CT-INT)[7] and

auxiliary field (CT-AUX)[10] algorithms in Appendix D. Finally, in Appendix E, we derive the expression for the matrix that relates the coefficients of the Green's function in the Legendre representation to its Matsubara frequency representation.

I. SINGLE-PARTICLE GREEN'S FUNCTION

A. Legendre representation

We consider the single-particle imaginary-time Green's function $G(\tau)$ defined on the interval $[0,\beta]$, where β is the inverse temperature. Expanding $G(\tau)$ in terms of Legendre polynomials $P_l(x)$ defined on the interval $[-1,1]$, we have

$$G(\tau) = \sum_{l\geqslant 0} \frac{\sqrt{2l+1}}{\beta} P_l[x(\tau)]\, G_l, \tag{1}$$

$$G_l = \sqrt{2l+1} \int_0^\beta d\tau\, P_l[x(\tau)]\, G(\tau), \tag{2}$$

where $x(\tau) = 2\tau/\beta - 1$ and G_l denotes the coefficients of $G(\tau)$ in the Legendre basis. The most important properties of the Legendre polynomials are summarized in Appendix A.

We note that *a priori* different orthogonal polynomial bases (e.g., Chebyshev instead of Legendre polynomials) may be used, and many of the conclusions in this paper would remain valid. The advantage of the Legendre polynomials is that the transformation between the Legendre representation and the Matsubara representation can be written in terms of a unitary matrix, since Legendre polynomials are orthogonal with respect to a scalar product that does not involve a weight function (see below and Appendix E). In this paper, therefore, we restrict our discussion to the Legendre polynomials.

On general grounds, one can expect the Legendre representation of $G(\tau)$ to be *much more compact than the standard Matsubara representation*: in order to perform a Fourier series expansion in terms of Matsubara frequencies, $G(\tau)$ has to be antiperiodized for all $\tau \in \mathbb{R}$, while the full information is already contained in the interval $[0,\beta]$. As a result, the Green's function contains discontinuities in τ that result in a slow decay at large frequencies (typically $\sim 1/\nu_n$). On the other hand, expanding $G(\tau)$, which is a smooth function of τ on the interval $[0,\beta]$, in terms of Legendre polynomials yields coefficients G_l that decay faster than the inverse of any power of l (as shown in Appendix B). As a result, the information about a Green's function can be saved in a very small storage volume. As we will show in Sec. II, this is particularly relevant when dealing with more complex objects such as the two-particle Green's function, which depends on three frequencies.

CTQMC algorithms usually measure the Green's function $G(\tau)$ in one of the two following ways: (i) using a very fine grid for the interval $[0,\beta]$ or (ii) measuring the Fourier transform of the Green's function on a finite set of Matsubara frequencies.[7,19] We show in Appendix C explicitly for the CT-HYB[8,11] algorithm that one can also directly measure the coefficients G_l during the Monte Carlo process (we expect our conclusions to hold for any continuous-time Monte Carlo algorithm).

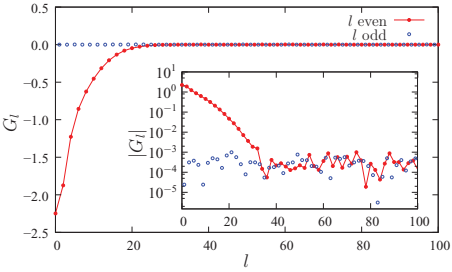

FIG. 1. (Color online) Legendre coefficients G_l of the Green's function of the half-filled Hubbard model on the Bethe lattice within DMFT. Error bars are not shown on the logarithmic plot. They are of the order of 10^{-4}.

As an illustration, we will focus on the Green's function obtained by DMFT for the Hubbard model at half-filling described by the Hamiltonian

$$H = -t \sum_{\langle ij\rangle\sigma} c_{i\sigma}^\dagger c_{j\sigma} + U \sum_i n_{i\uparrow}\, n_{i\downarrow}, \tag{3}$$

where $c_{i\sigma}^{(\dagger)}$ creates (annihilates) an electron with spin σ on the site i of a Bethe lattice,[1,20] and $\langle ij\rangle$ on the sum denotes nearest neighbors. In the following, quantities will be expressed in units of the hopping t, and we set the on-site Coulomb repulsion to $U/t = 4$ and use the temperature $T/t = 1/45$. We solve the DMFT equations using the TRIQS[21] toolkit and its implementation of the CT-HYB[8,11] algorithm. In Fig. 1, we show the coefficients G_l that we obtain. Note that coefficients for l odd must be zero due to particle-hole symmetry. Indeed, the coefficients in our data for odd l's all take on a very small value, compatible with a vanishing value within their error bars. The even l coefficients instead show a very fast decay, as discussed above. For $l > 30$, all coefficients eventually take values of the order of the statistical error bar.

Let us now discuss the specific issue of the statistical Monte Carlo noise. We observe that the high-order Legendre coefficients have a larger relative noise than small l coefficients. On general grounds, we expect the coefficients of the *exact* Green's function to continue to decrease faster than any power of $1/l$ to zero (cf. Appendix B). Hence, physical quantities computed from $G(\tau)$ are likely to have a very weak dependence on the G_l for large l. A good approximation then is to truncate the expansion in Legendre polynomials at an order $l_{\max}$ and set $G_l = 0$ for $l > l_{\max}$. The choice for $l_{\max}$ has to be such that the quantity of interest is accurately represented. On the other hand, if $l_{\max}$ is too large, we would start to include coefficients that have increasingly large error bars compared to their value, and this would eventually pollute the calculation. A systematic method is therefore to examine the physical quantity as a function of the cutoff $l_{\max}$. We expect that it will first reach a plateau where it is well converged. The existence of a plateau means that the contribution of higher-order coefficients is indeed negligible. For larger $l_{\max}$, the statistical noise in the G_l will destabilize this plateau, whose size will increase with the precision of the CTQMC computation. The existence of such

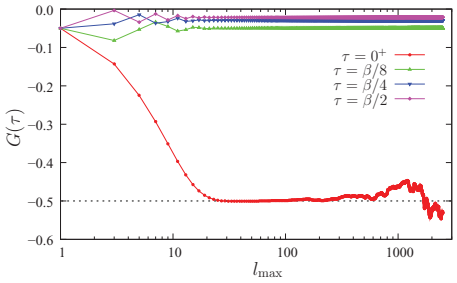

FIG. 2. (Color online) Imaginary-time Green's function $G(\tau)$ at four different values of τ as a function of $l_{\max}$.

a plateau provides a controlled way to determine the adequate value of $l_{\max}$. In the remaining paragraphs of this section, we will illustrate this phenomenon on different physical quantities by studying their dependence on $l_{\max}$.

B. Imaginary-time Green's function

It is instructive to analyze the effect of $l_{\max}$ on the reconstructed imaginary-time Green's function $G(\tau)$ [using Eq. (1)]. In Fig. 2, we show the evolution of $G(\tau)$ at $\tau = 0^+$, $\tau = \beta/8$, $\tau = \beta/4$, and $\tau = \beta/2$ with the cutoff. It is apparent that these values very rapidly converge as a function of $l_{\max}$. We observe a well-defined and extended plateau. As the cutoff grows bigger, noise reappears in $G(\tau)$ because of the comparatively large error bars in higher-order G_l's.

In Fig. 3, the Green's function is reconstructed on the full interval $[0,\beta]$ and compared to a direct measurement on a 1500-bin mesh. For $l_{\max} = 20$, where the individual values of $G(\tau)$ have not yet converged to their plateau (see Fig. 2), the resulting Green's function is smooth but not compatible with the scattered direct measurements. For $l_{\max} = 35$ and 60, $G(\tau)$ is smooth and nicely interpolates the scattered data. Moreover, $G(\tau)$ is virtually identical for both values of $l_{\max}$.

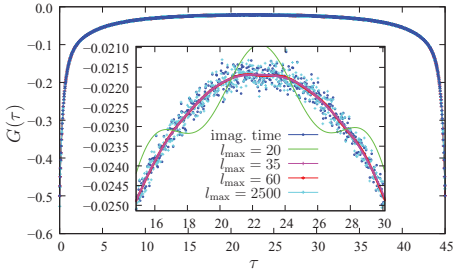

FIG. 3. (Color online) Imaginary-time Green's function $G(\tau)$ on the interval $[0,\beta]$ measured on a finite 1500-bin mesh (blue scattered points) and computed from $l_{\max}$ Legendre coefficients (solid lines). Four different choices for $l_{\max}$ are shown. Inset: zoom on the area around $\beta/2$.

This is expected because both of these values lie on the plateau. When $l_{\max}$ is very large, i.e., of the order of the number of imaginary-time bins, the noise in $G(\tau)$ eventually reappears and begins to resemble that of the direct measurement. We emphasize that all measurements have been performed within the same calculation and hence contain identical statistics. Hence the information in both measurements is identical up to the error committed by truncating the basis.

It is clear from this analysis that the truncation of the Legendre basis acts as a *noise filter*. We note that no information is lost by the truncation: the high-order coefficients correspond to information on very fine details of the Green's function, which cannot be resolved within a Monte Carlo calculation, as is obvious from the noisy $G(\tau)$.

C. Matsubara Green's function and high-frequency expansion

It is common to use the Fourier transform $G(i\nu_n)$ of $G(\tau)$ to manipulate Green's functions. This representation is, for example, convenient to compute the self-energy from Dyson's equation or to compute correlation energies. In terms of G_l, we can obtain the Matsubara Green's function with

$$G(i\nu_n) = \sum_{l\geqslant 0} G_l \frac{\sqrt{2l+1}}{\beta} \int_0^\beta d\tau\, e^{i\nu_n \tau} P_l[x(\tau)] = \sum_{l\geqslant 0} T_{nl} G_l, \tag{4}$$

where the unitary transformation T_{nl} is shown in Appendix E to be

$$T_{nl} = (-1)^n i^{l+1} \sqrt{2l+1}\; j_l\left(\frac{(2n+1)\pi}{2}\right), \tag{5}$$

with $j_l(z)$ denoting the spherical Bessel functions. Note that T_{nl} is independent of β.

In Fig. 4, we display the Matsubara Green's function as measured directly on the Matsubara axis and as computed from Eq. (4) with a fixed cutoff $l_{\max}$. The direct measurement of $G(i\nu_n)$ has been done within the same Monte Carlo

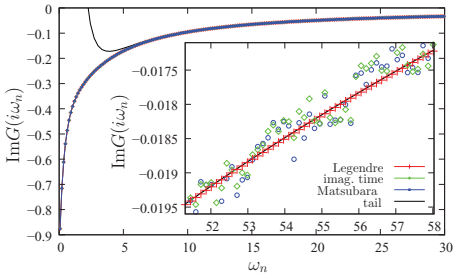

FIG. 4. (Color online) Matsubara Green's function obtained from measurements made directly on the Matsubara frequencies (blue scattered points), calculated from an imaginary-time measurement (green scattered points) and computed from Eq. (4) with $l_{\max} = 35$ (red solid line). The analytically known high-frequency tail is shown for comparison (black solid line). Inset: Blowup of the high-frequency region.

simulation as the one used to compute the G_l discussed above. It is clear from the plot that the truncation to $l_{\max}$ has filtered the high-frequency noise, and that for large $\mathrm{i}\nu_n$ the Matsubara Green's function has a smooth power-law decay. Let us emphasize here that the Matsubara Green's function is obtained in an unbiased manner that does not involve any model-guided Fourier transform (see also Ref. 22).

We will now show that the coefficients that control this power-law decay can also be accurately computed. Let us consider the high-frequency expansion of $G(\mathrm{i}\nu_n)$,

$$G(\mathrm{i}\nu_n) = \frac{c_1}{\mathrm{i}\nu_n} + \frac{c_2}{(\mathrm{i}\nu_n)^2} + \frac{c_3}{(\mathrm{i}\nu_n)^3} + \cdots. \tag{6}$$

Using the known high-frequency expansion of T_{nl} (cf. Appendix D),

$$T_{nl} = \frac{t_l^{(1)}}{\mathrm{i}\nu_n\beta} + \frac{t_l^{(2)}}{(\mathrm{i}\nu_n\beta)^2} + \frac{t_l^{(3)}}{(\mathrm{i}\nu_n\beta)^3} + \cdots, \tag{7}$$

one can directly relate the c_p and the G_l. Indeed, from (4), (6), and (7), it follows that

$$c_p = \frac{1}{\beta^p} \sum_{l\geqslant 0} t_l^{(p)} G_l. \tag{8}$$

The general expression of the coefficients $t_l^{(p)}$ is shown in (E8). For the first three moments, we have the following expressions:

$$c_1 = -\sum_{l\geqslant 0,\ \text{even}} \frac{2\sqrt{2l+1}}{\beta} G_l, \tag{9a}$$

$$c_2 = +\sum_{l>0,\ \text{odd}} \frac{2\sqrt{2l+1}}{\beta^2} G_l\, l(l+1), \tag{9b}$$

$$c_3 = -\sum_{l\geqslant 0,\ \text{even}} \frac{\sqrt{2l+1}}{\beta^3} G_l\,(l+2)(l+1)l(l-1). \tag{9c}$$

Since $t_l^{(p)} \sim l^{2p-3/2}$, with the fast decay of the G_l discussed above, we can expect a stable convergence of the c_p as a function of $l_{\max}$. Note, however, that when p increases, the coefficients grow, so we expect to need more and more Legendre coefficients to compute the series in practice.

The convergence of the moments is illustrated in Fig. 5. For the model we consider, the first moments are explicitly given by

$$c_1 = 1, \quad c_2 = 0,$$
$$c_3 = 5, \quad c_4 = 0.$$

We see that c_1 and c_3 smoothly converge to a plateau. For the higher moment c_5, a larger number of Legendre coefficients is required. A plateau is reached but is (depending on the accuracy of the data accumulated in the QMC simulation) quickly destabilized when $l_{\max}$ gets bigger and noisy G_l are included in the calculation. This clearly shows that $l_{\max}$ has to be chosen carefully to get sensitive c_p. For larger cutoff the error in the moments grows rapidly. This shows that a large error on the high-frequency moments is committed when measuring in a basis in which it is not possible to filter the noise, i.e., the conventional imaginary-time or Matsubara representation.

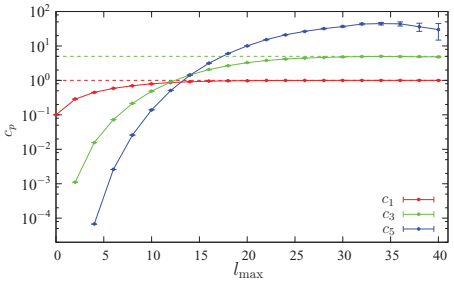

FIG. 5. (Color online) Convergence of the moments c_1, c_3, and c_5 as a function of $l_{\max}$. Only points corresponding to an even cutoff are shown because odd terms in the sum vanish. The analytically known results for c_1 and c_3 are indicated by dashed lines. Even moments are zero due to particle-hole symmetry.

Note that it is easy to incorporate *a priori* information on the moments c_p. For example, in the model we consider above, we have $c_1 = \langle\{c, c^\dagger\}\rangle = 1$. From (9a), we see that this is a *linear* constraint on the G_l coefficients, which we can therefore enforce by projecting the Legendre coefficients onto the ($l_{\max}$)-dimensional hyperplane defined by the constraint (9a). A correction to impose, e.g., a particular c_1 is straightforwardly found to be

$$G_l \to G_l + \left(\beta c_1 - \sum_{l'=0}^{l_{\max}} t_{l'}^{(1)} G_{l'}\right) \frac{t_l^{(1)}}{\sum_l \left|t_l^{(1)}\right|^2}. \tag{10}$$

This is easily generalized to other constraints.

D. Energy

The accurate determination of the high-frequency coefficients is of central importance, since many quantities are computed from sums over all Matsubara frequencies involving $G(\mathrm{i}\nu_n)$. Because $G(\mathrm{i}\nu_n)$ slowly decreases as $\sim 1/(\mathrm{i}\nu_n)$ to leading order, these sums are usually computed from the actual data up to a given Matsubara frequency, and the remaining frequencies are summed up analytically from the knowledge of the c_p. Thus, an incorrect determination of the c_p leads to significant numerical errors. This is a particularly delicate issue when $G(\mathrm{i}\nu_n)$ is measured directly on the Matsubara axis. In this case, one usually needs to fit the noisy high-frequency data to infer the high-frequency moments. As discussed above, such a procedure is not required when using Legendre coefficients, and the c_p can be computed in a controlled manner. In the following, we illustrate this point in an actual energy calculation.

Based on an LDA+DMFT calculation for the compound $SrVO_3$,[23,24] we compute the kinetic energy $E_{\mathrm{kin}} = (1/N) \sum_{k,\alpha} \langle n_{k\alpha}\rangle \epsilon_{k\alpha}$ and the correlation energy $E_{\mathrm{corr}} = (1/N) \sum_i U \langle n_{i\uparrow} n_{i\downarrow}\rangle$ (N denotes the number of lattice sites) resulting from the implementation and parameters of Ref. 24. These terms are contributions to the LDA+DMFT total energy,[25] which depend explicitly on the results of the DMFT impurity solver.

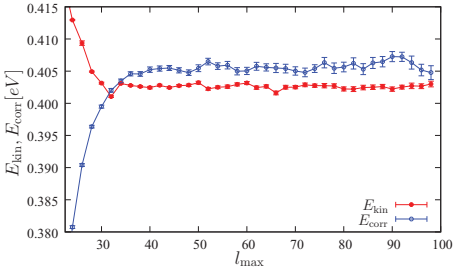

FIG. 6. (Color online) Kinetic energy $E_{\rm kin}$ (full symbols) and correlation energy $E_{\rm corr}$ (open symbols) for $SrVO_3$ as a function of $l_{\rm max}$, computed with the implementation and parameters of Ref. 25. For clarity, the kinetic energy has been shifted by 384.86 eV. Error bars are computed from 80 converged LDA+DMFT iterations.

The results are shown in Fig. 6. Here the parameter $l_{\rm max}$, against which these quantities are plotted, represents the number of Legendre coefficients used throughout the LDA+DMFT self-consistency. It is also the number of coefficients used to evaluate $\langle n_{k\alpha}\rangle$ from the lattice Green's function $G_k(i\nu_n)$. Note that $E_{\rm corr}$ has been accumulated directly within the CTQMC simulation.

In agreement with an analysis of the convergence with respect to the number of Legendre coefficients $l_{\rm max}$ similar to the ones shown in Figs. 2 and 5 for an *individual* DMFT iteration, we find a plateau for both energies at $l_{\rm max}\sim 40$. While the energy can be accurately computed within a single DMFT iteration, the error here stems mainly from the fluctuations between successive DMFT iterations. The plateau remains up to the largest values of $l_{\rm max}$. However, as $l_{\rm max}$ gets larger, so do the error bars due to the feedback of noise from the largest Legendre coefficients. Note that the error bars on the correlation energy, computed directly within the CTQMC algorithm, are of the same order of magnitude as those on the kinetic energy. The existence of a plateau implies that for a well-chosen cutoff $l_{\rm max}$, the energy can be computed in a controlled manner. We want to emphasize that such an approach is simpler and better controlled than delicate fitting procedures of high-frequency tails of the Green's function on the Matsubara axis.

II. TWO-PARTICLE GREEN'S FUNCTION

A. Legendre representation for two-particle Green's functions

The use of Legendre polynomials proves very useful when dealing with two-particle Green's functions. We will show that it brings about improvements both from the perspective of storage size and convergence as a function of the truncation. The object one mainly deals with is the generalized susceptibility,

$$\begin{aligned}\widetilde{\chi}^{\sigma\sigma'}(\tau_{12},\tau_{34},\tau_{14}) &= \widetilde{\chi}^{\sigma\sigma'}(\tau_1-\tau_2,\tau_3-\tau_4,\tau_1-\tau_4)\\ &= \langle \mathcal{T} c^\dagger_\sigma(\tau_1)c_\sigma(\tau_2)c^\dagger_{\sigma'}(\tau_3)c_{\sigma'}(\tau_4)\rangle\\ &\quad - \langle \mathcal{T} c^\dagger_\sigma(\tau_1)c_\sigma(\tau_2)\rangle\langle \mathcal{T} c^\dagger_{\sigma'}(\tau_3)c_{\sigma'}(\tau_4)\rangle. \quad (11)\end{aligned}$$

Let us emphasize that $\widetilde{\chi}$ is a function of three independent time differences only. With the particular choice made above, $\widetilde{\chi}$ is β-antiperiodic in τ_{12} and τ_{34} while it is β-periodic in τ_{14}. Consequently, its Fourier transform $\widetilde{\chi}(i\nu_n,i\nu_{n'},i\omega_m)$ is a function of two fermionic frequencies $\nu_n=2(n+1)\pi/\beta$, $\nu_{n'}=2(n'+1)\pi/\beta$, and one bosonic frequency $\omega_m=2m\pi/\beta$.

We introduce a representation of $\widetilde{\chi}(\tau_{12},\tau_{34},\tau_{14})$ in terms of the coefficients $\widetilde{\chi}_{ll'}(i\omega_m)$ such that

$$\begin{aligned}\widetilde{\chi}(\tau_{12},\tau_{34},\tau_{14}) = \sum_{l,l'\geqslant 0}\sum_{m\in\mathbb{Z}} \frac{\sqrt{2l+1}\sqrt{2l'+1}}{\beta^3}(-1)^{l'+1}\\ \times P_l[x(\tau_{12})]P_{l'}[x(\tau_{34})]e^{i\omega_m\tau_{14}}\widetilde{\chi}_{ll'}(i\omega_m). \quad (12)\end{aligned}$$

In this mixed basis representation, the τ_{12} and τ_{34} dependence of $\widetilde{\chi}(\tau_{12},\tau_{34},\tau_{14})$ is expanded in terms of Legendre polynomials, while the τ_{14} dependence is described through Fourier modes $e^{i\omega_m\tau_{14}}$. The motivation behind this choice is that many equations involving generalized susceptibilities (like the Bethe-Salpeter equation) are diagonal in $i\omega_m$. The inverse of (12) reads

$$\begin{aligned}\widetilde{\chi}_{ll'}(i\omega_m) = \iiint d\tau_{12}d\tau_{34}d\tau_{14}\sqrt{2l+1}\sqrt{2l'+1}(-1)^{l'+1}\\ P_l[x(\tau_{12})]P_{l'}[x(\tau_{34})]e^{-i\omega_m\tau_{14}}\widetilde{\chi}(\tau_{12},\tau_{34},\tau_{14}). \quad (13)\end{aligned}$$

We show in Appendix C how the Legendre expansion coefficients of the one- and two-particle Green's function [hence of $\widetilde{\chi}_{ll'}(i\omega_m)$] can be measured directly within CT-HYB. With the above definition, the Fourier transform $\widetilde{\chi}(i\nu_n,i\nu_{n'},i\omega_m)$ is easily found with

$$\widetilde{\chi}(i\nu_n,i\nu_{n'},i\omega_m) = \sum_{l,l'\geqslant 0} T_{nl}\widetilde{\chi}_{ll'}(i\omega_m)T^*_{n'l'}. \quad (14)$$

T_{nl} was already defined in Eq. (4). Using the additional unitarity property of T in Eq. (14), one can in general easily rewrite equations involving the Fourier coefficients $\widetilde{\chi}(i\nu_n,i\nu_{n'},i\omega_m)$ in sole terms of the $\widetilde{\chi}_{ll'}(i\omega_m)$.

In the DMFT framework, the lattice susceptibility $\widetilde{\chi}_{\rm latt}$ is obtained from[1,2]

$$\begin{aligned}[\underline{\underline{\widetilde{\chi}_{\rm latt}}}]^{-1}(i\omega_m,\mathbf{q}) = [\underline{\underline{\widetilde{\chi}_{\rm loc}}}]^{-1}(i\omega_m)\\ - \big[\underline{\underline{\widetilde{\chi}^0_{\rm loc}}}\big]^{-1}(i\omega_m) + \big[\underline{\underline{\widetilde{\chi}^0_{\rm latt}}}\big]^{-1}(i\omega_m,\mathbf{q}), \quad (15)\end{aligned}$$

where the double underline emphasizes that this is to be thought of as a matrix equation for the coefficients $\widetilde{\chi}$ expressed either in $(i\nu_n,i\nu_{n'})$ in the Fourier representation or in (l,l') in the mixed Legendre-Fourier representation. The bare susceptibilities are given by

$$\begin{aligned}\widetilde{\chi}^0_{\rm loc}(i\nu_n,i\nu_{n'},i\omega_m) &= -G_{\rm loc}(i\nu_n+i\omega_m)G_{\rm loc}(i\nu_n)\delta_{n,n'},\\ \widetilde{\chi}^0_{\rm latt}(i\nu_n,i\nu_{n'},i\omega_m,\mathbf{q}) &= -\sum_{\mathbf{k}} G^{\rm latt}_{\mathbf{k}+\mathbf{q}}(i\nu_n+i\omega_m)G^{\rm latt}_{\mathbf{k}}(i\nu_n)\delta_{n,n'},\end{aligned} \quad (16)$$

where

$$G^{\rm latt}_{\mathbf{k}}(i\nu_n) = [i\nu_n+\mu-\epsilon_{\mathbf{k}}-\Sigma_{\rm loc}(i\nu_n)]^{-1}, \quad (17)$$

and $G_{\rm loc}$, $\Sigma_{\rm loc}$ are the Green's function and self-energy of the local DMFT impurity problem, respectively. The equivalent

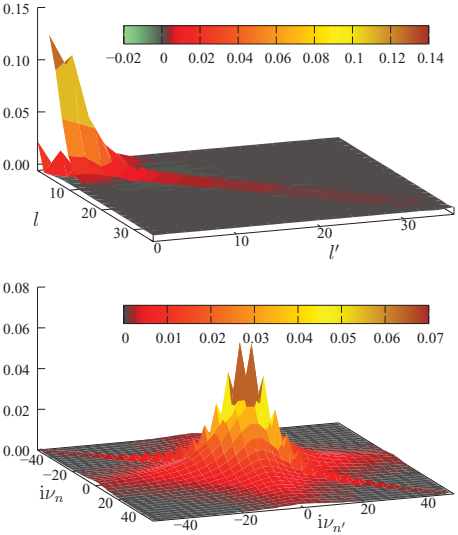

FIG. 7. (Color online) Generalized local magnetic susceptibility $\widetilde{\chi}^{\mathrm{m}}_{\mathrm{loc}} = \frac{1}{2}(\widetilde{\chi}^{\uparrow\uparrow}_{\mathrm{loc}} - \widetilde{\chi}^{\uparrow\downarrow}_{\mathrm{loc}})$ at the bosonic frequency $\mathrm{i}\omega_m = 0$ computed from the DMFT impurity problem. Upper panel: coefficients $\widetilde{\chi}^{\mathrm{m}}_{\mathrm{loc},ll'}(0)$ in the mixed Legendre-Fourier representation. Lower panel: Fourier coefficients $\widetilde{\chi}^{\mathrm{m}}_{\mathrm{loc}}(\mathrm{i}\nu_n,\mathrm{i}\nu_{n'},0)$.

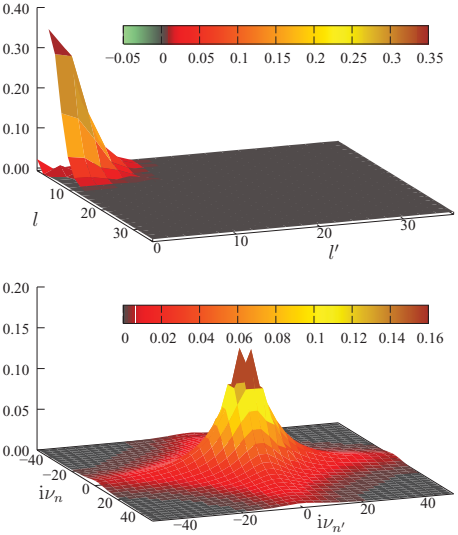

FIG. 8. (Color online) Vertex part of the generalized magnetic lattice susceptibility $\widetilde{\chi}^{\mathrm{m}}_{\mathrm{latt}} - \widetilde{\chi}^{0}_{\mathrm{latt}}$ at the bosonic frequency $\mathrm{i}\omega_m = 0$ and at the antiferromagnetic wave vector $\mathbf{q} = (\pi,\pi,\pi)$. Upper panel: coefficients $\widetilde{\chi}^{\mathrm{m}}_{\mathrm{latt},ll'}(0) - \widetilde{\chi}^{0}_{\mathrm{latt},ll'}(0)$ in the mixed Legendre-Fourier representation. Lower panel: Fourier coefficients $\widetilde{\chi}^{\mathrm{m}}_{\mathrm{latt}}(\mathrm{i}\nu_n,\mathrm{i}\nu_{n'},0) - \widetilde{\chi}^{0}_{\mathrm{latt}}(\mathrm{i}\nu_n,\mathrm{i}\nu_{n'},0)$ of the lattice susceptibility. Both plots employ the same number of coefficients.

susceptibilities in the mixed Legendre-Fourier representation are simply obtained as the inverse of Eq. (14),

$$\widetilde{\chi}^{0}_{ll'}(\mathrm{i}\omega_m,\mathbf{q}) = \sum_{n,n'\in\mathbb{Z}} T^{*}_{nl}\widetilde{\chi}^{0}(\mathrm{i}\nu_n,\mathrm{i}\nu_{n'},\mathrm{i}\omega_m,\mathbf{q})T_{n'l'}, \qquad (18)$$

where the high-frequency behavior of $G_{\mathrm{loc}}(\mathrm{i}\nu_n)$ and $G^{\mathrm{latt}}(\mathrm{i}\nu_n)$ can easily be considered in the frequency sums. Evaluation of lattice susceptibilities from $\widetilde{\chi}_{\mathrm{latt}}(\mathrm{i}\nu_n,\mathrm{i}\nu_{n'},\mathrm{i}\omega_m)$ can also directly be propagated to the mixed Legendre-Fourier representation, abolishing altogether the need to transform back to the Fourier representation,

$$\begin{aligned}\chi(\mathrm{i}\omega_m,\mathbf{q}) &= \frac{1}{\beta^2}\sum_{nn'\in\mathbb{Z}}\widetilde{\chi}_{\mathrm{latt}}(\mathrm{i}\nu_n,\mathrm{i}\nu_{n'},\mathrm{i}\omega_m,\mathbf{q}) \\ &= \frac{1}{\beta^2}\sum_{ll'\geqslant 0}(-1)^{l+l'}\sqrt{2l+1}\sqrt{2l'+1}\,\widetilde{\chi}_{\mathrm{latt},ll'}(\mathrm{i}\omega_m,\mathbf{q}).\end{aligned} \qquad (19)$$

Note that $\widetilde{\chi}_{\mathrm{latt}}$ can be written as the sum of a free two-particle propagation $\widetilde{\chi}^{0}_{\mathrm{latt}}$, Eq. (16) (bubble part), and a connected rest $\widetilde{\chi}^{\mathrm{conn}}_{\mathrm{latt}}$ (vertex part). These two terms can be separately summed in Eq. (19).

The present mixed-basis representation has been successfully used in a recent investigation of static finite-temperature lattice charge and magnetic susceptibilities for the $\mathrm{Na}_x\mathrm{CoO}_2$ system at intermediate-to-larger doping x.[26] A first example for the dynamical, i.e., finite-frequency, case will be discussed in Sec. II C.

B. Antiferromagnetic susceptibility of the three-dimensional Hubbard model

In order to benchmark our approach, we investigate the antiferromagnetic susceptibility of the half-filled Hubbard model (3) on a cubic lattice within the DMFT framework. All quantities are again expressed in units of the hopping t and with $U/t = 20$ and $T/t = 0.45$. This temperature is sufficiently close to the DMFT Néel temperature $T_N \approx 0.30t$ to yield a dominant vertex part, while still having a non-negligible bubble contribution.

We compute the susceptibility $\widetilde{\chi}_{\mathrm{loc}}$ of the DMFT impurity problem using the CT-HYB algorithm. In Fig. 7, we compare the mixed Legendre-Fourier coefficients $\widetilde{\chi}_{ll'}(\mathrm{i}\omega_m)$ to the Fourier coefficients $\widetilde{\chi}(\mathrm{i}\nu_n,\mathrm{i}\nu_{n'},\mathrm{i}\omega_m)$. For clarity, we focus on the first bosonic frequency $\mathrm{i}\omega_m = 0$. We observe that the $\widetilde{\chi}_{ll'}(0)$ have a very fast decay except in the $l = l'$ direction. This contrasts with the behavior of $\widetilde{\chi}(\mathrm{i}\nu_n,\mathrm{i}\nu_{n'},0)$, which exhibits slower decay in the three major directions $\mathrm{i}\nu_n = 0$, $\mathrm{i}\nu_{n'} = 0$, and $\mathrm{i}\nu_n = \mathrm{i}\nu_{n'}$.

The generalized susceptibility in τ differences (11) has discontinuities along the planes $\tau_{14} = 0$ and $\tau_{14} = \tau_{12} + \tau_{34}$ as well as nonanalyticities (kinks) for $\tau_{12} = 0$ and $\tau_{34} = 0$. These planes induce corresponding slow decay in the Fourier representation (14).[22] When it comes to the mixed Legendre-Fourier representation (13), however, the planes $\tau_{12} = 0$ and $\tau_{34} = 0$ are on the border of the imaginary-time region being expanded in this basis, which renders the coefficients insensitive toward these.

Computing lattice susceptibilities from Eq. (15), it is necessarily required to truncate the matrices. This leads to difficulties when computing the susceptibility from the Fourier coefficients $\widetilde{\chi}_{\rm loc}(i\nu_n, i\nu_{n'}, i\omega_m)$. As we can see from Fig. 7, the Fourier coefficients have a slow decay along three directions. The inversion of $\widetilde{\chi}_{\rm loc}(i\nu_n, i\nu_{n'}, i\omega_m)$ is delicate because many coefficients are involved even for large ν, ν'. One needs to use a very large cutoff to obtain a precise result. Alternatively, one can try to separate the high- and low-frequency parts of the equation and replace the susceptibilities with their asymptotic form at high frequency (see Ref. 27). While it is effectively possible to treat larger matrices, it is still required to impose a cutoff on the high-frequency part for the numerical computations.

In the mixed Legendre-Fourier representation, the situation is different. Only the coefficients along the diagonal decay slowly. In the inversion of the matrix, the elements on the diagonal for large l are essentially recomputed from themselves. One can expect that there will be a lot less mixing and thus a much faster convergence as a function of the truncation.

In Fig. 8, we display the vertex part of the generalized lattice susceptibility $\widetilde{\chi}_{\rm latt} - \widetilde{\chi}^0_{\rm latt}$ obtained from Eq. (15) in both representations. In both cases, we see that the diagonal part quickly becomes very small. In other words, the diagonal of the lattice susceptibility is essentially given by the bubble part $\widetilde{\chi}^0_{\rm latt}$. However, while essentially all the information is condensed close to $l, l' = 0$ in the mixed Legendre-Fourier representation, the Fourier coefficients still have a slow decay along the directions given by $i\nu_n = 0$ and $i\nu_{n'} = 0$. From this figure, one can speculate that a quantity computed from the Legendre-Fourier coefficients will converge rapidly as a function of a cutoff $l_{\rm max}$. However, we need to make sure that the coefficients close to $l, l' = 0$ are not affected much by the truncation.

In order to assess the validity of these speculations, we compute the static antiferromagnetic [$\mathbf{q} = (\pi, \pi, \pi)$] susceptibility $\chi^{\rm m}(0, \mathbf{q})$ as a function of the cutoff in both representations. It is obtained from Eq. (19) using the magnetic susceptibility $\widetilde{\chi}^{\rm m} = \frac{1}{2}(\widetilde{\chi}^{\uparrow\uparrow} - \widetilde{\chi}^{\uparrow\downarrow})$.

Since the diagonal of the lattice susceptibility is essentially given by the bubble (see Fig. 8), the sums above are performed in two steps. The vertex part shown in Fig. 8 is summed up to the chosen cutoff, while the bubble part is summed over all frequencies with the knowledge of its high-frequency behavior. The result is shown in Fig. 9. It reveals a major benefit of the Legendre representation: the susceptibility converges much faster as a function of the cutoff. The static susceptibility is essentially converged at $l_{\rm max} \sim 12$. This corroborates the idea that the small-l, l' part of $\widetilde{\chi}_{{\rm latt},ll'}$ is only weakly dependent on the further diagonal elements of $\widetilde{\chi}_{{\rm loc},ll'}$.

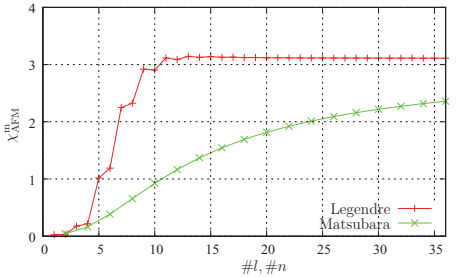

FIG. 9. (Color online) Antiferromagnetic susceptibility as a function of the number of Legendre ($l = l_{\rm max} + 1$) and Matsubara ($n = 2n_{\rm max} + 2$) coefficients, respectively, used in the calculation.

C. Dynamical susceptibility of the two-dimensional Hubbard model

As a final benchmark, we demonstrate that our method is not restricted to the static case. To this end, we show the momentum resolved dynamical magnetic susceptibility $\chi(\omega, \mathbf{q})$ for a DMFT calculation for the half-filled two-dimensional (2D) square lattice Hubbard model in Fig. 10. We have chosen an on-site interaction $U/t = 4$ and temperature $T/t = 0.25$, which is slightly above the DMFT Néel temperature. The susceptibility was computed from the Legendre representation according to Eq. (19) using 20×20 Legendre coefficients, which was sufficient for all bosonic frequencies. In general, for higher bosonic frequencies, more Legendre coefficients are needed to represent the vertex part of the generalized magnetic lattice susceptibility. However, no additional structure appears in the high l, l' region. We then analytically continued the data using Padé approximants.[28] The figure shows the typical magnon spectrum[6,29,30] reminiscent of a spin wave in this paramagnetic state with strongly enhanced weight at the antiferromagnetic wave vector $\mathbf{q} = (\pi, \pi)$ due to the proximity of the mean-field antiferromagnetic instability.

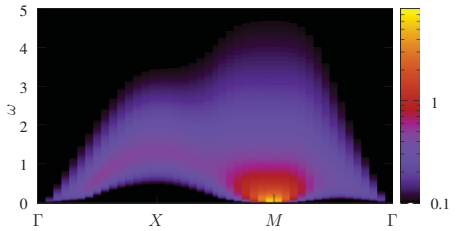

FIG. 10. (Color online) Imaginary part of the magnetic susceptibility on the real frequency axis along high-symmetry lines in the 2D Brillouin zone.

III. CONCLUSION

In this paper, we have studied the representation of imaginary-time Green's functions in terms of a Legendre orthogonal polynomial basis. We have shown that CTQMC can directly accumulate the Green's function in this basis. This representation has several advantages over the standard Matsubara frequency representation: (i) It is much more compact, i.e., coefficients decay much faster; this is particularly interesting for storing and manipulating the two-particle Green's functions. Moreover, two-particle response functions can be computed directly in the Legendre representation, without the need to transform back to the Matsubara representation. In particular, the matrix manipulations required for the solution of the Bethe-Salpeter equations can be performed in this basis. We have shown that this greatly enhances the accuracy of the calculations, since in contrast to the Matsubara representation, the error due to the truncation of the matrices becomes negligible. (ii) The Monte Carlo noise is mainly concentrated in the higher Legendre coefficients, the contribution of which is usually very small; this allows us to develop a systematic method to filter out noise in physical quantities and to obtain more accurate values for, e.g., the correlation energy in LDA+DMFT computations.

ACKNOWLEDGMENTS

L.B. and F.L. thank A.I. Lichtenstein for helpful discussions. M.F. and O.P. thank M. Aichhorn for helpful discussions and providing the parameters and data from Ref. 24. O.P. thanks J. M. Normand for pointing out Ref. 31. We thank P. Werner for a careful reading of the manuscript. Calculations were performed with the TRIQS[21] project using HPC resources from The North-German Supercomputing Alliance (HLRN) and from GENCI-CCRT (Grant No. 2011-t2011056112). TRIQS uses some libraries of the ALPS[32] project. This work was supported by the DFG Research Unit FOR 1346.

APPENDIX A: SOME PROPERTIES OF THE LEGENDRE POLYNOMIALS

In this appendix, we summarize for convenience some basic properties of the Legendre polynomials. Further references can be found in Refs. 31,33,34. We use the standardized polynomial $P_l(x)$ defined on $x \in [-1,1]$ through the recursive relation

$$(l+1)P_{l+1}(x) = (2l+1)xP_l(x) - lP_{l-1}(x), \quad \text{(A1)}$$

$$P_0(x) = 1, \quad P_1(x) = x. \quad \text{(A2)}$$

P_l are orthogonal and their normalization is given by

$$\int_{-1}^{1} dx\, P_k(x)P_l(x) = \frac{2}{2l+1}\delta_{kl}. \quad \text{(A3)}$$

The P_l are bounded on the segment $[-1,1]$ by[34]

$$|P_l(x)| \leqslant 1 \quad \text{(A4)}$$

with the special points

$$P_l(\pm 1) = (\pm 1)^l. \quad \text{(A5)}$$

The primitive of $P_l(x)$ that vanishes at $x = -1$ is (cf. Ref. 31, Vol. II, Sec. 10.10)

$$\int_{-1}^{x} dy\, P_l(y) = \frac{P_{l+1}(x) - P_{l-1}(x)}{2l+1}, \quad l \geqslant 1. \quad \text{(A6)}$$

By orthogonality or (A5), it also vanishes at $x = 1$. The Fourier transform of the Legendre polynomial restricted to the segment $[-1,1]$ is given by formula 7.243.5 of Ref. 33,

$$\int_{-1}^{1} e^{iax} P_l(x)\, dx = i^l \sqrt{\frac{2\pi}{a}} J_{l+\frac{1}{2}}(a) = 2i^l j_l(a), \quad \text{(A7)}$$

where J denotes the Bessel function and $j_l(a) = \sqrt{\frac{\pi}{2a}} J_{l+\frac{1}{2}}(a)$ denotes the spherical Bessel functions.

APPENDIX B: FAST DECAY OF THE LEGENDRE COEFFICIENTS

Let us consider a function $g(\tau)$ smooth on the segment $[0,\beta]$ (i.e., to be precise, $\mathcal{C}^\infty$, indefinitely differentiable), and β-antiperiodic, like a Green's function. In this appendix, we show that its Legendre coefficients decay faster than any power law contrary to its standard Fourier expansion coefficients, which decay as power laws determined by the discontinuities of the function and its derivatives.

Let us start by recalling the asymptotics of the standard Fourier expansion coefficients on fermionic Matsubara frequencies. These coefficients are given by

$$\hat{g}(i\nu_n) = \int_0^\beta d\tau\, g(\tau) e^{i\nu_n \tau} \quad \text{(B1)}$$

$$= \frac{g(\tau)e^{i\nu_n\tau}|_0^\beta}{i\nu_n} - \int_0^\beta d\tau\, g'(\tau)\frac{e^{i\nu_n\tau}}{i\nu_n}. \quad \text{(B2)}$$

The coefficients vanish for $n \to \infty$, and applying the same result to g', one obtains

$$\hat{g}(i\nu_n) = -\frac{g(\beta^-) + g(0^+)}{i\nu_n} + O\left(\frac{1}{\nu_n^2}\right). \quad \text{(B3)}$$

Let us now turn to the Legendre expansion. Using the same rescaling as before, we can consider for simplicity a function $f(x)$ smooth on $[-1,1]$. We can proceed in a similar way using the primitive of the Legendre polynomial [which is also given by a simple formula, (A6)]. For $l \geqslant 1$, we have

$$\begin{aligned}\frac{f_l}{\sqrt{2l+1}} &= \int_{-1}^{1} dx\, f(x)P_l(x) \\ &= f(x)\left(\int_{-1}^{x} dy\, P_l(y)\right)\Big|_{-1}^{1} \\ &\quad - \int_{-1}^{1} dx\, f'(x)\left(\int_{-1}^{x} dy\, P_l(y)\right) \\ &= -\int_{-1}^{1} dx\, f'(x)\frac{P_{l+1}(x) - P_{l-1}(x)}{2l+1}. \quad \text{(B4)}\end{aligned}$$

The crucial difference with the Fourier case is that, for $l \geqslant 1$, *the boundary terms always cancel*, regardless of the function f due to the orthogonality property of the polynomials [it can also be checked directly from (A5)]. So we are left with just

the integral term. Since the Legendre coefficients of f' vanish at large l (by applying the previous formula to f'), we get instead of (B3)

$$\frac{f_l}{\sqrt{2l+1}} = o\left(\frac{1}{l}\right). \tag{B5}$$

In both cases, the reasoning can be reproduced recursively by further differentiating the function, as long as no singularity is encountered. In the Fourier case, it produces the well-known high-frequency expansion in terms of the discontinuity of the function and its derivatives. In the Legendre case, we find that the coefficients are $o(1/l^k)$ as soon as f is k times differentiable. Hence if the function is smooth on $[-1,1]$, the coefficients decay asymptotically faster than any power law.

The only point that remains to be checked is that indeed $G(\tau)$ is smooth on $[0,\beta]$. It is clear from its spectral representation

$$G(\tau) = -\int_{-\infty}^{\infty} d\nu \frac{e^{-\tau\nu}}{1+e^{-\beta\nu}} A(\nu) \tag{B6}$$

if we admit that the spectral function $A(\nu)$ has compact support, by differentiating under the integral.

Finally, while this simple result of "fast decay" is enough for our purposes in this paper, it is possible to get much more refined statements on the asymptotics of the Legendre coefficients of the function f, in particular when it has some analyticity properties. For a detailed discussion of these issues, and in particular of the conditions needed to get the generic exponential decay of the coefficients, we refer the reader to Ref. 35.

APPENDIX C: DIRECT ACCUMULATION OF THE LEGENDRE COEFFICIENTS FOR THE CT-HYB ALGORITHM

In this appendix, we describe how to compute directly the Legendre expansion of the one-particle and the two-particle Green's function.

1. The accumulation formulas in CT-HYB

For completeness, let us first recall the accumulation formula for the one-particle and the two-particle Green's functions in the CT-HYB algorithm,[8,9,11,19] which sums the perturbation theory in the hybridization function $\Delta_{ab}(\mathrm{i}\nu_n)$ on the Matsubara axis. While these formulas have appeared previously in the literature, this simple functional derivation emphasizes the "Wick"-like form of the higher-order correlation function.

The partition function of the impurity model reads

$$Z = \int \mathcal{D}c^\dagger \mathcal{D}c \exp(-S_{\mathrm{eff}}), \tag{C1}$$

where the effective action has the form

$$S_{\mathrm{eff}} = -\int_0^\beta\int_0^\beta d\tau d\tau' \sum_{A,B} c_A^\dagger(\tau) G^{-1}_{0,AB}(\tau,\tau') c_B(\tau') + \int_0^\beta d\tau H_{\mathrm{int}}(\{c_A^\dagger(\tau), c_A(\tau)\}), \tag{C2}$$

$$G^{-1}_{0AB}(\mathrm{i}\nu_n) = (\mathrm{i}\nu_n + \mu)\delta_{AB} - h^0_{AB} - \Delta_{AB}(\mathrm{i}\nu_n). \tag{C3}$$

To simplify the notations, we use here a generic index A,B. In the case in which there are symmetries, like the spin SU(2) symmetry in the standard DMFT problem, the Green's functions are block-diagonal. For example, the generic index A can be (a,σ), where a is an orbital or site index, and the spin index $\sigma = \uparrow,\downarrow$ is the block index.

The partition function is expanded in powers of the hybridization Δ as

$$Z = \sum_{n\geqslant 0} \int \prod_{i=1}^n d\tau_i d\tau_i' \sum_{\lambda_i,\lambda_i'} w(n,\{\lambda_j,\lambda_j',\tau_j,\tau_j'\}), \tag{C4}$$

$$w(n,\{\lambda_j,\lambda_j',\tau_j,\tau_j'\}) \equiv \frac{1}{n!^2} \det_{1\leqslant i,j\leqslant n} [\Delta_{\lambda_i,\lambda_j'}(\tau_i - \tau_j')] \times \mathrm{Tr}\left(\mathcal{T} e^{-\beta H_{\mathrm{loc}}} \prod_{i=1}^n c^\dagger_{\lambda_i}(\tau_i) c_{\lambda_i'}(\tau_i')\right), \tag{C5}$$

where $\mathcal{T}$ is time ordering and H_{loc} is the local Hamiltonian.[8,9,11,19] $|w|$ are the weights of the quantum Monte Carlo (QMC) Markov chain. Introducing the short notation $\mathcal{C} \equiv (n,\{\lambda_j,\lambda_j',\tau_j,\tau_j'\})$ for the QMC configuration, the partition function Z and the average of any function f over the configuration space (denoted by angular brackets in this section) are given by

$$Z = \sum_{\mathcal{C}} w(\mathcal{C}), \tag{C6}$$

$$\langle f(\mathcal{C})\rangle = \frac{1}{Z}\sum_{\mathcal{C}} w(\mathcal{C}) f(\mathcal{C}). \tag{C7}$$

The one-particle and two-particle Green's functions are obtained as functional derivatives of Z with respect to the hybridization function, as

$$G_{AB}(\tau_1,\tau_2) = -\frac{1}{Z}\frac{\partial Z}{\partial \Delta_{BA}(\tau_2,\tau_1)}, \tag{C8a}$$

$$G^{(4)}_{ABCD}(\tau_1,\tau_2,\tau_3,\tau_4) = \frac{1}{Z}\frac{\partial^2 Z}{\partial \Delta_{BA}(\tau_2,\tau_1)\partial\Delta_{DC}(\tau_4,\tau_3)}. \tag{C8b}$$

To use the expansion of Z, we need to compute the derivative of a determinant with respect to its elements. Let us consider a general matrix $\bar{\Delta}$, its inverse $\bar{M} \equiv \bar{\Delta}^{-1}$, and use the Grassman integral representation

$$\det \bar{\Delta} = \int \prod_i d\eta_i d\bar{\eta}_i e^{\sum_{ij}\bar{\eta}_i \bar{\Delta}_{ij}\eta_j}. \tag{C9}$$

Using the Wick theorem, we have

$$\frac{\partial \det\bar{\Delta}}{\partial \bar{\Delta}_{ba}} = \int \prod_i d\eta_i d\bar{\eta}_i (\bar{\eta}_b\eta_a) e^{\sum_{ij}\bar{\eta}_i\bar{\Delta}_{ij}\eta_j} = \det\bar{\Delta}\times\bar{M}_{ab}, \tag{C10a}$$

$$\frac{\partial^2 \det\bar{\Delta}}{\partial\bar{\Delta}_{ba}\partial\bar{\Delta}_{dc}} = \int \prod_i d\eta_i d\bar{\eta}_i (\bar{\eta}_b\eta_a\bar{\eta}_d\eta_c) e^{\sum_{ij}\bar{\eta}_i\bar{\Delta}_{ij}\eta_j} = \det\bar{\Delta}(\bar{M}_{ab}\bar{M}_{cd} - \bar{M}_{ad}\bar{M}_{cb}). \tag{C10b}$$

Let us now apply (C10) by introducing for each configuration $\mathcal{C} \equiv (n,\{\lambda_j,\lambda_j',\tau_j,\tau_j'\})$ the matrix $\hat{\Delta}(\mathcal{C})$ of size n given by

$$\hat{\Delta}(\mathcal{C})_{ij} \equiv \Delta_{\lambda_i,\lambda_j'}(\tau_i - \tau_j') \tag{C11}$$

and its inverse $M^{\mathcal{C}} \equiv [\hat{\Delta}(\mathcal{C})]^{-1}$. We obtain

$$\frac{\partial w(\mathcal{C})}{\partial \Delta_{BA}(\tau_2,\tau_1)} = \frac{w(\mathcal{C})}{\det \hat{\Delta}(\mathcal{C})} \sum_{\alpha,\beta=1}^{n} \frac{\partial \det \hat{\Delta}(\mathcal{C})}{\partial \hat{\Delta}(\mathcal{C})_{\beta\alpha}} \frac{\partial \hat{\Delta}(\mathcal{C})_{\beta\alpha}}{\partial \Delta_{BA}(\tau_2,\tau_1)}$$

$$= w(\mathcal{C}) \sum_{\alpha,\beta=1}^{n} M^{\mathcal{C}}_{\alpha\beta} \frac{\partial \hat{\Delta}(\mathcal{C})_{\beta\alpha}}{\partial \Delta_{BA}(\tau_2,\tau_1)} \tag{C12a}$$

and

$$\frac{\partial^2 w(\mathcal{C})}{\partial \Delta_{BA}(\tau_2,\tau_1)\partial \Delta_{DC}(\tau_4,\tau_3)} = \frac{w(\mathcal{C})}{\det \hat{\Delta}(\mathcal{C})} \sum_{\alpha\beta\gamma\delta=1}^{n} \frac{\partial^2 \det \hat{\Delta}(\mathcal{C})}{\partial \hat{\Delta}(\mathcal{C})_{\beta\alpha} \partial \hat{\Delta}(\mathcal{C})_{\delta\gamma}} \times \frac{\partial \hat{\Delta}(\mathcal{C})_{\beta\alpha}}{\partial \Delta_{BA}(\tau_2,\tau_1)} \frac{\partial \hat{\Delta}(\mathcal{C})_{\delta\gamma}}{\partial \Delta_{DC}(\tau_4,\tau_3)}. \tag{C12b}$$

Denoting

$$D(\mathcal{C})^{\alpha\beta}_{AB\tau_1\tau_2} \equiv \frac{\partial \hat{\Delta}(\mathcal{C})_{\beta\alpha}}{\partial \Delta_{BA}(\tau_2,\tau_1)} = \delta(\tau_1 - \tau'_\alpha)\delta(\tau_2 - \tau_\beta)\delta_{\lambda'_\alpha,A}\delta_{\lambda_\beta,B}, \tag{C13}$$

we finally obtain the accumulation formulas for the Green's functions,[8,9]

$$G_{AB}(\tau_1,\tau_2) = -\left\langle \sum_{\alpha\beta=1}^{n} M^{\mathcal{C}}_{\alpha\beta} D(\mathcal{C})^{\alpha\beta}_{AB\tau_1\tau_2} \right\rangle, \tag{C14a}$$

$$G^{(4)}_{ABCD}(\tau_1,\tau_2,\tau_3,\tau_4) = \left\langle \sum_{\alpha\beta\gamma\delta=1}^{n} \left(M^{\mathcal{C}}_{\alpha\beta} M^{\mathcal{C}}_{\gamma\delta} - M^{\mathcal{C}}_{\alpha\delta} M^{\mathcal{C}}_{\gamma\beta}\right) \times D(\mathcal{C})^{\alpha\beta}_{AB\tau_1\tau_2} D(\mathcal{C})^{\gamma\delta}_{CD\tau_3\tau_4} \right\rangle. \tag{C14b}$$

2. Legendre expansion of the one-particle Green's function

We take into account the time translation invariance and the τ-antiperiodicity of the Green's function in the following way. *A priori*, in (C14a), the arguments τ_1,τ_2 are in the interval $[0,\beta]$. We can, however, easily make this function β-antiperiodic in both arguments

$$\widetilde{G}_{AB}(\tau_1,\tau_2) = -\left\langle \sum_{\alpha\beta=1}^{n} M^{\mathcal{C}}_{\alpha\beta} \delta^-(\tau_1 - \tau'_\alpha)\delta^-(\tau_2 - \tau_\beta)\delta_{\lambda'_\alpha,A}\delta_{\lambda_\beta,B} \right\rangle, \tag{C15}$$

where we defined the periodic and antiperiodic Dirac comb, respectively, by

$$\delta^{\pm}(\tau) \equiv \sum_{n\in\mathbb{Z}} (\pm 1)^n \delta(\tau - n\beta). \tag{C16}$$

At convergence of the Monte Carlo Markov chain, the Green's function is in fact translationally invariant in imaginary time, and we have

$$G_{AB}(\tau) = \frac{1}{\beta}\int_0^\beta ds\ \widetilde{G}_{AB}(\tau + s, s), \tag{C17}$$

which leads to

$$G_{AB}(\tau) = -\frac{1}{\beta}\left\langle \sum_{\alpha\beta=1}^{n} M^{\mathcal{C}}_{\alpha\beta} \delta^-[\tau - (\tau'_\alpha - \tau_\beta)]\delta_{\lambda'_\alpha,A}\delta_{\lambda_\beta,B} \right\rangle. \tag{C18}$$

Finally, Eq. (C18) can be transformed to a measurement in the Legendre representation according to (2),

$$G_{AB;l} = -\frac{\sqrt{2l+1}}{\beta}\left\langle \sum_{\alpha\beta=1}^{n} M^{\mathcal{C}}_{\alpha\beta} \widetilde{P}_l(\tau'_\alpha - \tau_\beta)\delta_{\lambda'_\alpha,A}\delta_{\lambda_\beta,B} \right\rangle, \tag{C19}$$

where $\widetilde{P}(\delta\tau)$ is defined by

$$\widetilde{P}_l(\delta\tau) = \begin{cases} P_l[x(\delta\tau)], & \delta\tau > 0, \\ -P_l[x(\delta\tau + \beta)], & \delta\tau < 0. \end{cases} \tag{C20}$$

3. Legendre accumulation of the two-particle Green's function

The generalized susceptibility $\widetilde{\chi}$ of (11) can be expressed in term of G and $G^{(4)}$ as

$$\widetilde{\chi}^{\sigma\sigma'}_{abcd}(\tau_{12},\tau_{34},\tau_{14}) = G^{(4)}_{b\sigma,a\sigma,d\sigma',c\sigma'}(\tau_{21},\tau_{43},\tau_{23}) - G_{b\sigma,a\sigma}(\tau_{21})G_{d\sigma',c\sigma'}(\tau_{43}), \tag{C21}$$

so in this subsection we will focus on the computation of $G^{(4)}$. We take into account the time translation invariance with the same technique as for the one-particle Green's function. First we make the function $G^{(4)}(\tau_1,\tau_2,\tau_3,\tau_4)$ fully β-antiperiodic in the four variables using the antiperiodic Dirac comb δ^- defined in (C16), and we use the time translation invariance of the Green's function to obtain

$$G^{(4)}(\tau_{12},\tau_{34},\tau_{14}) = \frac{1}{\beta}\int_0^\beta d\bar{\tau}\ \widetilde{G}^{(4)}(\tau_{14}+\bar{\tau}, \tau_{14}-\tau_{12}+\bar{\tau}, \tau_{34}+\bar{\tau}, \bar{\tau}). \tag{C22}$$

From (C14b), we get

$$G^{(4)}_{ABCD}(\tau_{12},\tau_{34},\tau_{14}) = \frac{1}{\beta}\left\langle \sum_{\alpha\beta\gamma\delta=1}^{n} \left(M^{\mathcal{C}}_{\alpha\beta} M^{\mathcal{C}}_{\gamma\delta} - M^{\mathcal{C}}_{\alpha\delta} M^{\mathcal{C}}_{\gamma\beta}\right)\delta^-(\tau_{12} - (\tau'_\alpha - \tau_\beta))\delta^-(\tau_{34} - (\tau'_\gamma - \tau_\delta))\delta^+(\tau_{14} - (\tau'_\alpha - \tau_\delta))\delta_{\lambda'_\alpha,A}\delta_{\lambda_\beta,B}\delta_{\lambda'_\gamma,C}\delta_{\lambda_\delta,D} \right\rangle, \tag{C23}$$

where δ^+ and δ^- are defined in (C16). Applying (13), the accumulation formula in the mixed Legendre-Fourier basis is straightforwardly obtained as

$$G^{(4)}_{ABCD}(l,l',\mathrm{i}\omega_m) = \frac{\sqrt{2l+1}\sqrt{2l'+1}}{\beta}(-1)^{l'+1}\left\langle \sum_{\alpha\beta\gamma\delta=1}^{n} \left(M^{\mathcal{C}}_{\alpha\beta} M^{\mathcal{C}}_{\gamma\delta} - M^{\mathcal{C}}_{\alpha\delta} M^{\mathcal{C}}_{\gamma\beta}\right)\widetilde{P}_l(\tau'_\alpha - \tau_\beta)\widetilde{P}_{l'}(\tau'_\gamma - \tau_\delta)e^{\mathrm{i}\omega_m(\tau'_\alpha - \tau_\delta)}\delta_{\lambda'_\alpha,A}\delta_{\lambda_\beta,B}\delta_{\lambda'_\gamma,C}\delta_{\lambda_\delta,D} \right\rangle, \tag{C24}$$

where $\widetilde{P}$ is defined in (C20).

We note that the measurement can be factorized to speed up the measurement process. In the Legendre measurement, only the part involving the first product of M matrices factorizes, as can be seen from (C24). Note, however, that the second product of M matrices merely generates crossing symmetry, so that the full information on this quantity is already contained in the first term. Hence this symmetry can be reconstructed after the simulation. In the one-band case, the second product is proportional to $\delta_{\sigma\sigma'}$, so that the $G^{(4)\uparrow\downarrow}$ component can be measured directly. For the $G^{(4)\uparrow\uparrow}$ component, we only measure the term proportional to $M^{\mathcal{C}}_{\uparrow}M^{\mathcal{C}}_{\uparrow}$ and construct this component by antisymmetrization afterwards.

APPENDIX D: ACCUMULATION FORMULA FOR THE CT-INT AND CT-AUX ALGORITHMS

Using a notation in analogy to the previous section, the expansion of the partition function Z, Eqs. (C1)–(C3), in the continuous-time interaction expansion (CT-INT) method[7] is given by

$$Z = \sum_{n\geqslant 0}\int\prod_{i=1}^{n} d\tau_i \sum_{\substack{\lambda_{2i-1},\lambda'_{2i-1}\\ \lambda_{2i},\lambda'_{2i}}} w(n,\{\lambda_j,\lambda'_j,\tau_j\}) \tag{D1}$$

$$w(n,\{\lambda_j,\lambda'_j,\tau_j\}) \equiv \frac{1}{n!}\det_{1\leqslant i,j\leqslant 2n}\left[G_{0\lambda_i,\lambda'_j}(\bar{\tau}_i-\bar{\tau}_j)\right] \times\prod_{i=1}^{n} U_{\lambda_{2i-1}\lambda'_{2i-1}\lambda_{2i}\lambda'_{2i}}, \tag{D2}$$

where $\bar{\tau}_i \equiv \tau_{\lfloor (i+1)/2\rfloor}$ and we have assumed the interaction part of the Hamiltonian to be of the form $H_{\rm int}(\{c^\dagger_A,c_A\}) = \sum_{ABCD} U_{ABCD}c^\dagger_A c_B c^\dagger_C c_D$ and $A=(a,\sigma)$ is a generic index with a being the orbital or site index and $\sigma=\uparrow,\downarrow$ the spin index.

In the CT-INT algorithm, we propose to measure the Legendre coefficients of $S \equiv \Sigma G$ based on the self-energy binning measurement originally introduced for the continuous-time auxiliary field (CT-AUX) algorithm.[10] Introducing the matrix

$$\hat{G}_0(\mathcal{C})_{ij} = G_{0\lambda_i\lambda'_j}(\bar{\tau}_i-\bar{\tau}_j) \tag{D3}$$

and its inverse, $M^{\mathcal{C}} \equiv (\hat{G}_0(\mathcal{C}))^{-1}$, the self-energy binning measurement for the CT-INT can be written as

$$S_{AB}(\tau) = -\left\langle\sum_{\alpha\beta=1}^{2n}\delta(\tau-\bar{\tau}_\alpha)\delta_{A\lambda'_\alpha}M^{\mathcal{C}}_{\alpha\beta}G^0_{\lambda_\beta B}(\bar{\tau}_\beta)\right\rangle. \tag{D4}$$

This can be straightforwardly transformed to a measurement in the Legendre basis by applying (2):

$$S_{AB,l} = -\sqrt{2l+1}\left\langle\sum_{\alpha\beta=1}^{2n}\delta_{A\lambda'_\alpha}P_l(x(\bar{\tau}_\alpha))M^{\mathcal{C}}_{\alpha\beta}G^0_{\lambda_\beta B}(\bar{\tau}_\beta)\right\rangle. \tag{D5}$$

An analogous formula also applies to the CT-AUX.

In practice, translational invariance may be used to generate multiple estimates for S within a given configuration. The Green's function is obtained by transforming S to Matsubara representation and using Dyson's equation. The moments of G are straightforwardly computed from the moments of ΣG and the knowledge of those of G_0.

APPENDIX E: EXPLICIT FORMULA FOR T_{nl} AND ITS HIGH FREQUENCY EXPANSION

The transformation matrix from the Legendre to the Matsubara representation is

$$T_{nl} \equiv \frac{\sqrt{2l+1}}{\beta}\int_0^\beta d\tau e^{i\nu_n\tau}P_l[x(\tau)], \tag{E1}$$

where ν_n is a fermionic Matsubara frequency and l is the Legendre index. Using (A7) and introducing the reduced frequencies $\bar{\nu}_n = \beta\nu_n = (2n+1)\pi$, we find

$$T_{nl} = (-1)^n\, i^{l+1}\sqrt{2l+1}\; j_l\left(\frac{\bar{\nu}_n}{2}\right). \tag{E2}$$

Note that T_{nl} is actually independent of β.

T_{nl} is a unitary transformation, as can be check explicitly using the Poisson summation formula and the orthogonality of the Legendre polynomials (A3),

$$\sum_{n\in\mathbb{Z}} T^*_{nl}T_{nl'} = \frac{\sqrt{2l+1}\sqrt{2l'+1}}{\beta}\int\!\!\int_0^\beta d\tau\, d\tau' \times P_l[x(\tau)]P_{l'}[x(\tau')]\underbrace{\frac{1}{\beta}\sum_{n\in\mathbb{Z}}e^{-i\nu_n(\tau-\tau')}}_{=\delta(\tau-\tau')}$$
$$= \sqrt{2l+1}\sqrt{2l'+1}\int_{-1}^{1}\frac{dx}{2}\,P_l(x)P_{l'}(x)$$
$$= \delta_{ll'}. \tag{E3}$$

We will now deduce the coefficients $t_l^{(p)}$ of the expansion of T_{nl},

$$T_{nl} = \sum_{p\geqslant 1}\frac{t_l^{(p)}}{(i\bar{\nu}_n)^p}. \tag{E4}$$

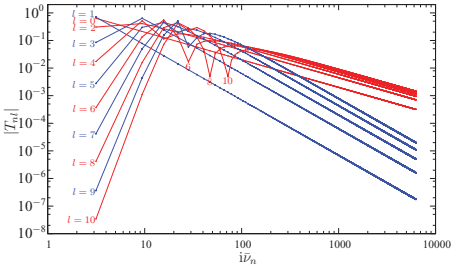

FIG. 11. (Color online) $|T_{nl}|$ for the first even (red) and odd (blue) Legendre coefficients. The high-frequency tail is reproduced correctly by $t_l^{(p)}$.

This is straightforwardly done from a corresponding representation of the Bessel function, cf., e.g., Ref. 36, Sec. 10.1,

$$j_l(z) = z^{-1}\left\{\sin(z-\pi l/2)\sum_{k=0}^{\lfloor \frac{l}{2}\rfloor}(-1)^k\frac{(l+2k)!(2z)^{-2k}}{(2k)!(l-2k)!} + \cos(z-\pi l/2)\sum_{k=0}^{\lfloor \frac{l-1}{2}\rfloor}(-1)^k\frac{(l+2k+1)!(2z)^{-2k-1}}{(2k+1)!(l-2k-1)!}\right\}. \quad \text{(E5)}$$

For the case at hand, this gives

$$T_{nl} = -i^l 2\sqrt{2l+1}\left\{\cos\left(\frac{l}{2}\pi\right)\sum_{k=0}^{\lfloor \frac{l}{2}\rfloor}\frac{(l+2k)!}{(2k)!(l-2k)!}\frac{1}{(\mathrm{i}\bar{\nu}_n)^{2k+1}} + \mathrm{i}\sin\left(\frac{l}{2}\pi\right)\sum_{k=0}^{\lfloor \frac{l-1}{2}\rfloor}\frac{(l+2k+1)!}{(2k+1)!(l-2k-1)!}\frac{1}{(\mathrm{i}\bar{\nu}_n)^{2k+2}}\right\}. \quad \text{(E6)}$$

The two sums can be combined to

$$T_{nl} = 2\sqrt{2l+1}\sum_{p=1}^{l+1}\frac{(l+p-1)!}{(p-1)!(l-p+1)!}\frac{(-1)^p}{(\mathrm{i}\bar{\nu}_n)^p}\delta_{p+l,\mathrm{odd}}, \quad \text{(E7)}$$

which immediately provides the coefficients $t_l^{(p)}$ of (E4),

$$t_l^{(p)} = (-1)^p 2\sqrt{2l+1}\frac{(l+p-1)!}{(p-1)!(l-p+1)!}\delta_{p+l,\mathrm{odd}}. \quad \text{(E8)}$$

Figure 11 shows T_{nl} for the first Legendre coefficients plotted against the fermionic Matsubara frequency $\mathrm{i}\bar{\nu}_n$. The doubly logarithmic plot clearly shows the high-frequency $1/\mathrm{i}\bar{\nu}_n$ behavior for the even and the $1/(\mathrm{i}\bar{\nu}_n)^2$ behavior for the odd coefficients. One can see that, as expected, the structure at very high frequencies is only carried by polynomials with large values of l.

[1] A. Georges, G. Kotliar, W. Krauth, and M. J. Rozenberg, Rev. Mod. Phys. **68**, 13 (1996).
[2] T. Maier, M. Jarrell, T. Pruschke, and M. H. Hettler, Rev. Mod. Phys. **77**, 1027 (2005).
[3] A. Toschi, A. A. Katanin, and K. Held, Phys. Rev. B **75**, 045118 (2007).
[4] A. N. Rubtsov, M. I. Katsnelson, and A. I. Lichtenstein, Phys. Rev. B **77**, 033101 (2008).
[5] H. Hafermann, S. Brener, A. Rubtsov, M. Katsnelson, and A. Lichtenstein, JETP Lett. **86**, 677 (2008).
[6] H. Hafermann, G. Li, A. N. Rubtsov, M. I. Katsnelson, A. I. Lichtenstein, and H. Monien, Phys. Rev. Lett. **102**, 206401 (2009).
[7] A. N. Rubtsov, V. V. Savkin, and A. I. Lichtenstein, Phys. Rev. B **72**, 035122 (2005).
[8] P. Werner, A. Comanac, L. de' Medici, M. Troyer, and A. J. Millis, Phys. Rev. Lett. **97**, 076405 (2006).
[9] P. Werner and A. J. Millis, Phys. Rev. B **74**, 155107 (2006).
[10] E. Gull, P. Werner, O. Parcollet, and M. Troyer, Europhys. Lett. **82**, 57003 (2008).
[11] E. Gull, A. J. Millis, A. I. Lichtenstein, A. N. Rubtsov, M. Troyer, and P. Werner, Rev. Mod. Phys. **83**, 349 (2011).
[12] A. N. Rubtsov, M. I. Katsnelson, A. I. Lichtenstein, and A. Georges, Phys. Rev. B **79**, 045133 (2009).
[13] G. Li, H. Lee, and H. Monien, Phys. Rev. B **78**, 195105 (2008).
[14] S. Brener, H. Hafermann, A. N. Rubtsov, M. I. Katsnelson, and A. I. Lichtenstein, Phys. Rev. B **77**, 195105 (2008).
[15] A. Weiße, G. Wellein, A. Alvermann, and H. Fehske, Rev. Mod. Phys. **78**, 275 (2006).
[16] A. Holzner, A. Weichselbaum, I. P. McCulloch, U. Schollwöck, and J. von Delft, Phys. Rev. B **83**, 195115 (2011).
[17] E. Gull, P. Werner, A. Millis, and M. Troyer, Phys. Rev. B **76**, 235123 (2007).
[18] G. Kotliar, S. Y. Savrasov, K. Haule, V. S. Oudovenko, O. Parcollet, and C. A. Marianetti, Rev. Mod. Phys. **78**, 865 (2006).
[19] K. Haule, Phys. Rev. B **75**, 155113 (2007).
[20] H. A. Bethe, Proc. R. Soc. London, Ser. A **150**, 552 (1935).
[21] M. Ferrero and O. Parcollet, TRIQS: "a Toolkit for Research on Interacting Quantum Systems" [http://ipht.cea.fr/triqs].
[22] O. Gunnarsson, G. Sangiovanni, A. Valli, and M. W. Haverkort, Phys. Rev. B **82**, 233104 (2010).
[23] B. Amadon, F. Lechermann, A. Georges, F. Jollet, T. O. Wehling, and A. I. Lichtenstein, Phys. Rev. B **77**, 205112 (2008).
[24] M. Aichhorn, L. Pourovskii, V. Vildosola, M. Ferrero, O. Parcollet, T. Miyake, A. Georges, and S. Biermann, Phys. Rev. B **80**, 085101 (2009), see Appendix A and references therein.
[25] B. Amadon, S. Biermann, A. Georges, and F. Aryasetiawan, Phys. Rev. Lett. **96**, 066402 (2006).
[26] L. Boehnke and F. Lechermann, e-print arXiv:1012.5943 [cond-mat.str-el].
[27] J. Kunes, Phys. Rev. B **83**, 085102 (2011).
[28] H. J. Vidberg and J. W. Serene, J. Low Temp. Phys. **29**, 179 (1977).
[29] R. Preuss, W. Hanke, C. Gröber, and H. G. Evertz, Phys. Rev. Lett. **79**, 1122 (1997).
[30] S. Hochkeppel, F. F. Assaad, and W. Hanke, Phys. Rev. B **77**, 205103 (2008).
[31] A. Erdélyi, *Higher Transcendental Functions* (McGraw-Hill, New York, 1953).
[32] B. Bauer, L. D. Carr, H. G. Evertz, A. Feiguin, J. Freire, S. Fuchs, L. Gamper, J. Gukelberger, E. Gull, S. Guertler, A. Hehn, R. Igarashi, S. V. Isakov, D. Koop, P. N. Ma, P. Mates, H. Matsuo,

O. Parcollet, G. Pawłowski, J. D. Picon, L. Pollet, E. Santos, V. W. Scarola, U. Schollwöck, C. Silva, B. Surer, S. Todo, S. Trebst, M. Troyer, M. L. Wall, P. Werner, and S. Wessel, J. Stat. Mech.: Theory Exp. (2011) P05001.

[33] I. S. Gradshteyn, I. M. Ryzhik, A. Jeffrey, and D. Zwillinger, *Table of Integrals, Series, and Products*, 6th ed. (Academic, Amsterdam, 2000).

[34] E. T. Whittaker and G. N. Watson, *A Course of Modern Analysis*, 4th ed. (Cambridge University Press, Cambridge, 1927).

[35] J. P. Boyd, *Chebyshev and Fourier Spectral Methods*, 2nd ed. (Dover, New York, 2001).

[36] M. Abramowitz and I. A. Stegun, *Handbook of Mathematical Functions with Formulas, Graphs, and Mathematical Tables*, 10th ed. (Dover, New York, 1964).

2.3 On the CT-Hyb algorithm

To round up the set of tools used in this work, this section will briefly introduce the hybridization expansion continuous time (CT-Hyb) Quantum Monte Carlo (QMC) algorithm [WCD+06, WM06, GML+11] used to solve the DMFT impurity problem. During the DMFT self-consistency loop, CT-Hyb is used to calculate the impurity Green's function. After the self-consistency is reached, additionally the two-particle Green's function is measured.

The accumulation formulas for both quantities in general and a Legendre representation thereof in particular have been derived in appendix C of [BHF+11] reprinted in the previous section. Unlike other derivations for the accumulation formula for the one-particle Green's function, that are introduced ad-hoc [WM06] or take a round trip through the bath Green's functions T-matrix [Hau07], the derivation in [BHF+11] stays within an closed path integral formulation of the impurity problem and has the advantage of being easily generalized to the two-particle Green's function or higher ones.

In a similar manner, this section introduces a closed derivation of the CT-Hyb algorithm, where existing derivations [WCD+06, GML+11] have to rely on combinatorial arguments. The derivation borrows the basic structure and arguments from the derivation of the dual fermion (DF) formalism [RKL08, HBR+08, RKLG09]. It is based on discussions held with A. Rubtsov in Jülich in 2011.

For later reference the Hubbard-Stratonovich Transformation (HST)

$$e^{\bar{c}_\alpha b_{\alpha\beta} A_{\beta\gamma} b_{\gamma\delta} c_\delta} = \det A \int \mathcal{D}\left[\bar{f} f\right] e^{-f_\alpha A^{-1}_{\alpha\beta} f_\beta + \bar{f}_\alpha b_{\alpha\beta} c_\beta + \bar{c}_\alpha b_{\alpha\beta} f_\beta} \tag{2.4}$$

The action for the Anderson Impurity model (AIM) can be decomposed into the free atom part and the hybridization

$$S_{\mathrm{imp}}[\bar{c}, c] = S_{\mathrm{at}}[\bar{c}, c] - \int d\tau d\tau' \bar{c}_\tau \Delta_{\tau\tau'} c_{\tau'} \ .$$

Applying the HST equation (2.4) to the path integral for the partition function with $A = \Delta$ and $b_{\alpha\beta} = \delta_{\alpha\beta}$ yields (integrals over τ always go from 0 to the inverse temperature β and orbital indices are neglected for now)

$$\begin{aligned}\mathcal{Z}_{\mathrm{imp}} &= \int \mathcal{D}\left[\bar{c}c\right] e^{-S_{\mathrm{imp}}[\bar{c},c]} \\ &= \det\Delta \int \mathcal{D}\left[\bar{c}c\right] \mathcal{D}\left[\bar{f}f\right] e^{-S_{\mathrm{at}}} e^{-\int d\tau d\tau' \bar{f}_\tau \Delta^{-1}_{\tau\tau'} f_{\tau'}} e^{\int d\tau' \bar{c}_{\tau'} f_{\tau'} + \int d\tau \bar{f}_\tau c_\tau}\end{aligned}$$

The idea is now to expand the last exponential and analytically solve the path integral for $\bar{f}f$ for each term in this expansion. Only terms in the sum with an equal number of f and $\bar{f}$ need to be taken into account for this.

$$\begin{aligned}\mathcal{Z}_{\mathrm{imp}} =& \det\Delta \int \mathcal{D}\left[\bar{c}c\right] \mathcal{D}\left[\bar{f}f\right] e^{-S_{\mathrm{at}}[\bar{c},c]} e^{-\int d\tau d\tau' \bar{f}_\tau \Delta^{-1}_{\tau\tau'} f_{\tau'}} \\ & (1 + \frac{1}{2!} \int d\tau_1 d\tau_1' (\bar{c}_{\tau_1} f_{\tau_1} \bar{f}_{\tau_1'} c_{\tau_1'} + \bar{f}_{\tau_1} c_{\tau_1} \bar{c}_{\tau_1'} f_{\tau_1'} + \ldots) \\ =& \det\Delta \int \mathcal{D}\left[\bar{c}c\right] \mathcal{D}\left[\bar{f}f\right] e^{-S_{\mathrm{at}}[\bar{c},c]} e^{-\int d\tau d\tau' \bar{f}_\tau \Delta^{-1}_{\tau\tau'} f_{\tau'}} \\ & (1 + \frac{1}{2!} \int d\tau_1 d\tau_1' (-f_{\tau_1'} \bar{f}_{\tau_1} c_{\tau_1} \bar{c}_{\tau_1'} - f_{\tau_1} \bar{f}_{\tau_1'} c_{\tau_1'} \bar{c}_{\tau_1} + \ldots) \\ =& \det\Delta \int \mathcal{D}\left[\bar{c}c\right] \mathcal{D}\left[\bar{f}f\right] e^{-S_{\mathrm{at}}[\bar{c},c]} e^{-\int d\tau d\tau' \bar{f}_\tau \Delta^{-1}_{\tau\tau'} f_{\tau'}} \\ & \sum_k \frac{1}{k!} \int \cdots \int d\tau_1 d\tau_1' \ldots d\tau_k d\tau_k' (-1)^k f_{\tau_1'} \bar{f}_{\tau_1} \ldots f_{\tau_k'} \bar{f}_{\tau_k} c_{\tau_1} \bar{c}_{\tau_1'} \ldots c_{\tau_k} \bar{c}_{\tau_k'} \\ =& \mathcal{Z}_{\mathrm{at}} \sum_k \frac{1}{k!} \int \cdots \int d\tau_1 d\tau_1' \ldots d\tau_k d\tau_k' \qquad (2.6) \\ & (-1)^k \left\langle \mathcal{T} f_{\tau_1'} \bar{f}_{\tau_1} \ldots f_{\tau_k'} \bar{f}_{\tau_k} \right\rangle_{\Delta^{-1}} \left\langle \mathcal{T} c_{\tau_1} \bar{c}_{\tau_1'} \ldots c_{\tau_k} \bar{c}_{\tau_k'} \right\rangle_{\mathrm{at}}\end{aligned}$$

with

$$\begin{aligned}\left\langle A \right\rangle_{\mathrm{at}} =& \mathcal{Z}_{\mathrm{at}}^{-1} \int \mathcal{D}\left[\bar{c}c\right] A[\bar{c},c] e^{-S_{\mathrm{at}}[\bar{c},c]} \\ \left\langle B \right\rangle_{\Delta^{-1}} =& \mathcal{Z}_{\Delta^{-1}}^{-1} \int \mathcal{D}\left[\bar{f}f\right] B[\bar{f},f] e^{-\int d\tau d\tau' \bar{f}_\tau \Delta^{-1}_{\tau\tau'} f_{\tau'}}\end{aligned}$$

where

$$\mathcal{Z}_{\text{at}} = \int \mathcal{D}\left[\bar{c}c\right] e^{-S_{\text{at}}[\bar{c},c]}$$
$$\mathcal{Z}_{\Delta^{-1}} = \int \mathcal{D}\left[\bar{f}f\right] e^{-\int d\tau d\tau' \bar{f}_\tau \Delta^{-1}_{\tau\tau'} f_{\tau'}} = \frac{1}{\det \Delta}$$

The expectation value $\langle \mathcal{T}_\tau A \rangle_{\Delta^{-1}}$ is a 'free' expectation value in the sense that its action is quadratic in Grassmann variables. Using Wick's Theorem, equation (2.6) can be evaluated to

$$\mathcal{Z}_{\text{imp}} = \mathcal{Z}_{\text{at}} \underbrace{\sum_k \frac{(-1)^k}{k!} \int \cdots \int d\tau_1 d\tau'_1 \ldots d\tau_k d\tau'_k}_{\equiv \sum_\zeta} \underbrace{\det\left[\hat{\Delta}^k_\zeta\right] \left\langle \mathcal{T}_\tau c_{\tau_1} \bar{c}_{\tau'_1} \ldots c_{\tau_k} \bar{c}_{\tau'_k} \right\rangle_{\text{at}}}_{\equiv \mathrm{w}_\zeta}$$

$\hat{\Delta}^k_\zeta$ is the $k \times k$-matrix with elements $\left[\hat{\Delta}^k_\zeta\right]_{AB} = \Delta(\tau_A, \tau'_B)$, $i, j \leq k$ where the configurations of τ's and τ''s (and possibly orbital indices) is encoded in the configuration ζ.

This establishes an formalism that expresses the impurity partition function as a sum over weights w_ζ of configurations ζ. How this can be cast into a Monte Carlo algorithm has been discussed before [WCD+06, WM06, GML+11] and will not be reviewed here.

All calculations in this work were performed using the TRIQS software package [FP], supplemented by code to measure and handle the two-particle Green's function and evaluate lattice susceptibilities.

Three

Susceptibilities

Even after some numerical algorithm provides an approximation to the susceptibility tensor

$$\chi^{\sigma\sigma'}_{ijkl}(\mathbf{q}, \mathrm{i}\omega_n) = -\int d(\mathbf{r}-\mathbf{r}')d(\tau-\tau')e^{\mathrm{i}\mathbf{q}(\mathbf{r}-\mathbf{r}')}e^{\mathrm{i}\omega_n(\tau-\tau')} \left\langle \mathcal{T}_\tau c^\dagger_{\sigma i}(\mathbf{r},\tau)c_{\sigma j}(\mathbf{r},\tau)c^\dagger_{\sigma' k}(\mathbf{r}',\tau')c_{\sigma' l}(\mathbf{r}',\tau') \right\rangle$$

one is still left with too many numbers to make sense of. The static physical susceptibility alone for a three orbital system still has 324 components (one case discussed later chapter 7 even has nine 'orbital' indices, thus 26244 components in the susceptibility tensor) plus a potentially intricate wave vector dependence $\mathbf{q}$, which however is not addressed in this chapter and thus dropped for the sake of clarity of the equations.

A route to the physical interpretation of susceptibilities that is complementary to the approach discussed towards the end of section 2.1, namely to integrate out the spin- and orbital indices in a way to gain one of the conventional observables, will be discussed in this chapter.

3.1 Extracting dominant contributions to the susceptibility tensor

Consider the eigendecomposition of the tensor $\chi^{\sigma\sigma'}_{ijkl}(\omega = 0)$ for the static case written in superindices $\alpha = \{\sigma ij\}$ and $\beta = \{\sigma' lk\}$.

$$\chi_{\alpha\beta} = \sum_l V^{(l)*}_\alpha \chi^{(l)} V^{(l)}_\beta \ ,$$

where $\chi^{(l)}$ are the eigenvalues of $\chi_{\alpha\beta}$ and $V^{(l)}_\alpha$ are the components of the eigenvector associated with the eigenvalue $\chi^{(l)}$. For the real symmetric matrix $\chi_{\alpha\beta}$ this is easily achieved.

With that, the susceptibility eigenvalues can be related to fluctuations of eigenmodes

$$\begin{aligned}
\chi^{(l)} &= \sum_{\alpha\beta} V^{(l)}_\alpha \chi_{\alpha\beta} V^{(l)*}_{l\beta} \\
&= -\sum_{\alpha\beta} V^{(l)}_\alpha \left\langle \mathcal{T}_\tau \hat{n}_\alpha \hat{n}_\beta \right\rangle_{\omega=0} V^{(l)*}_{l\beta} \\
&= -\Big\langle \mathcal{T}_\tau \underbrace{\sum_\alpha V^{(l)}_\alpha \hat{n}_\alpha}_{\hat{V}^{(l)}} \underbrace{\sum_\beta V^{(l)*}_\beta \hat{n}_\beta}_{\hat{V}^{(l)\dagger}} \Big\rangle_{\omega=0} \ ,
\end{aligned} \tag{3.1}$$

where $\hat{n}_\alpha(\tau) = c^\dagger_{\sigma i}(\tau) c_{\sigma j}(\tau)$ and $\hat{n}_\beta(\tau') = c^\dagger_{\sigma' l}(\tau') c_{\sigma' k}(\tau')$.

If the system under consideration is close to a phase transition with wave vector $\mathbf{Q}$, the susceptibility tensor can well be approximated by just taking into account the largest eigenvalue $\chi^{\max}$, at the same time giving an explicit expression for the operator $\hat{V}^{\max}$, the fluctuation of which diverges, giving the easiest excitable state. Comparing equation (3.1) to equation (2.2) makes clear that $\hat{V}^{\max}$ is just a special choice of the $\delta\hat{X}_\Gamma$ used there (and $\hat{V}^{\max\dagger}$ for $\delta\hat{X}'_\Delta$). With that, to first order in the field $F'^{\max}$, that couples $\hat{V}^{\max}$ to the Hamiltonian, equation (2.1) becomes

$$\left\langle \hat{V}^{\max}(\mathbf{Q}, 0) \right\rangle = \chi^{\max}(\mathbf{Q}, 0) F'^{\max}(\mathbf{Q}, 0) \ .$$

Consequently, $\left\langle \hat{V}^{\max}(\mathbf{Q}, 0) \right\rangle$ is the order parameter of the phase transition when $\chi^{\max}$ diverges.

Independently, Kuneš *et al.* [KA14] used a similar eigenanlaysis.

3.2 The simple case of one orbital per site

The eigendecomposition explained above becomes particularly easy in the case of a single orbital per site in a paramagnetic state. Only spin degrees of freedom enter ($\alpha = \sigma$, $\beta = \sigma'$), which then has the form

$$\chi_{\alpha\beta} = \begin{array}{c} \\ \uparrow \\ \downarrow \end{array} \begin{array}{c} \begin{array}{cc} \uparrow & \downarrow \end{array} \\ \begin{pmatrix} A & B \\ B & A \end{pmatrix} \end{array},$$

with $A, B \in \mathbb{R}$. This matrix has eigenvalues and eigenvectors

$$\begin{pmatrix} A & B \\ B & A \end{pmatrix} \begin{pmatrix} \sqrt{1/2} \\ \sqrt{1/2} \end{pmatrix} = \underbrace{(A+B)}_{\equiv 2\chi^{\mathrm{c}}} \underbrace{\begin{pmatrix} \sqrt{1/2} \\ \sqrt{1/2} \end{pmatrix}}_{\equiv \sqrt{1/2}\delta n}$$

$$\begin{pmatrix} A & B \\ B & A \end{pmatrix} \begin{pmatrix} \sqrt{1/2} \\ -\sqrt{1/2} \end{pmatrix} = \underbrace{(A-B)}_{\equiv \frac{\hbar^2}{2}\chi^{\mathrm{m}}} \underbrace{\begin{pmatrix} \sqrt{1/2} \\ -\sqrt{1/2} \end{pmatrix}}_{\equiv \frac{\sqrt{2}}{\hbar} S_z}.$$

Only charge- and spin-fluctuations are possible in such a system in the longitudinal channel. Correspondingly, the only possible ordered states are magnetic and charge-ordered states. Additionally, $\chi_{\alpha\beta}$ has a $\mathbf{q}$-dependence that allows to distinguish between e.g. ferromagnetic and anti-ferromagnetic fluctuations.

Four

Incommensurate spin susceptibility in Sr_2RuO_4

The body-centered tetragonal structure Sr_2RuO_4 attained a lot of attention with the mid nineties due to the discovery of superconductivity [MHY+94] that, while at very low temperatures below 1K, is an interesting research ground due to it's unconventional character similar to the cuprate superconductors, yet in an undoped material.

Interest was renewed by the prediction [MS99] from model-like random phase approximation (RPA) calculations and subsequent experimental verification [SBB+99] from inelastic neutron scattering (INS) measurements of a strong peak in the spin susceptibility at the incommensurate Q_i-point in the Brillouin zone (see figure 4.1 for the notation).

It is still an widely open question to which extend the different orbitals contribute to the physics of the system. Random phase approximation (RPA) comes to the conclusion [MS99, BSB+02] that a pure nesting scenario in the quasi-onedimensional sheets in the Fermi surface are solely responsible for the incommensurate spin susceptibility, which originate from d_{xz}- and d_{yz}-bands respectively for the sheet expanding in y- and in x-direction. At Q_i, these nesting conditions meet to form a peak. Recent renormalization group studies [HRZ13] have revived this argument to discuss the mutual exclusion of spin-density wave and superconductivity in context to the dimensionality of the partaking orbitals, assigning the two-dimensional Fermi surface of

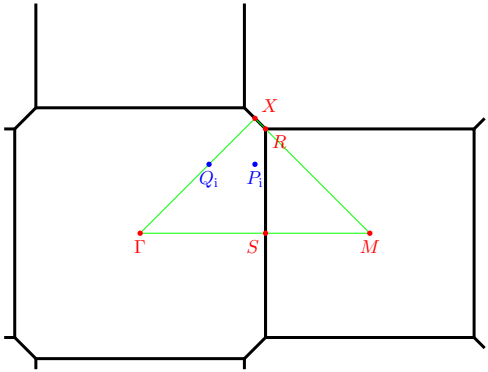

Figure 4.1: $\mathbf{k}_z = 0$-cut through the Brillouin zone of Sr_2RuO_4 with the high-symmetry points used in the text. The Q_i point is the position of the incommensurate magnetic peak and P_i is point where certain approximations also see an elevated susceptibility

the d_{xy} band (conventionally called the γ-surface) as the source of the p-wave pairing orderparameter. This seems to be in line with recent inelastic neutron scattering experiments by Iida *et al.* [IKK+11] that found the incommensurate peak still well pronounced at room temperature and from this temperature dependence drew the conclusion that the magnetic and superconducting properties are not related.

Yet, the finding of additional features throughout the Brillouin zone, INS data suggesting a peak near $\mathbf{q} = (0.15, 0.15)$ (in units of the in-plane reciprocal unit vectors[1]) as well as a delicate shoulder structure [BSB+02] of the peaks, hint that the physics is more complicated

[1]The notation in this Brillouin zone is ambiguous at best. Often (e.g. [BSB+02]), this point is denoted $\mathbf{q} = (0.15, 0.15, 0)$, which however is not entirely true because the first and second reciprocal unit vector carry a q_z component in this body-centered tetragonal lattice, which would lay $\mathbf{q} = (0.15, 0.15, 0)$ away from the intended $q_z = 0$-plane. To avoid confusion and since this work only discusses points within this plane, the third component will be dropped. Thus, to name some points $M = (1, 0)$, $X = (0.5, 0.5)$ and $Q_i = (0.3, 0.3)$.

than a simple nesting picture.

While spin-orbit coupling might play a role for the overall physical description of Sr_2RuO_4, Ng and Sigrist demonstrated from tight binding calculations including spin-orbit coupling [NS00] that it is of minor relevance for the qualitative structure of the incommensurate peak in the spin susceptibility. Corresponding experimental work [BSS$^+$04] supports this qualitative view, finds however, that peak intensities differ strongly between in-plane and out-of-plane susceptibility. Correspondingly, the following investigations will disregard spin-orbit coupling as a first step. This might be revisited in future work.

The numerical calculations of this material presented here serves two purposes. Firstly, calculating susceptibilities in an approximation beyond RPA for this inherent three-orbital problem is a valuable missing piece of information and it will indeed be shown in this chapter that not only contributions can be made to the investigation of the intriguing peak-structure throughout the Brillouin zone but also the orbital resolution of the dominant spin-like susceptibility shows a non-trivial behavior. Secondly (yet first in sequence), this material will serve as a demonstration case for a further development of the numerical benefit of using the Legendre polynomial basis [BHF$^+$11] to calculate not only static but also dynamical lattice susceptibilities.

This relevant additional improvement of the calculation of susceptibilities for non-static bosonic Matsubara frequencies came up only after the publication of the use of Legendre polynomials [BHF$^+$11]. It makes use of the some analytically known properties of the dynamical generalized susceptibility for elevated frequencies to further reduce the number of Legendre coefficients necessary to reliably calculate lattice susceptibilities. The susceptibilities for the investigation of Na_xCoO_2 presented in chapter 6 and specifically in reference [BL12] were still calculated without this improvement. For one orbital this is very well possible, albeit numerically a bit more tedious. When dynamical susceptibilities for Na_xCoO_2 were revisited and also calculated for lower temperatures later on in chapter 6 and reference [BL14], this improvement was used, yielding the smooth connection to the previous results

and more refined newer ones.

4.1 Numeric setup for Sr_2RuO_4

To gain an unbiased an accurate account of the kinetic part of the Hamiltonian, a density functional theory [Koh99] (DFT) calculation in its local density approximation [PW92] (LDA) flavour as implemented in the mixed-basis pseudopotential [MELFed] (MBPP) code. Structural data is taken from reference [WL93]. We proceed with LDA+dynamical mean field theory [APK$^+$97, LK98, KSH$^+$06] (LDA+DMFT) calculation, employing the projection onto a maximally localized Wannier basis [MV97] and using the rotationally invariant Slater-Kanamori local interaction parametrization suitable for the t_{2g}-shell [dMG11]

$$\mathcal{H}_{\text{int}} = (U - 3J_H)\frac{\hat{N}(\hat{N}-1)}{2} - 2J_{\text{H}}\mathbf{S}^2 - \frac{J_{\text{H}}}{2}\mathbf{L}^2 + \frac{5}{2}\hat{N}$$

with $\hat{N}$ the total charge operator, $\mathbf{S}$ the spin- and $\mathbf{L}$ the angular momentum operators. The parameters for the Coulomb interaction $U = 2.3$eV and Hund coupling $J_{\text{H}} = 0.4$eV were chosen in accordance with Mjavlje *et al.*, [MAM$^+$11] where these were determined to agree reasonably well with constrained RPA calculations [AIG$^+$04].

4.2 An addendum to the use of Legendre coefficients - Shifting frequencies

An account of analytical considerations for the structure of the generalized susceptibility in Matsubara frequency space mainly given in reference [RVT12] but also previously discussed in [LA11]. In the following it will be shown how this structure can be used to further

reduce the number of Legendre coefficients for elevated bosonic frequencies compared to the method detailed in [BHF+11] (which was reprinted in full on page 22). Following that, the benefit will be shown explicitly by performing convergence tests for Sr_2RuO_4. All figures in this section are for Sr_2RuO_4 modeled as discussed above and at the temperature $T = 290$K.

Equation (14) in reference [BHF+11]

$$\widetilde{\chi}(\mathrm{i}\nu_n, \mathrm{i}\nu_{n'}, \mathrm{i}\omega_m) = \sum_{l,l' \geq 0} T_{nl} \widetilde{\chi}_{ll'}(\mathrm{i}\omega_m) T^*_{n'l'}$$

and its inverse

$$\widetilde{\chi}_{ll'}(\mathrm{i}\omega_m) = \sum_{n,n' \in \mathbb{Z}} T^*_{nl} \widetilde{\chi}(\mathrm{i}\nu_n, \mathrm{i}\nu_{n'}, \mathrm{i}\omega_m) T_{n'l'}$$

with $\widetilde{\chi}_{ll'}(\mathrm{i}\omega_m)$ being the generalized susceptibility in mixed Legendre Matsubara basis and $\widetilde{\chi}(\mathrm{i}\nu_n, \mathrm{i}\nu_{n'}, \mathrm{i}\omega_m)$ in pure (conventional) Matsubara basis in fermionic ($\nu_n = (2n+1)\pi T$) and bosonic ($\omega_m = 2m\pi T$) Matsubara frequency. The unitary transformation

$$\begin{aligned} T_{nl} =& \frac{\sqrt{2l+1}}{\beta} \int_0^\beta d\tau e^{\mathrm{i}\nu_n \tau} P_l[x(\tau)] \\ =& (-1)^n \mathrm{i}^{l+1} \sqrt{2l+1} j_l \left(\frac{(2n+1)\pi}{2} \right) \end{aligned}$$

with $\beta = \frac{1}{T}$ the inverse temperature connects these quantities. The notation used in this section aligns to section 2.1 and [BHF+11], hence $P_l(x)$ is the lth Legendre polynomial, $x(\tau)$ is the linear mapping of the range $\tau \in [0; \beta]$ to the range $x \in [-1; 1]$ and $j_l(z)$ is the lth spherical Bessel function.

Orbital and spin indices are implicit in $\widetilde{\chi}_{ll'}(\mathrm{i}\omega_m)$ as well as $\widetilde{\chi}(\mathrm{i}\nu_n, \mathrm{i}\nu_{n'}, \mathrm{i}\omega_m)$ throughout this section. As the unitary transformation T_{nl} and the improvements thereof discussed here act solely on the fermionic (and bosonic) degrees of freedom but leave the orbital and spin-indices unaffected, those can be left out of the current discussion.

The susceptibilities are calculated as outlined in [BHF+11], by inverting the impurity Bethe-Salpeter equation (BSE) in the horizontal particle-hole channel to get the irreducible vertex of the impurity, which is subsequently used as an approximation for the lattice's irreducible vertex [ZH90, MJPH05] in the lattice's BSE to obtain the generalized susceptibility of the desired lattice wave-vector (equation (15) in [BHF+11])

$$\underline{\underline{\widetilde{\chi}}}^{-1}(\mathbf{q}, \mathrm{i}\omega_m) = \underline{\underline{\widetilde{\chi}}}_{\mathrm{imp}}^{-1}(\mathrm{i}\omega_m) - \underline{\underline{\widetilde{\chi}}}_{\mathrm{imp}}^{0\ -1}(\mathrm{i}\omega_m) + \underline{\underline{\widetilde{\chi}}}^{0-1}(\mathbf{q}, \mathrm{i}\omega_m)\ . \tag{4.1}$$

Like in [BHF+11], the double underline denotes the dependence on two fermionic Matsubara frequencies or Legendre coefficients. Naturally in a numerical treatment of these inversions the representing basis has to be truncated to a finite number of coefficients C and it must be taken care of the convergence of the general susceptibility of this number

$$\begin{aligned}\underline{\underline{\widetilde{\chi}}}(\mathbf{q}, \mathrm{i}\omega_m) &= \lim_{C\to\infty} [\underline{\underline{\widetilde{\chi}}}|_C](\mathbf{q}, \mathrm{i}\omega_m) \\ &= \lim_{C\to\infty} \left([\underline{\underline{\widetilde{\chi}_{\mathrm{imp}}}}|_C]^{-1}(\mathrm{i}\omega_m) - [\underline{\underline{\widetilde{\chi}^0_{\mathrm{imp}}}}|_C]^{-1}(\mathrm{i}\omega_m) + [\underline{\underline{\widetilde{\chi}^0}}|_C]^{-1}(\mathbf{q}, \mathrm{i}\omega_m) \right)^{-1}\ .\end{aligned}$$

When calculating the physical susceptibility (equation (19) in [BHF+11])

$$\begin{aligned}\chi(\mathbf{q}, \mathrm{i}\omega_m) \equiv& \left\langle \underline{\underline{\widetilde{\chi}}}(\mathbf{q}, \mathrm{i}\omega_m) \right\rangle \\ =& \lim_{C\to\infty} \left\langle \underline{\underline{\widetilde{\chi}}}|_C(\mathbf{q}, \mathrm{i}\omega_m) \right\rangle ,\end{aligned}$$

the empty bubble part, which can be computed numerically up to very high C can be separated to increase convergence

$$\chi(\mathbf{q}, \mathrm{i}\omega_m) = \lim_{C\to\infty} \left\langle \underline{\underline{\widetilde{\chi}}}|_C(\mathbf{q}, \mathrm{i}\omega_m) - \underline{\underline{\widetilde{\chi}^0}}|_C(\mathbf{q}, \mathrm{i}\omega_m) \right\rangle + \chi^0(\mathbf{q}, \mathrm{i}\omega_m)\ .$$

While this scheme does not change with an unitary transformation of the fermionic degrees of freedom, the details of tracing out those

does, yielding

$$\left\langle \underline{\underline{\widetilde{\chi}}}(\mathbf{q}, \mathrm{i}\omega_m) \right\rangle \equiv \frac{1}{\beta^2} \sum_{n,n' \in \mathbb{Z}} \widetilde{\chi}(\mathbf{q}, \mathrm{i}\nu_n, \mathrm{i}\nu_{n'}, \mathrm{i}\omega_m)$$

for the Matsubara case and

$$\left\langle \underline{\underline{\widetilde{\chi}}}(\mathbf{q}, \mathrm{i}\omega_m) \right\rangle \equiv \frac{1}{\beta^2} \sum_{l,l' \geq 0} (-1)^{l+l'} \sqrt{2l+1} \sqrt{2l'+1} \widetilde{\chi}_{ll'}(\mathbf{q}, \mathrm{i}\omega_m) \tag{4.2}$$

for the Legendre case and also the truncation is different

$$\underline{\underline{\widetilde{\chi}}}|_{\hat{n}}(\mathbf{q}, \mathrm{i}\omega_m) \equiv \widetilde{\chi}_{nn'}\big|_{-\frac{\hat{n}}{2} \leq n/n' < \frac{\hat{n}}{2}}(\mathbf{q}, \mathrm{i}\omega_m) \tag{4.3}$$

for the Matsubara case and

$$\underline{\underline{\widetilde{\chi}}}|_{\hat{l}}(\mathrm{i}\omega_m) \equiv \sum_{n,n' \in \mathbb{Z}} T^*_{nl} \widetilde{\chi}_{nn'}(\mathrm{i}\omega_m) T_{n'l'}\big|_{0 \leq l/l' < \hat{l}} = \widetilde{\chi}_{ll'}\big|_{0 \leq l/l' < \hat{l}} \tag{4.4}$$

for Legendre coefficients.

While the calculation of lattice susceptibilities following equation (4.1) sketches the use of the Legendre basis throughout this work and is also the test case for the following arguments, it is important to note that it is not limited to this use case. All diagrammatic schemes that can be mapped to matrix operations within one channel of two-particle properties can benefit from the Legendre basis without further ado. To this group of problems belong also i.e. the dynamical vertex approximation [TKH07] (DΓA) and the dual fermion [RKL08, HBR$^+$08, RKLG09] (DF) method in most of its manifestations including the ladder dual fermion approximation [HLR$^+$09] (LDFA). The qualitative arguments for the benefits of the Legendre basis relies solely on the general structure of the two-particle quantities, which does not differ throughout these approaches.

Figure 4.2 shows the Γ-point (uniform) static generalized magnetic susceptibility for the fixed orbital indices (3333) (3 here denotes the d_{xy}-orbital, which at the Γ-point is the most relevant one as will be discussed in section 4.4) in fermionic Matsubara coefficients and Legendre

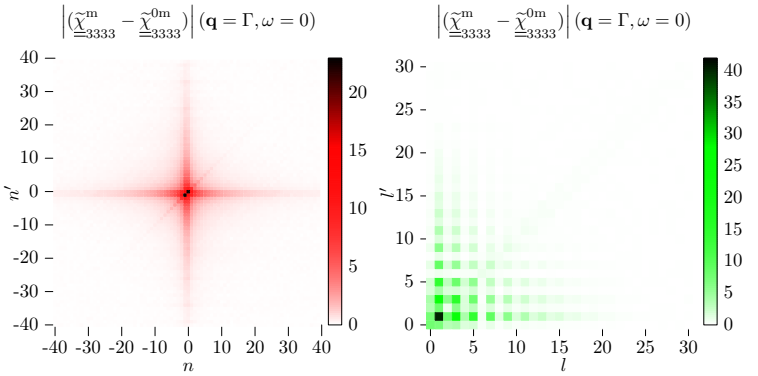

Figure 4.2: Static uniform generalized spin susceptibility in Matsubara frequencies (left) or Legendre coefficients (right) for the indicated orbital frequencies for $T = 290$K. Note the different number of coefficients in both plots

coefficients respectively. The empty bubble $\widetilde{\underline{\underline{\chi}}}^{0\mathrm{m}}$ has been subtracted to focus on the numerically demanding part.

For better comparability to the Legendre case, the Matsubara version is not shown against Matsubara frequencies $\mathrm{i}\nu_n$, but rather against its index n (thus using the notation $\widetilde{\chi}_{nn'}$). Note that figure 4.2 shows about seven times more coefficients for $\widetilde{\chi}_{nn'}$ than for $\widetilde{\chi}_{ll'}$.

It shows the static generalized susceptibility and thus touches ground with figure 8 of [BHF+11], yet for the more complicated material considered here. Accordingly, the convergence curves for these two cases in figure 4.3 (full symbols) qualitatively match those of figure 9 of [BHF+11]. Both figures show the convergence of the physical magnetic susceptibility against the number of coefficients used for each fermionic degree of freedom in the its calculation as it was sketched above. Both show that the Legendre basis yields a rapid saturation, while the Matsubara basis does not even allow for a reliable extrapolation still with many more coefficients. This is consistent with the

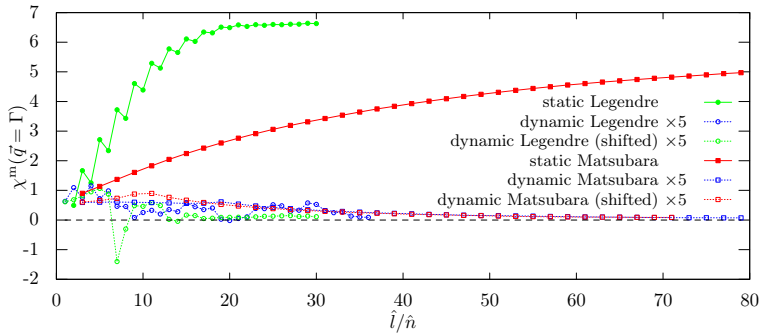

Figure 4.3: Convergence of the Γ-point spin susceptibility for Sr_2RuO_4 at $T = 290$K using the indicated bases. As an example for the dynamical susceptibility (dashed lines) $i\omega_{10} = i20T$ was chosen as in the preceding plots. The colors were chosen in correspondence to those too. For these parameters, the dynamical susceptibility is expected to be precisely zero [HvLK+14]. For the Matsubara convergence curves, only the symmetric points (odd number of coefficients) are used

decay of the generalized susceptibility in both bases in figure 4.2.

On the other hand, the dynamical generalized susceptibility in Matsubara coefficients has a peculiar structure with a broadened range of slow decay along the n- and n'-direction [RVT12], clearly visible in figure 4.4 and it also leaves a trace in the convergence curve of the dynamical susceptibility versus the number of Matsubara frequencies (empty blue symbols in figure 4.3), which hits a maximum around $\hat{n} = 20$, which is just where both maxima of $\widetilde{\chi}_{nn'}$ are included the truncated $\widetilde{\underline{\chi}}_{\hat{n}}$. After that the convergence takes the slow stance comparable to the static case, in line with the slow decay in the n and n' directions.. The Legendre coefficients carry relevant weight only within a well contained region as opposed to this gradual decay in three major directions. Following [HvLK+14], at the Γ-point the susceptibilities for Matsubara frequencies $i\omega_m$ with $m > 0$ are $\chi(\Gamma, i\omega_{m>0}) = 0$,

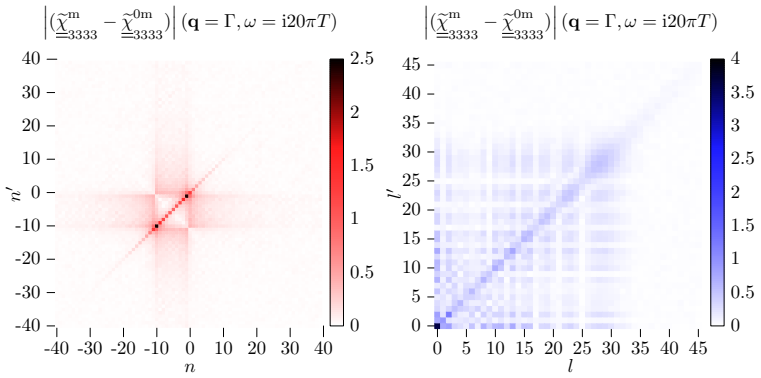

Figure 4.4: Dynamical ($m = 10$) uniform generalized spin susceptibility in Matsubara frequencies (left) or Legendre coefficients (right) for the indicated orbital frequencies. Note the different number of coefficients in both plots

which makes this an apt test case for the convergence of this quantity. Note how the point where figure 4.3 shows a well converged Legendre-calculated dynamical susceptibility, around $\hat{l} \approx 33$ in this case, coincides with the region of relevant weight in figure 4.4.

The structure of the dynamical Matsubara generalized susceptibility suggests to use a different a different truncation than proposed before in equation (4.3)

$$\underline{\underline{\bar{\chi}}}|_{\hat{n}}(\mathbf{q}, \mathrm{i}\omega_m) \equiv \widetilde{\chi}_{nn'}\big|_{-\frac{\hat{n}}{2}-m \leq n/n' < \frac{\hat{n}}{2}-m}(\mathbf{q}, \mathrm{i}\omega_m) \ ,$$

which follows the structure of $\widetilde{\chi}_{nn'}(\mathbf{q}, \mathrm{i}\omega_m)$. This has been employed and discarded before [Lui11], because while it turns in to the slowly decaying stance earlier as visible in the open red squares in figure 4.3 (already around $\hat{n} \approx \frac{m}{2}$, where the whole central structure is incorporated within the truncated region), this stance is just as bad as in the unshifted case.

This changes completely however when turning again to the Legendre basis, considering a truncation in Legendre space of a shifted transformation, i.e. replacing equation (4.4) by

$$\underline{\underline{\bar{\chi}}}|_{\hat{l}}(\mathbf{q}, \mathrm{i}\omega_m) \equiv \sum_{n,n' \in \mathbb{Z}} \bar{T}^*_{2n+m+1,l} \widetilde{\chi}_{nn'}(\mathbf{q}, \mathrm{i}\omega_m) \bar{T}_{2n'+m+1,l'}\big|_{0 \le l,l' < \hat{l}} \,. \tag{4.5}$$

Therein,

$$\begin{aligned} \bar{T}_{o,l} \equiv & \frac{\sqrt{2l+1}}{\beta} \int_0^\beta d\tau e^{\mathrm{i}o\pi\frac{\tau}{\beta}} P_l(x(\tau)) \\ = & \sqrt{2l+1} \mathrm{i}^{o} \mathrm{i}^{l} j_l\left(\frac{o\pi}{2}\right) \end{aligned}$$

is the generalization of T_{nl} used before with $T_{nl} = \bar{T}_{2n+1,l}$. It is easy to check using the orthogonality of the Legendre polynomials, that $\bar{T}_{2n+m+1,l}$ is unitary for each fixed m, i.e.

$$\begin{aligned} \sum_n \bar{T}^*_{2n+m+1,l} \bar{T}_{2n+m+1,l'} &= \delta_{ll'} \\ \sum_l \bar{T}^*_{2n+m+1,l} \bar{T}_{2n'+m+1,l} &= \delta_{nn'} \end{aligned}$$

Please note that in equation (4.5) (just as in equation (4.4)), the n-sums are just formally executed, no approximation or truncation enters at that point. The only truncation is in Legendre basis. Instead, an accumulation formula for the shifted Legendre basis quantity $\underline{\underline{\bar{\chi}}}|_{\hat{l}}^{\mathrm{imp}}(\mathrm{i}\omega_m)$ can be readily derived from the accumulation formula in imaginary time (equation (C.23) in [BHF+11])

$$\begin{aligned} G^{(4)}_{ABCD}(\tau_{12}, \tau_{34}, \tau_{14}) = \frac{1}{\beta} \Big\langle & \sum_{\alpha\beta\gamma\delta=1}^{k} (M^\zeta_{\alpha\beta} M^\zeta_{\gamma\delta} - M^\zeta_{\alpha\delta} M^\zeta_{\gamma\beta}) \\ & \delta^-(\tau_{12} - \tau_{\alpha\beta}) \delta^-(\tau_{34} - \tau_{\gamma\delta}) \delta^+(\tau_{14} - \tau_{\alpha\delta}) \\ & \delta_{\lambda_\alpha, A} \delta_{\lambda_\beta, B} \delta_{\lambda_\gamma, C} \delta_{\lambda_\delta, D} \Big\rangle \,. \end{aligned}$$

$G^{(4)}$ refers to the two-particle Green's function, uppercase Latin letters to a complete set of local characterizing quantities (e.g. spin- and orbital indices), $\tau_{12} = \tau_1 - \tau_2'$, $\delta^{\pm}(\tau)$ is the $\frac{1}{T}$-(anti)periodic Dirac function, M^{ζ} is the inverse of the matrix $\hat{\Delta}(\zeta)_{ij} \equiv \Delta_{\lambda_i,\lambda_j'}(\tau_i - \tau_j')$ for the configuration $\zeta = (k, \lambda_j, \lambda_j', \tau_j, \tau_j')$, which in turn is composed of a perturbation order k and a set of spins/orbitals and imaginary times ($\{\lambda, \tau\}$) for the k creation operators and a set of spins/orbitals and imaginary times ($\{\lambda', \tau'\}$) for the k annihilation operators generated by the Markov process. $\Delta_{AB}(\tau)$ is the hybridization matrix of the impurity problem. All this is discussed in greater detail in appendix C of [BHF+11].

The simple dependence of imaginary time of just three δ functions allows for a easy transformation to a different basis, e.g. the Matsubara basis

$$G^{(4)}_{ABCD}(\mathrm{i}\nu_n, \mathrm{i}\nu_{n'}, \mathrm{i}\omega_m) = \frac{1}{\beta}\Big\langle \sum_{\alpha\beta\gamma\delta=1}^{k} (M^{\zeta}_{\alpha\beta}M^{\zeta}_{\gamma\delta} - M^{\zeta}_{\alpha\delta}M^{\zeta}_{\gamma\beta}) e^{\mathrm{i}\nu_n\tau_{\alpha\beta}} e^{\mathrm{i}\nu_{n'}\tau_{\gamma\delta}} e^{\mathrm{i}\omega_m\tau_{\alpha\delta}} \delta_{\lambda_\alpha,A}\delta_{\lambda_\beta,B}\delta_{\lambda_\gamma,C}\delta_{\lambda_\delta,D}\Big\rangle .$$

From there, the desired accumulation formula in the shifted Legendre basis is just obtained by applying the transformation equation (4.5)

$$\bar{G}^{(4)}_{ABCDll'}(\mathrm{i}\omega_m) = \frac{\sqrt{2l+1}\sqrt{2l'+1}}{\beta}(-1)^{l'+1} \Big\langle \sum_{\alpha\beta\gamma\delta=1}^{k} (M^{\zeta}_{\alpha\beta}M^{\zeta}_{\gamma\delta} - M^{\zeta}_{\alpha\delta}M^{\zeta}_{\gamma\beta}) \widetilde{P}_l(x(\tau_{\alpha\beta}))\widetilde{P}_{l'}(x(\tau_{\gamma\delta}) e^{-\mathrm{i}\frac{\omega_m}{2}(\tau_{\alpha\beta}+\tau_{\gamma\delta})} e^{\mathrm{i}\omega_m\tau_{\alpha\delta}} \delta_{\lambda_\alpha,A}\delta_{\lambda_\beta,B}\delta_{\lambda_\gamma,C}\delta_{\lambda_\delta,D}\Big\rangle .$$

Comparing that with the accumulation formula for non-shifted Legendre basis given in equation (C.24) in [BHF+11], the only difference

is a shift of the time associated with the third time difference

$$\tau_{\alpha\delta} \to \tau_{\alpha\delta} - \frac{\tau_{\alpha\beta} + \tau_{\gamma\delta}}{2} ,$$

which obviously has a negligible impact on the time for the numerical accumulation of this quantity. Yet, the numerical benefit is big,

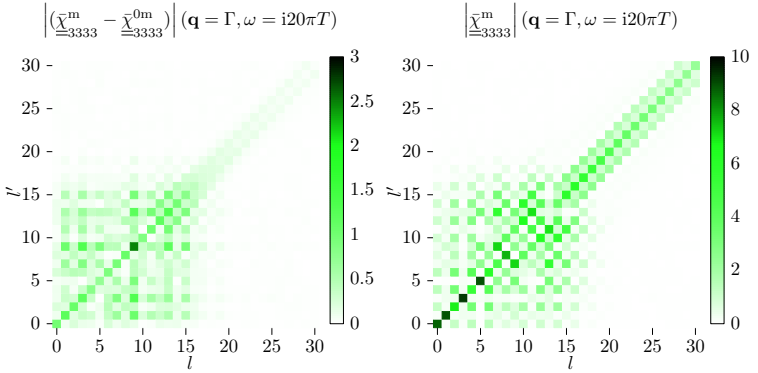

Figure 4.5: Dynamical ($m = 10$) uniform generalized spin susceptibility in shifted Legendre coefficients (left) and together with the empty bubble part (right) for the indicated orbital frequencies. Note the different number of coefficients in both plots and also compared to figure 4.4

as is clearly visible when comparing figure 4.5 to figure 4.4 (note the different number of coefficients used in both figures). The compact appearance is preserved, yet its size of this region in Legendre coefficients is further decreased, in the actual example from roughly 33 to as little as roughly 17 coefficients each for l and l'. In most cases it is not necessary to increase the number of Legendre coefficients for the dynamical case beyond that necessary already for $m = 0$ when calculating the susceptibility for a number of bosonic Matsubara frequencies sufficient to yield a physically sound analytic continuation [VS77] to the

real frequency domain. The right plot in figure 4.5 shows the structure of the whole generalized susceptibility $\underline{\underline{\widetilde{\chi}}}(\mathrm{i}\omega_{10}, \Gamma)$ including the trivial part which, as in the static case, adds primarily to a dominantly diagonal region, stabilizing the inversions to obtain this quantity. The convergence curve in figure 4.3 (empty green circles) is consequential.

The only additional points that need revisiting when compared to the scheme presented in [BHF+11] is the construction of the empty bubble part of the susceptibility $\underline{\underline{\bar{\chi}}}_{ll'}(\mathrm{i}\omega_m)$, which now also uses the shifted transformation $\bar{T}_{ol}$[2]

$$\bar{\chi}^0_{ll'}(\mathrm{i}\omega_m) = -\sum_{nn'} \bar{T}^*_{2n+m+1,l} G\Big(\mathrm{i}(2n+2m+1)\frac{\pi}{\beta}\Big) G\Big(\mathrm{i}(2n+1)\frac{\pi}{\beta}\Big) \bar{T}^*_{2n'+m+1,l'}$$

and the calculation of the physical susceptibility, which however turns out to stay unaltered compared to equation (4.2)

$$\Big\langle \underline{\underline{\bar{\chi}}}(\mathbf{q}, \mathrm{i}\omega_m) \Big\rangle \equiv \frac{1}{\beta^2} \sum_{l,l' \geq 0} (-1)^{l+l'} \sqrt{2l+1}\sqrt{2l'+1}\, \bar{\chi}_{ll'}(\mathbf{q}, \mathrm{i}\omega_m)$$

4.3 Dynamical spin susceptibility spectrum for Sr_2RuO_4

With the numerical instruments developed above, one is finally equipped to calculate the dynamical spin susceptibility for a realistically modeled system with the full t_{2g}-shell in the correlated subspace without the fear to include systematic errors due to truncation in Matsubara frequency coefficients that enter the analytic continuation in uncontrolled ways.

The temperatures used in the remainder of this chapter range down to $T = 193\mathrm{K}$ ($\beta = 60\frac{1}{e\mathrm{V}}$) which, while of course high above the super-

[2] This formula is to be understood as a template for these empty bubble susceptibilities. They appear as **q**-dependent as well as impurity quantities, correspondingly with the usual additional **k**-sums and **k**-dependent Green's functions or just with the impurity quantities. Details can be found in equation (16) of [BHF+11]

conducting transition temperature of few Kelvin, allows for a valuable insight into the spin-dynamics of the system.

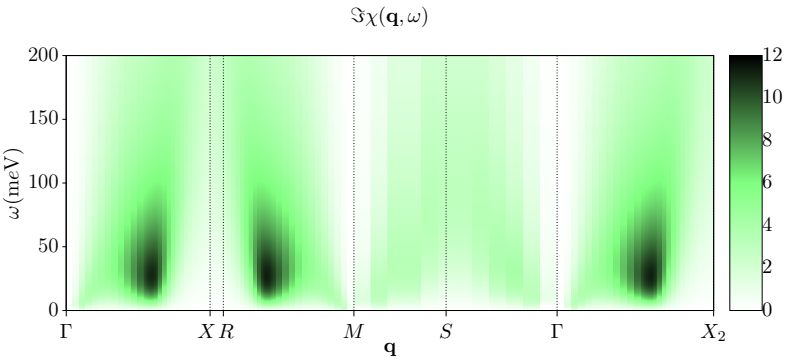

Figure 4.6: Dynamical spin susceptibility throughout the Brillouin-zone for $T = 290$K. The notation for the high-symmetry points is given in figure 4.1. The X_2-point lies above the X-point on level with the upper surface of the Brillouin zone

Figure 4.6 shows the dynamical spin susceptibility spectrum. Constant energy cuts through certain partial paths of this are at hand from INS measurements [BSB+02,IKK+11], that compare well on a qualitative level. The experimentally observed incommensurate peak in the dynamical susceptibility is clearly visible, it shows equally pronounced at the $\overline{\Gamma X}$-, the $\overline{XM}$- and the $\overline{\Gamma X_2}$-path. These points lie on the same q_z-line due to the sheared stacking of the Brillouin zones, so the relative similarity of these peaks just highlights the two-dimensionality of the material. The peak position at $\hat{\omega} \approx 27$meV is not resolved by but consistent with aforementioned INS data, which covers energy ranges up to 10meV.

4.4 Orbital contributions to the spin susceptibility

Inelastic neutron scattering experiments that were applied to Sr_2RuO_4 provide a measure for the magnetic spin susceptibility, while the calculation of the full susceptibility tensor $\chi^{\sigma\sigma'}_{ijkl}$ allows to determine the leading eigenmodes of the fluctuation independent of an experimental instruments fit to measure these. The corresponding tools were developed in section 3.1 and are congruously used on the static susceptibility in this section.

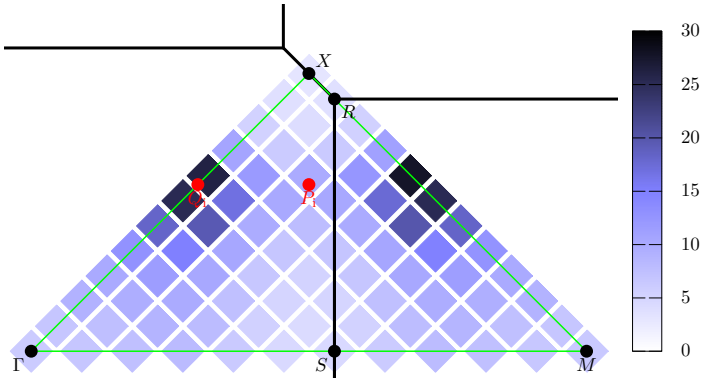

Figure 4.7: Map of the dominating eigenvalue in the irreducible wedge of the $q_z = 0$-Brillouin zone (figure 4.1) for $T = 193$K. The path used in figure 4.6 and figure 4.8 is marked in green

The dominant eigenvalue for each **q**-point for a rather low temperature $T = 193$K for the in-plane irreducible wedge of the Brillouin zone is shown in figure 4.7. Nicely seen are the two most prominent

features, the peaks at the discussed incommensurate point Q_i and its counterpart at on the $\overline{XM}$-path.

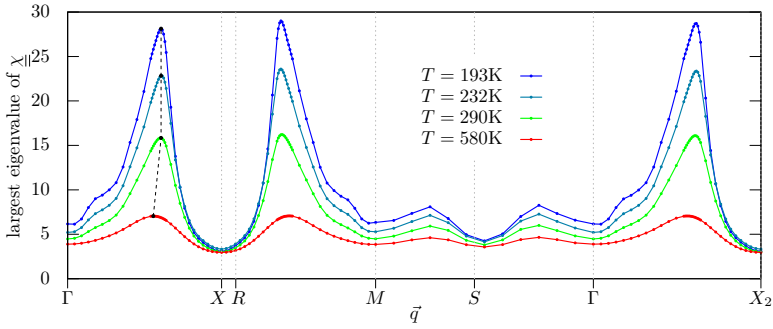

Figure 4.8: Dispersion of the dominant eigenvalue of the susceptibility tensor for several temperatures along the same way through the Brillouin zone that was used in figure 4.6.

A more refined account of the structure and in particular a evolution of the peak-structure with temperature can be found in figure 4.8. While for elevated temperatures ($T = 580$K, red curve) only a rather flat structure is visible (even there though the rather high background is noteworthy), only at lower temperatures develop the shoulder structure [BSB+02] at the $\overline{\Gamma X}$-path and asymmetric decay towards Γ-point and X-point. The determined peak position of $Q_\mathrm{i} = (0.30, 0.30)$ matches perfectly with experimental findings [BSB+02].

The orbital contributions to the dominant fluctuating eigenmode vary across the Brillouin zone. At the Γ-point, the dominant eigenvector (compare section 3.1) is (all results in this section are for

$T = 193\text{K}$)

$$V^{\max}(\mathbf{q}=\Gamma) = \begin{array}{cc} & \begin{array}{ccc} d_{xz} & d_{yz} & d_{xy} \end{array} \\ \uparrow \begin{array}{c} d_{xz} \\ d_{yz} \\ d_{xy} \end{array} & \begin{pmatrix} 0.33 & 0.00 & 0.00 \\ 0.00 & 0.34 & 0.00 \\ 0.00 & 0.00 & 0.52 \end{pmatrix} \\ & \\ & \begin{array}{ccc} d_{xz} & d_{yz} & d_{xy} \end{array} \\ \downarrow \begin{array}{c} d_{xz} \\ d_{yz} \\ d_{xy} \end{array} & \begin{pmatrix} -0.36 & 0.00 & 0.00 \\ 0.00 & -0.34 & 0.00 \\ 0.00 & 0.00 & -0.52 \end{pmatrix} \end{array} .$$

So the dominant Γ-eigenmode is not S^z, but S^z-like in the sense (numerical deviations in the second decimal have been discarded here)

$$\hat{V}^{\max} \propto v_{xz} S^z_{xz} + v_{yz} S^z_{yz} + v_{xy} S^z_{xy} \qquad v_{xz} = v_{yz} \approx 0.34 \quad v_{xy} \approx 0.52 \,,$$

while a pure S^z excitation would have a equal relative weights v_{xz}, v_{yz}, v_{xy}, $v_{xz}^2 + v_{yz}^2 + v_{xy}^2 = 0.5$. The observation that $V^{\max}$ is diagonal in orbital indices (which holds true throughout the whole Brillouin zone) is not trivial and the interpretation if this is not the case will be discussed in the next chapter.

Following the relative weights of the orbital contributions to the respective dominant eigenmode (figure 4.9) provides an understanding of the susceptibility peaks. First, the simple nesting condition [MS99] is residual in these plots, showing increased weight of the d_{xz} orbital (yellow) in vertical planes (perpendicular to the q_z-direction) crossing Q_i and increased weight of the d_{yz} orbital (cyan) in horizontal planes (perpendicular to the q_y-direction) also crossing Q_i. There are however strong alterations of the weight along these planes, undermining a pure nesting picture.

Also the d_{xy} orbital (magenta), the Fermi surface of which (the γ-sheet) does not fulfill a nesting condition holds the highest contribution to the susceptibility and does so also in regions where the magnitude

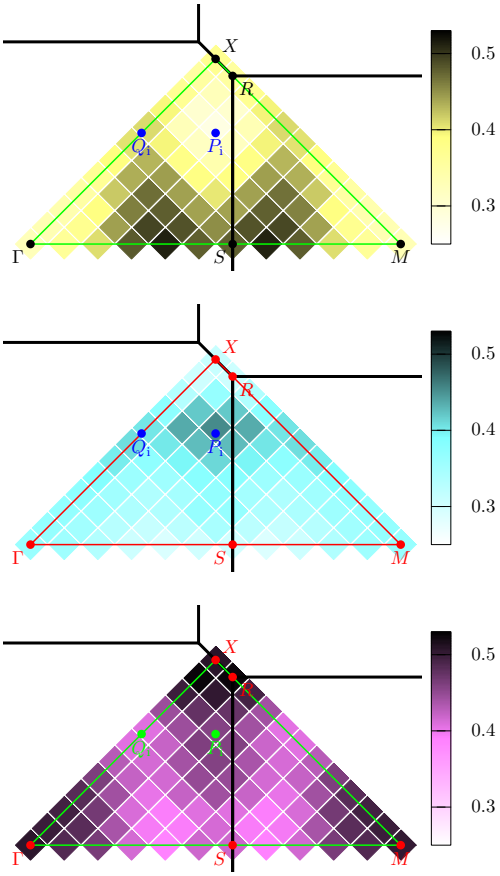

Figure 4.9: Orbital contribution of the d_{xz}-like (top, yellow), d_{yz}-like (middle, cyan) and d_{xy}-like (bottom, magenta) orbital to the dominant eigenmode of the susceptibility tensor. Parameters and notation as in figure 4.7

of the excitation (4.7) is still high, namely at the aforementioned point $\mathbf{q} = (0.15, 0.15)$ and (together with the d_{yz} orbital) at P_i.

Probably most important however is the observation that at the incommensurate point Q_i, all three orbitals contribute equally within numerical accuracy

$$V^{\max}(\mathbf{q} = Q_\mathrm{i}) = \begin{array}{c} \\ \uparrow \\ \\ \\ \downarrow \\ \\ \end{array} \begin{array}{c} \begin{array}{ccc} d_{xz} & d_{yz} & d_{xy} \end{array} \\ \begin{pmatrix} 0.41 & 0.00 & 0.00 \\ 0.00 & 0.41 & 0.00 \\ 0.00 & 0.00 & 0.40 \end{pmatrix} \\ \begin{array}{ccc} d_{xz} & d_{yz} & d_{xy} \end{array} \\ \begin{pmatrix} -0.41 & 0.00 & 0.00 \\ 0.00 & -0.41 & 0.00 \\ 0.00 & 0.00 & -0.41 \end{pmatrix} \end{array},$$

making this particular point a pure S^z-fluctuation without orbital discrimination. This too points against a pure nesting picture.

4.5 Outlook

This chapter developed numerical techniques to accurately determine dynamical lattice susceptibilities for multiorbital systems and demonstrated their use on the numerically challenging t_{2g} compound Sr_2RuO_4, reproducing experimental observations from inelastic neutron scattering experiments of an incommensurate peak in the magnetic susceptibility. The orbital contributions to the magnetic susceptibility are resolved throughout the Brillouin zone, revealing unexpected nontrivial behavior.

Still this investigation leaves room for future research. A more thorough comparison of the frequency dependence of the dynamical susceptibility is desirable. Fixed energy experimental data for low as well as reasonably high temperature is available for many paths

through the Brillouin zone [BSB$^+$02, IKK$^+$11], an systematic identification of experimental findings and the numerical work presented here will help the assessment of the approximation of a local irreducible vertex as an apt treatment of Sr_2RuO_4. This will be of particular interest for the shoulders of the incommensurate (Q_i-point) peak, at the P_i-point and at $\mathbf{q} = (0.15, 0.15)$, for which experimental and theoretical work is still debatable.

The orbital resolution can help to understand the source of the incommensurate peak, opening again the discussion as to how far it is connected in nature with the superconducting phase found at very low temperatures.

Five

Ordering tendencies on the square Hubbard bilayer

To gain further insight into the physical interpretation of the eigenbasis determined by the eigendecomposition of the susceptibility tensor $\underline{\underline{\chi}}$ (compare section 3.1), a fairly simple and well understood example will be investigated in this chapter with the developed set of tools.

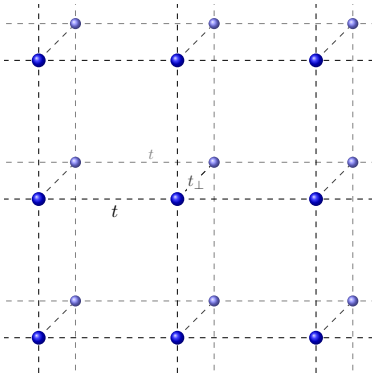

Figure 5.1: Hubbard bilayer with in-plane nearest neighbor hopping t and inter-plane hopping $t_\perp$

The square bilayer model (figure 5.1) consists of two square lattice planes of a conventional form, additionally allowing a hopping

in between the layers on-site. A plain Hubbard U-term is taken into account.

The hamiltonian is given by

$$\begin{aligned}\mathcal{H} = &- \sum_{\sigma\langle ij\rangle} t \left(c^\dagger_{\sigma 1 i} c_{\sigma 1 j} + c^\dagger_{\sigma 2 i} c_{\sigma 2 j} \right) \\ &- \sum_{\sigma i} t_\perp \left(c^\dagger_{\sigma 1 i} c_{\sigma 2 i} + c^\dagger_{\sigma 2 i} c_{\sigma 1 i} \right) \\ &+ \sum_i U \left(\hat{n}_{\uparrow 1 i} \hat{n}_{\downarrow 1 i} + \hat{n}_{\uparrow 2 i} \hat{n}_{\downarrow 2 i} \right)\end{aligned}$$

with $\langle ij \rangle$ denoting sums over nearest neighbors. The number in the index names the layer. With the choice $t = t_\perp = 0.25$, one can think of this model as two slabs cut out of a simple cubic lattice and this investigation will be restricted to the half-filled case. Consequently, the antiferromagnetic tendency from that model is also visible in this bilayer.

Phase diagrams of bilayer models have been discussed before [HKL09], showing a paramagnetic metal for small interaction parameter U and low $\frac{t_\perp}{t}$. With increasing U, it is well established that the bilayer undergoes a transition to an antiferromagnetic metal at low $\frac{t_\perp}{t}$ and a transition to a singlet state at larger $\frac{t_\perp}{t}$. For small $\frac{t_\perp}{t}$ and even further increased U, the system will eventually hit a antiferromagnetic insulating phase.

In this section, this model is investigated for illustrative purposes for the properties of the susceptibilities of a simple, yet multi-orbital system. The paramagnetic metal to antiferromanetic metal transition serves this purpose well. A more thorough investigation of also the other transitions in this model promises to be an interesting task, yet to be undertaken.

Lattice susceptibilities in a DMFT-like approximation are calculated along the lines of section 2.2 and chapter 3.

The right part of figure 5.2 shows the largest eigenvalue throughout the Brillouin zone (at $U = 0.9$), indicating that ordering tendencies

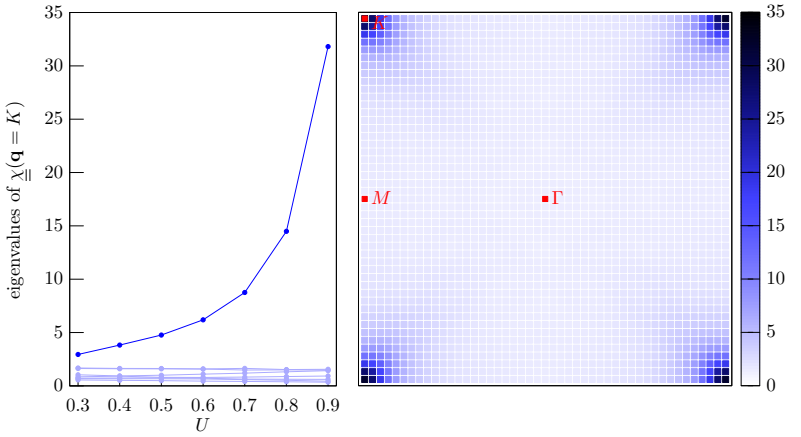

Figure 5.2: Left: All eigenvalues of the susceptibility tensor $\underline{\underline{\chi}}$ at the K-point for $T = 0.05$ and $U = 0.9$ and varying interaction strength. Right: Largest eigenvalue troughout the Brillouin zone

only appear in a K-point "anti"-pattern, while the left part shows the evolution of all eigenvalues at said K-point with a parameter, in this case the interaction strength, approaching the ordered phase.

This does not yet giving away the local state that will be continued alternatingly upon a divergence of this largest eigenvalue. For this, the eigenvector corresponding to the largest eigenvalue has to be considered

$$V^{(1)} = \begin{array}{c} \\ \uparrow \\ \downarrow \end{array} \begin{pmatrix} 0.5 & 0.0 \\ 0.0 & -0.5 \end{pmatrix} \begin{pmatrix} -0.5 & 0.0 \\ 0.0 & 0.5 \end{pmatrix} .$$

Thus the fluctuating eigenmode is

$$\hat{V}^{(1)} = 0.5(\hat{n}_{1\uparrow} - \hat{n}_{1\downarrow} - \hat{n}_{2\uparrow} + \hat{n}_{2\downarrow}) \propto S_1^z - S_2^z \, .$$

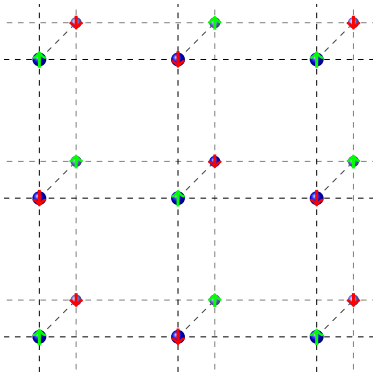

Figure 5.3: The antiferromagnetically coupled antiferromagnetic planes favoured in this model

The ordering pattern that realizes at the divergence of this eigenmode is visualized in figure 5.3

The ordering of this model in a DMFT-like approximation is settled with that and nicely reproduces the earlier results in an unbiased way. Additional insight however about the model and about the types of results the eigendecomposition of the susceptibility tensor can give, it is worthwhile to also consider the eigenvectors corresponding to the lower lying eigenvalues.

Table 5.1 and table 5.2 gather all those eigenvectors in the order they appear at $U = 0.9$. Besides the already discussed $V^{(1)}$, which is associated with a antiparallel spin ordering of the two sites per lattice site, some other states are easily identifiable. $V^{(3)}$ is a local parallel coupling, the ordered phase if the eigenvalue for this eigenvector would diverge would be a $S = 1$ antiferromagnet. This eigenvalue could be enhanced by introducing a Hund coupling to the hamiltonian. The contribution of $V^{(3)}$ to the susceptibility tensor is just the conventional spin susceptibility.

$$V^{(1)} = \begin{matrix}\uparrow \\ \downarrow\end{matrix}\begin{pmatrix} 0.5 & 0.0 \\ 0.0 & -0.5 \end{pmatrix}\begin{pmatrix} -0.5 & 0.0 \\ 0.0 & 0.5 \end{pmatrix}$$

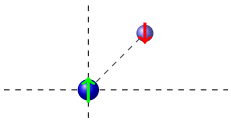

$$V^{(2)} = \begin{matrix}\uparrow \\ \downarrow\end{matrix}\begin{pmatrix} 0.0 & 0.5 \\ -0.5 & 0.0 \end{pmatrix}\begin{pmatrix} 0.0 & -0.5 \\ 0.5 & 0.0 \end{pmatrix}$$

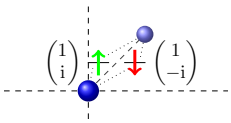

$$V^{(3)} = \begin{matrix}\uparrow \\ \downarrow\end{matrix}\begin{pmatrix} 0.5 & 0.0 \\ 0.0 & 0.5 \end{pmatrix}\begin{pmatrix} -0.5 & 0.0 \\ 0.0 & -0.5 \end{pmatrix}$$

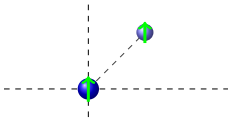

$\Rightarrow \chi^{\mathrm{m}}$

$$V^{(4)} = \begin{matrix}\uparrow \\ \downarrow\end{matrix}\begin{pmatrix} 0.0 & 0.5 \\ -0.5 & 0.0 \end{pmatrix}\begin{pmatrix} 0.0 & 0.5 \\ -0.5 & 0.5 \end{pmatrix}$$

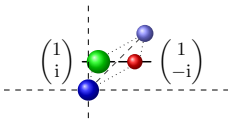

Table 5.1: The first four eigenvalues of the susceptibility tensor of the square nearest neighbor bilayer for $t = t_\perp = 0.25$, $U = 0.9$

$$V^{(5)} = \begin{matrix}\uparrow \\ \downarrow\end{matrix}\begin{pmatrix} 0.0 & 0.5 \\ 0.5 & 0.0 \\ 0.0 & 0.5 \\ 0.5 & 0.0 \end{pmatrix}$$

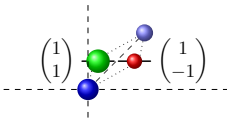

$$V^{(6)} = \begin{matrix}\uparrow \\ \downarrow\end{matrix}\begin{pmatrix} 0.0 & 0.5 \\ 0.5 & 0.0 \\ 0.0 & -0.5 \\ -0.5 & 0.0 \end{pmatrix}$$

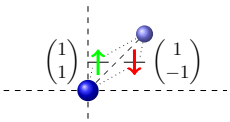

$$V^{(7)} = \begin{matrix}\uparrow \\ \downarrow\end{matrix}\begin{pmatrix} 0.5 & 0.0 \\ 0.0 & -0.5 \\ 0.5 & 0.0 \\ 0.0 & -0.5 \end{pmatrix}$$

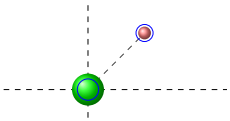

$\Rightarrow \chi^{\mathrm{o}}$

$$V^{(8)} = \begin{matrix}\uparrow \\ \downarrow\end{matrix}\begin{pmatrix} 0.5 & 0.0 \\ 0.0 & 0.5 \\ 0.5 & 0.0 \\ 0.0 & 0.5 \end{pmatrix}$$

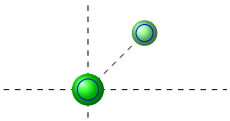

$\Rightarrow \chi^{\mathrm{c}}$

Table 5.2: The second part of table 5.1 with the fifth to eighth eigenvector

$V^{(7)}$ and $V^{(8)}$ are the density counterparts of the magnetic orders $V^{(1)}$ and $V^{(3)}$ respectively, with $\hat{V}^{(7)} \propto \hat{n}_1 - \hat{n}_2$ ($\hat{n}_a = \hat{n}_{\uparrow a} + \hat{n}_{\downarrow a}$) the orbital moment and its fluctuation resulting in what is conventionally called the orbital susceptibility χ^{o} and $\hat{v}^{(8)} \propto \hat{n}_1 + \hat{n}_2$ giving the charge susceptibility (χ^{c}) contribution. These two would increase in relevance with a nearest neighbor interaction term $\sum_{\langle ij \rangle} V \hat{n}_i \hat{n}_j$ in the hamiltonian, which favors charge ordering for sufficiently large V (see e.g. [HABW14]).

Slightly harder to grasp are the eigenmodes with off-diagonal components, $V^{(2)}$, $V^{(4)}$, $V^{(5)}$ and $V^{(6)}$, as they are not readily represented in the form $\sum_{\sigma a} v_{\sigma a} \hat{n}_{\sigma a}$, that encouraged an intuitive interpretation in the preceding chapter for the case of Sr_2RuO_4. Equation (3.1) provides a formal expansion of the susceptibility tensor in the fluctuating operators $\hat{V}^{(l)}$ irrespective of the one-particle basis in which they are represented. The other way around, the actual representation provides the one-particle basis in which the operator $\hat{V}^{(l)}$ takes the desired form.

Rewriting the operators $\hat{V}^{(l)}$ in equation (3.1)

$$\hat{V}^{(l)} = \sum_{\sigma i j} c^{\dagger}_{\sigma i} V^{(l)}_{\sigma i j} c_{\sigma j} = \underbrace{c^{\dagger}_{\sigma i} U^{(l)\star}_{i i'}}_{c^{(l)\dagger}_{i'}} \underbrace{U^{(l)}_{i' a} V^{(l)}_{\sigma a b} U^{(l)\star}_{b j'}}_{V'^{(l)}_{\sigma i' j'}} \underbrace{U^{(l)}_{j' j} c_{\sigma j}}_{c^{(l)}_{j'}}$$

with a unitary matrix $U^{(l)}$ allows a easy interpretation of the eigenmodes with off-diagonal components. When $U^{(l)}$ is chosen to be the eigenbasis of $V^{(l)}$ such that $V'^{(l)}$ becomes diagonal (with respect to the orbital indices i and j), the one-particle basis $c^{(l)\dagger}/c^{(l)}$ is the appropriate basis to express the eigenmode as occupation-like fluctuations. The respective orbital weights contributing to the fluctuation are given by the eigenvalues of $V^{(l)}$.

$V^{(6)}$ for example describes an antiparallel spin-alignment between the even and the odd superposition of the site-orbitals. For all cases ($V^{(2)}$, $V^{(4)}$, $V^{(5)}$ and $V^{(6)}$), table 5.1 and table 5.2 show the local ordering and give the appropriate eigenbasis.

While such a direct interpretation of the eigenbasis of the fluctuating mode will not always be possible for arbitrary systems, it is worth-

while to note that it is a general property of such, that off-diagonal components in the orbital indices of the fluctuating mode indicate a fluctuation of molecular orbital like mode.

Six

Lattice correlations and thermal properties of Na_xCoO_2

In 2008, Lang *et al.* [LBA+08] performed ^{23}Na T_1 relaxation and ^{23}K Knight shift NMR measurements to establish a "phase" diagram mapping the predominant correlation regimes throughout sodium content and temperature. The combination of these two measurements into the Korringa ratio, to which T_1 contributes information about the 'local' spin susceptibility at the position of the sodium core and ^{23}K captures the 'uniform' spin susceptibility, allowed to distinguish between the sodium-rich region, which features ferromagnetic correlations indicated by a Korringa ratio significantly smaller than zero and an well developed Curie tail in the uniform susceptibility and the sodium-poor region with a basically flat uniform susceptibility, yet a remarkably large Korringa ratio, reminiscent of a strong non uniform spin fluctuations, that were in total labeled as antiferromagnetic.

This came as a surprise, as previous studies, e.g. by Foo *et al.*, that only had access to the uniform susceptibility, had established no hallmark of strong correlation in the low-doping region, which itself has been subject to speculations [MK07], as the vicinity of the integer filling open d-shell $x = 0$ would have suggested otherwise.

In that context, Marianetti and Kotliar [MK07] introduced an effective three-band hamiltonian for the study of Na_xCoO_2 and showed that it is necessary to add an binary disorder potential mimicing the different sodium positions and averaging over the hybridizations

of the two distinct impurity types in a dynamical mean field theory [GKKR96] (DMFT) calculation in order to gain qualitative agreement of their impurity magnetic susceptibility with the experimental [FWW+04] uniform susceptibility.

In [BL12], which is reprinted in the following, the full wave-vector and frequency dependent susceptibility was calculated throughout the full Brillouin zone and for sodium doping contents ranging from $x = 0.3$ to $x = 0.9$. This allows a thorough comparison of the correlation regimes with the experimental findings of Lang *et al.* The general doping dependence and the cross-over between anti- and ferromagnetic correlations is well captured, including the temperature dependence of that cross-over. It is shown that the antiferromagnetic correlations are of K-point type for very low doping but shift to M around $x = 0.5$. In the case of the Korringa ratio, a quantity that has to be derived from the dynamical susceptibility, even the quantitative comparison holds.

Wilhelm *et al.* [WLH+14] confirmed the findings for the dynamical susceptibility and built on that to incorporate the coupling of quasiparticles to collective magnetic excitations employing the dual fermion method [RKL08, BHR+08] into the calculations to find traces of spin-polarons.

Encouraged by the success of the mean-field description in [BL12] that grounds the physical properties of Na_xCoO_2 on strong correlations effects in the Co-layer for all sodium contents instead of disorder effects of the sodium positions, it was a natural next step to review in a similar manner the high thermopower in this material, that was attributed to the interplay of disorder and correlations before [WTSH11]. To that end, in [BL14], which also is reprinted in the following, a three-orbital model is used incorporating the e'_g bands and a charge self-consistent [GPPL12, Gri13] (CSC) local density approximation (LDA)+DMFT scheme is used. Sodium content enters by considering a fractional charged pseudopotential in the LDA calculations [MELFed], i.e. in a effective way. Yet the single-particle spectra and the Seebeck coefficient follow with great agreement with

experiments.

Competing orders in Na_xCoO_2 from strong correlations on a two-particle level

Reprinted with permission from

L. Boehnke, and F. Lechermann
Physical Review B **85**, 075145 (2012).

The reference numbering used in this reprinted article is only valid within this specific article.

Competing orders in Na_xCoO_2 from strong correlations on a two-particle level

Lewin Boehnke and Frank Lechermann
I. Institut für Theoretische Physik, Universität Hamburg, D-20355 Hamburg, Germany
(Received 17 January 2011; published 28 March 2012)

Based on dynamical mean-field theory with a continuous-time quantum Monte Carlo impurity solver, static as well as dynamic spin and charge susceptibilites for the phase diagram of the sodium cobaltate system Na_xCoO_2 are discussed. The approach includes important vertex contributions to the **q** dependent two-particle response functions by means of a local approximation to the irreducible vertex function in the particle-hole channel. A single-band Hubbard model suffices to reveal several charge- and spin-instability tendencies in accordance with experiment, including the stabilization of an effective kagome sublattice close to $x = 0.67$, without invoking the doping-dependent Na-potential landscape. The in-plane antiferromagnetic-to-ferromagnetic crossover is additionally verified by means of the computed Korringa ratio. Moreover an intricate high-energy mode in the transverse spin susceptiblity is revealed, pointing toward a strong energy dependence of the effective intersite exchange.

DOI: 10.1103/PhysRevB.85.115128 PACS number(s): 71.27.+a, 71.10.Fd, 71.30.+h, 75.30.Cr

I. INTRODUCTION

The investigation of finite-temperature phase diagrams of realistic strongly correlated systems is a quite formidable task due to the often tight competition between various low-energy ordering instabilities. In this respect the quasi-two-dimensional (quasi-2D) sodium cobaltate system Na_xCoO_2 serves as a notably challenging case.[1,2] Here $x \in [0,1]$ nominally mediates between the $Co^{4+}(3d^5, S = \frac{1}{2})$ and $Co^{3+}(3d^6, S = 0)$ low-spin states. Thus the Na ions provide the electron doping for the nearly filled t_{2g} states of the triangular CoO_2 layers up to the band-insulating limit $x = 1$. Coulomb correlations with a Hubbard U up to 5 eV for the t_{2g} manifold of bandwidth $W \sim 1.5$ eV[3] are revealed from photoemission.[4] Hence with $U/W \gg 1$ the frustrated metallic system is definitely placed in the strongly correlated regime.

Various different electronic phases and regions for temperature T versus doping x are displayed in the experimental sodium cobaltate phase diagram (see Fig. 1), for instance, a superconducting dome ($T_c \sim 4.5$ K) stabilized by intercalation with water close to $x = 0.3$.[5] Pauli-like magnetic susceptibility is found in the range $x < 0.5$[1] with evidence for 2D antiferromagnetic (AFM) correlations.[2,6] For $x > 0.5$, spin fluctuations and increased magnetic response show up for $0.6 < x < 0.67$, including the evolution to Curie-Weiss (CW) behavior[1] for $0.6 < x < 0.75$ and the eventual onset of in-plane ferromagnetic (FM) order. The ordered magnetic structure in the doping range $0.75 < x < 0.9$ with $T_N \sim 19$–27 K[7–10] is of A-type AFM for the FM CoO_2 layers. As the local spin-density approximation (LSDA) is not sufficient to account for the AFM-to-FM crossover with x,[3] explicit many-body approaches are needed.[11–13]

Several theoretical works have dealt with the influence of the sodium arrangements on the electronic properties of Na_xCoO_2, both from the viewpoint of disordered sodium ions[12] as well as from orderings for certain dopings.[14–16] However, whether such sodium patterns are due to sole (effective) single-particle potentials or mainly originating from many-body effects within the CoO_2 planes is still a matter of debate.[17,18]

In this paper, we report the fact that a large part of the electronic (spin and charge) phase diagram of sodium cobaltate may be well described within a Hubbard model using realistic dispersions and without invoking the details of the sodium arrangement. Therefore most of the observed crossovers and instabilities are truly driven by strong correlation effects and can scarcely be described by a weak-coupling expansion around the noninteracting case. The theoretical study is elucidating the two-particle correlations in the particle-hole channel computed within dynamical mean-field theory (DMFT) including vertex contributions (for a review, see, e.g., Refs. 19 and 20). So far the latter have been neglected in cobaltate susceptibilities based on LSDA[21,22] and the fluctuation-exchange approximation.[22,23] Our dynamical lattice susceptibilities allow us to reveal details of the AFM-to-FM crossover with T and of the intriguing charge-ordering tendencies, both in line with recent experimental data.[2,24] Moreover, insight in the $(x, \mathbf{q})$ dependent spin excitations at finite frequency is provided.

II. MODELING AND METHOD

Since we are mainly interested in the $x > 0.5$ part of the phase diagram, the low-energy band dispersion of sodium cobaltate is described within an a_{1g}-like single-band approach, justified from photoemission[25] and Compton scattering[26] experiments. We primarily focus on the in-plane processes on the effective triangular Co lattice with tight-binding parameters up to the third-nearest-neighbor (NN) hopping, i.e., $(t, t', t'') = (-202, 35, 29)$ meV[27] for the 2D dispersion. Although intersite Coulomb interactions might play a role,[13] the canonical modeling was restricted to an on-site Coulomb interaction $U = 5$ eV. Our calculations show that already substantial nonlocal correlations originate therefrom. The resulting Hubbard model on the triangular lattice is solved within DMFT for the local one-particle Green's function $G(\tau_{12}) = -\langle T_\tau c(\tau_1) c^\dagger(\tau_2)\rangle$ with $\tau_{uv} = \tau_u - \tau_v$ and T_τ being the time-ordering operator. The DMFT problem is approached with the continuous-time quantum Monte Carlo methodology[28,29] in its hybridization-expansion flavor[29] as implemented in the TRIQS package.[30] Additionally we implemented the computation of the impurity two-particle Green's function[31] $G^{(2)}(\tau_{12}, \tau_{34}, \tau_{14}) = -\langle T_\tau c^\dagger(\tau_1) c(\tau_2) c^\dagger(\tau_3) c(\tau_4)\rangle$ to address explicit electron-electron correlations. In the approximation of a purely local particle-hole irreducible vertex,

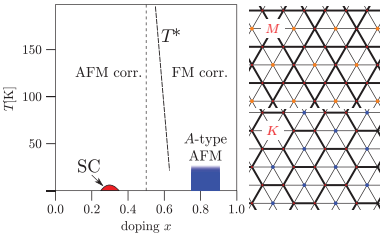

FIG. 1. (Color online) Left: Sketched Na_xCoO_2 diagram of dominating correlations and stable phases, based on Ref. 2. Right: M point ordering (top) and K point ordering (bottom) on the triangular lattice separating the lattice into a triangular sublattice (squares) and a kagome, honeycomb sublattice (thick lines).

$G^{(2)}$ allows us to also determine lattice susceptibilities.[19,20,31,32] These susceptibilities, e.g., for spin (s) and charge (c), written as

$$\chi_{s/c}(i\omega,\mathbf{q},T) = T^2 \sum_{\nu\nu'} \left(\tilde{\chi}^{(0)}_{s/c,\nu\nu'}(i\omega,\mathbf{q},T) + v_{s/c,\nu\nu'}(i\omega,\mathbf{q},T)\right), \tag{1}$$

where ω (ν) marks bosonic (fermionic) Matsubara frequencies, consist of two parts. Namely $\tilde{\chi}^{(0)}_{s/c,\nu\nu'}$ denotes the conventional (Lindhard-like) term, built up from the (renormalized) bubble part, which is mainly capable of detecting Fermi-surface-driven instabilities close to $T = 0$, but the second part $v_{s/c,\nu\nu'}$ (the vertex term) includes properly the energy dependence of the response behavior due to strong local interactions in real space. It proves important for revealing, e.g., magnetic instabilities at finite T due to the resolution of the two-particle correlations governed by an implicit intersite exchange J. Note that all numerics take advantage of the recently introduced orthogonal polynomial representation[31] of one- and two-particle Green's functions to provide the needed high accuracy and to eliminate artifacts often stemming from truncating the Fourier-transformed $G^{(2)}$ in Matsubara space.

Within the first Brillouin zone (BZ) of the triangular coordination with lattice constant a, the coherent Γ point instability signals FM order in the case of χ_s and phase separation for χ_c. Additionally important here are the instabilities at the K and M points. The associated orderings give rise to distinct sublattice structures in real space (cf. Fig. 1). The M point ordering leads to a triangular and a kagome sublattice with lattice constant $a_{\text{eff}} = 2a$, while the K point ordering establishes a triangular and a honeycomb sublattice with $a_{\text{eff}} = \sqrt{3}a$, respectively.

III. RESULTS

A. Static properties

We will first discuss the static $[\chi_{s/c}(\omega = 0,\mathbf{q},T)]$ response (read off from the zeroth bosonic Matsubara frequency), directly reflecting the system's susceptibility to an order of the ($\mathbf{q}$-resolved) type. The cobaltate intralayer charge susceptibility $\chi_c(0,\mathbf{q},T)$ shows pronounced features in $\mathbf{q}$ space with doping x (see Fig. 2). Close to $x = 0.3$ our single-band modeling leads to increased intensity inside the BZ, pointing toward longer-range charge-modulation (e.g., 3×3, etc.) tendencies in real space. That $Na_{1/3}CoO_2$ is indeed prone to such 120°-like instabilities has been experimentally suggested by Qian *et al.*[33] Toward $x = 0.5$ the susceptibility for short-range charge modulation grows in χ_c, displaying a diffuse high-intensity distribution at the BZ edge with a maximum at the K point for $x = 0.5$. No detailed conclusive result on the degree and type of charge ordering for the latter composition is known from experiments; however, chainlike charge disproportionation that breaks the triangular symmetry has been verified.[34,35] The present single-site approach cannot stabilize such symmetry breakings, but a pronounced χ_c at the K point at least inherits some stripelike separation of the two involved sublattices. Near $x = 0.67$, the χ_c maximum has shifted to the M point, in line with the detection of an effective kagome lattice from nuclear magnetic resonance (NMR) experiments.[24] For even higher doping, this $\mathbf{q}$ dependent structuring transmutes into a Γ point maximum, pointing toward known phase-separating tendencies.[36] Figure 2 also exhibits the x dependent intralayer spin susceptibility, starting with strong AFM peaks at $x = 0.3$ due to K point correlations. With reduced intensity these shift to the M point at $x = 0.5$, consistent with different types of spin and charge orderings at this doping level.[35] For $x > 0.5$, $\chi_s(\mathbf{q},T,0)$ first develops broad intensity over the full BZ before forming a pronounced peak at the Γ point above $x \sim 0.6$. Thus the experimentally observed crossover of the in-plane AFM-to-FM tendencies in the spin response is reproduced.

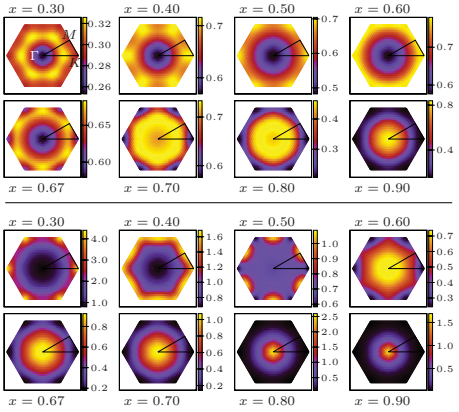

FIG. 2. (Color online) Static in-plane charge (top) and spin (bottom) susceptibility $\chi(0,\mathbf{q},T)$ with doping at $T = 386$ K.

Lang *et al.*[2] revealed from the Na NMR that this crossover is T dependent with x, resulting in an energy scale T^* below which AFM correlations are favored (cf. Fig. 1). The slope $\partial T^*/\partial x$ turns out negative, in line with the general argument that FM correlations are most often favored at elevated T because of the entropy gain via increased transverse

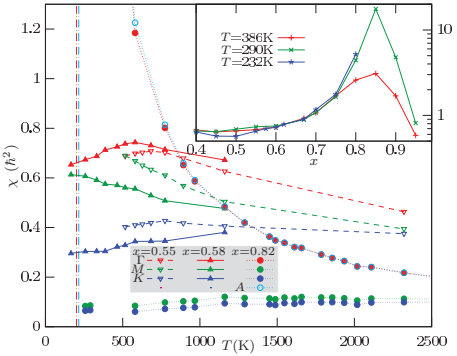

FIG. 3. (Color online) Temperature dependence of the spin susceptibility at the Γ, M, and K point for $x = 0.55$, 0.58, and 0.82. For the latter, values at the A point are also included. Vertical lines indicate extrapolated transition temperatures for Γ (FM) spin ordering and A (A-type AFM) spin ordering respectively for $x = 0.82$. The inset shows the doping dependence of the uniform ($\mathbf{q} = \Gamma$) in-plane spin susceptibility χ_s for various T. Note the largely increased magnitude of χ_s for $x \geqslant 0.75$ in this log-scale plot.

spin fluctuations. In this respect, Fig. 3 shows the $(x,T,\mathbf{q})$ dependence of the computed χ_s. For $x = 0.55$, 0.58, a maximum in the Γ point susceptibility is revealed, which has been interpreted by Lang *et al.*[2] as the criterion for a change in the correlation characteristics, thereby defining the T^* line. While the temperature scale exceeds the experimental value in the present mean-field formalism, the qualitatively correct doping behavior of the T^* line is obtained.

Beyond the experimental findings our calculations allow us to further investigate the nature of the magnetic crossover. Figure 3 reveals that at lower T and x closer to $x = 0.5$ the susceptibility at Γ is ousted by the one at M, while χ_s at K is mostly dispensable. The M susceptibility can be understood due to the proximity of the striped order at $x = 0.5$,[1,17,37] which is, however, not realized until much lower temperatures.

The inset of Fig. 3 follows the T dependent Γ point susceptibility through a vast doping range. Note the subtle resolution around $x = 0.5$ as well as the large exaggeration, especially for lower temperatures in the experimentally verified in-plane FM region. The main panel of Fig. 3 additionally shows for $x = 0.82$ the spin susceptibility at the A point [i.e., at $k_z = (0,0,\frac{1}{2})$ in the BZ), which denotes the A-type AFM order. While Γ and A show CW behavior, the extrapolated transition temperature is ∼7% higher at A than at Γ, verifying the experimental findings of A-type order.[7–10] In the temperature scan we additionally introduced a nearest-layer interplane hopping $t_\perp = 13$ meV;[9,13,38] however, the previous in-plane results are qualitatively not affected by this model extension. Due to known charge disproportionation the inclusion of long-range Coulomb interactions, e.g., via an intersite V,[13,16] seems reasonable. This was abandoned in the present single-site DMFT approach, resulting generally in reduced charge response. Without V, charge fluctuations are substantially suppressed for large U/W, while the intersite spin fluctuations are still strong due to superexchange.

B. Dynamical properties

Aside from the static response, our method allows access to the dynamic regime. Figure 4 shows the dynamical transverse spin susceptibility for fixed $T = 580$ K for selected x. Note the broad $\mathbf{q}$ dependence and small excitation energy in the low-doping regime. In contrast, the FM correlations near $x = 0.82$ are reflected by strong paramagnon-like gapless excitation at Γ combined with very little weight and rather high excitation energies at AFM wave vectors. Interestingly, a comparably strong and sharp K-type high-energy excitation (∼1 eV) for larger x below the onset of in-plane FM order is revealed. Its amplitude is strongest at $x = 0.67$ while its energy increases with x and it is worthwhile to note that the mode is *neither* visible when neglecting vertex contributions *nor* in a plain triangular Hubbard model with NN hopping only. Thus it reflects a strong energy dependence of the intersite exchange coupling $J = J(x,\mathbf{q},\omega)$ that obviously changes character for $x \sim 0.67$ with $\mathbf{q}$ and ω. The predicted high-energy feature could be probed experimentally and also studied in time-dependent measurements. We propose the use of modern laser-pulse techniques[39] to address this problem.

Experimentally, the evidence for significant $\mathbf{q} \neq 0$ fluctuations is drawn[2,40] from the Korringa ratio[41–44]

$$\mathcal{K}_x^T = \frac{\hbar}{4\pi k_B}\left(\frac{\gamma_e}{\gamma_N}\right)^2 \frac{1}{T_1 T K_S^2},$$
$$\frac{1}{T_1 T} = \lim_{\omega\to 0} \frac{2k_B}{\hbar^2} \sum_{\mathbf{q}} |A(\mathbf{q})|^2 \frac{\Im\chi_s^{-+}(\omega,\mathbf{q},T)}{\omega}, \qquad (2)$$
$$K_S = \frac{|A(\mathbf{0})|\gamma_e \Re\chi_s^{-+}(0,\mathbf{0},T)}{\gamma_N \hbar^2},$$

where $1/T_1$ is the nuclear relaxation rate, K_S is the NMR field shift, γ_e (γ_N) is the electronic (nuclear) gyromagnetic ratio, $A(\mathbf{q})$ is the hyperfine coupling, and k_B is the Boltzmann constant. $\Re\chi_s^{-+}$ and $\Im\chi_s^{-+}$ denote the real and imaginary parts of the transverse spin susceptibility, respectively. Roughly speaking, $\mathcal{K} > 1$ signals AFM correlations, $\mathcal{K} < 1$ points to FM tendencies in χ_s, and the term "Korringa behavior"

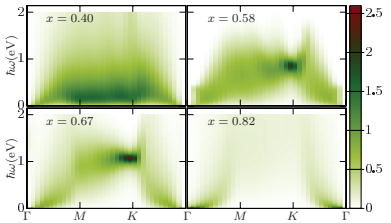

FIG. 4. (Color online) Imaginary part of the dynamical spin susceptibility for $T = 580$ K for selected dopings.

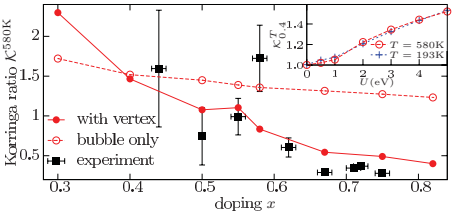

FIG. 5. (Color online) Korringa ratio versus doping for $T = 580$ K. The experimental data, extracted from Refs. 40 and 2, were obtained for lower temperatures. The inset shows the evolution of the bubble-diagram contribution from the analytically known value $\mathcal{K} = 1$ for the noninteracting ($U = 0$) case[41] to the fully interacting ($U = 5$ eV) calculation.

generally denotes the regime $\mathcal{K}(T) \sim 1$. In single-atom unit cells, $A(\mathbf{q})$ becomes $\mathbf{q}$ independent.

Note that $1/T_1$ especially is numerically expensive, as it requires calculation of χ_s^{-+} on many Matsubara frequencies with subsequent analytical continuation to the real frequency axis for contributions beyond the bubble diagram. Figure 5 finally shows the AFM-to-FM correlation crossover captured by the Korringa ratio over a wide doping range. The overall agreement with experimental results is conclusive. Relevant deviations in the low-doping regime probably originate from the smaller temperatures studied in the experiment. The difference at $x = 0.58$ might be of the same origin, but since charge ordering occurs for $x > 0.5$, which was not included explicitly here, neglecting the $\mathbf{q}$ dependence of $A(\mathbf{q})$ might be also questionable.[45] One can see that the bubble-only calculation yields a nearly flat Korringa ratio with doping and thus fails completely in explaining the experimental findings. In particular it does not reflect the strong FM correlations for high doping. This further proves the importance of strong correlations on the two-particle level, asking for substantial vertex contributions.[43] Note that the recently suggested lower-energy effective kagome model[16] including the effect of charge ordering is not contradicting the present modeling, since here the effective kagome lattice naturally shows up and also the key properties of the spin degrees of freedom seem well described on the original triangular lattice.

IV. CONCLUSION

In summary, the DMFT computation of two-particle observables including vertex contributions based on a realistic single-band Hubbard modeling for Na_xCoO_2 leads to a faithful phase-diagram examination at larger x, including the kagome-like charge-ordering tendency for $x \sim 0.67$ and the in-plane AFM-to-FM crossover associated with a temperature scale T^*. Thus it appears that many generic cobaltate features are already governed by a canonical correlated model, without invoking the details of the doping-dependent sodium-potential landscape or the inclusion of multiorbital processes. Of course, future work has to concentrate on quantifying further details of the various competing instabilities (and their mutual couplings) within extended model considerations. Beyond equilibrium physics, we predict a strong energy dependence of the effective intersite exchange resulting in an K-type high-energy mode around $x = 0.67$, which could be probed in experimental studies.

ACKNOWLEDGMENTS

The authors are indebted to O. Parcollet and M. Ferrero for useful discussions on the vertex implementation and calculation. We also thank A. Georges, H. Hafermann, A. I. Lichtenstein, O. Peil, and C. Piefke for valuable comments. This work was supported by the SPP 1386, the FOR 1346, and the SFB925 of the DFG. Computations were performed at the North-German Supercomputing Alliance (HLRN) and the regional computing center (RRZ) of the University of Hamburg.

[1] M. L. Foo, Y. Wang, S. Watauchi, H. W. Zandbergen, T. He, R. J. Cava, and N. P. Ong, Phys. Rev. Lett. **92**, 247001 (2004).
[2] G. Lang, J. Bobroff, H. Alloul, G. Collin, and N. Blanchard, Phys. Rev. B **78**, 155116 (2008).
[3] D. J. Singh, Phys. Rev. B **61**, 13397 (2000).
[4] M. Z. Hasan, Y.-D. Chuang, D. Qian, Y. W. Li, Y. Kong, A. P. Kuprin, A. V. Fedorov, R. Kimmerling, E. Rotenberg, K. Rossnagel, Z. Hussain, H. Koh, N. S. Rogado, M. L. Foo, and R. J. Cava, Phys. Rev. Lett. **92**, 246402 (2004).
[5] K. Takada, H. Sakurai, E. Takayama-Muromachi, F. Izumi, R. A. Dilanian, and T. Sasaki, Nature (London) **422**, 53 (2003).
[6] T. Fujimoto, G.-Q. Zheng, Y. Kitaoka, R. L. Meng, J. Cmaidalka, and C. W. Chu, Phys. Rev. Lett. **92**, 047004 (2004).
[7] J. Sugiyama, H. Itahara, J. H. Brewer, E. J. Ansaldo, T. Motohashi, M. Karppinen, and H. Yamauchi, Phys. Rev. B **67**, 214420 (2003).
[8] A. T. Boothroyd, R. Coldea, D. A. Tennant, D. Prabhakaran, L. M. Helme, and C. D. Frost, Phys. Rev. Lett. **92**, 197201 (2004).
[9] S. P. Bayrakci, I. Mirebeau, P. Bourges, Y. Sidis, M. Enderle, J. Mesot, D. P. Chen, C. T. Lin, and B. Keimer, Phys. Rev. Lett. **94**, 157205 (2005).
[10] P. Mendels, D. Bono, J. Bobroff, G. Collin, D. Colson, N. Blanchard, H. Alloul, I. Mukhamedshin, F. Bert, A. Amato, and A. D. Hillier, Phys. Rev. Lett. **94**, 136403 (2005).
[11] J. O. Haerter, M. R. Peterson, and B. S. Shastry, Phys. Rev. Lett. **97**, 226402 (2006).
[12] C. A. Marianetti and G. Kotliar, Phys. Rev. Lett. **98**, 176405 (2007).
[13] C. Piefke, L. Boehnke, A. Georges, and F. Lechermann, Phys. Rev. B **82**, 165118 (2010).
[14] J. Merino, R. H. McKenzie, and B. J. Powell, Phys. Rev. B **80**, 045116 (2009).
[15] S. Zhou and Z. Wang, Phys. Rev. Lett. **98**, 226402 (2007).
[16] O. E. Peil, A. Georges, and F. Lechermann, Phys. Rev. Lett. **107**, 236404 (2011).

[17]H. W. Zandbergen, M. L. Foo, Q. Xu, V. Kumar, and R. J. Cava, Phys. Rev. B **70**, 024101 (2004).
[18]Y. Hinuma, Y. S. Meng, and G. Ceder, Phys. Rev. B **77**, 224111 (2008).
[19]A. Georges, G. Kotliar, W. Krauth, and M. J. Rozenberg, Rev. Mod. Phys. **68**, 13 (1996).
[20]T. Maier, M. Jarrell, T. Pruschke, and M. H. Hettler, Rev. Mod. Phys. **77**, 1027 (2005).
[21]M. D. Johannes, I. I. Mazin, D. J. Singh, and D. A. Papaconstantopoulos, Phys. Rev. Lett. **93**, 097005 (2004).
[22]M. M. Korshunov, I. Eremin, A. Shorikov, V. I. Anisimov, M. Renner, and W. Brenig, Phys. Rev. B **75**, 094511 (2007).
[23]K. Kuroki, S. Onari, Y. Tanaka, R. Arita, and T. Nojima, Phys. Rev. B **73**, 184503 (2006).
[24]H. Alloul, I. R. Mukhamedishin, T. A. Platova, and A. V. Dooglav, Europhys. Lett. **85**, 47006 (2009).
[25]D. Qian, L. Wray, D. Hsieh, L. Viciu, R. J. Cava, J. L. Luo, D. Wu, N. L. Wang, and M. Z. Hasan, Phys. Rev. Lett. **97**, 186405 (2006).
[26]J. Laverock, S. B. Dugdale, J. A. Duffy, J. Wooldridge, G. Balakrishnan, M. R. Lees, G.-Q. Zheng, D. Chen, C. T. Lin, A. Andrejczuk, M. Itou, and Y. Sakurai, Phys. Rev. B **76**, 052509 (2007).
[27]H. Rosner, S.-L. Drechsler, G. Fuchs, A. Handstein, A. Wälte, and K.-H. Müller, Braz. J. Phys. **33**, 718 (2003).
[28]A. N. Rubtsov, V. V. Savkin, and A. I. Lichtenstein, Phys. Rev. B **72**, 035122 (2005).
[29]P. Werner, A. Comanac, L. de' Medici, M. Troyer, and A. J. Millis, Phys. Rev. Lett. **97**, 076405 (2006).
[30]M. Ferrero and O. Parcollet (unpublished).
[31]L. Boehnke, H. Hafermann, M. Ferrero, F. Lechermann, and O. Parcollet, Phys. Rev. B **84**, 075145 (2011).
[32]V. Zlatić and B. Horvatić, Solid State Commun. **75**, 263 (1990).
[33]D. Qian, D. Hsieh, L. Wray, Y.-D. Chuang, A. Fedorov, D. Wu, J. L. Lue, N. L. Wang, L. Viciu, R. J. Cava, and M. Z. Hasan, Phys. Rev. Lett. **96**, 216405 (2006).
[34]Q. Huang, M. L. Foo, J. W. Lynn, H. W. Zandbergen, G. Lawes, Y. Wang, B. H. Toby, A. P. Ramirez, N. P. Ong, and R. J. Cava, J. Phys.: Condens. Matter **16**, 5803 (2004).
[35]F. L. Ning, S. M. Golin, K. Ahilan, T. Imai, G. J. Shu, and F. C. Chou, Phys. Rev. Lett. **100**, 086405 (2008).
[36]M. Lee, L. Viciu, L. Li, Y. Wang, M. L. Foo, S. Watauchi, R. A. Pascal, R. J. Cava, and N. P. Ong, Nat. Mater. **5**, 537 (2006).
[37]G. Gašparović, R. A. Ott, J.-H. Cho, F. C. Chou, Y. Chu, J. W. Lynn, and Y. S. Lee, Phys. Rev. Lett. **96**, 046403 (2006).
[38]C. Fouassier, G. Matejka, J.-M. Reau, and P. Hagenmuller, J. Solid State Chem. **6**, 532 (1973).
[39]A. V. Kimel, C. D. Stanciu, P. A. Usachev, R. V. Pisarev, V. N. Gridnev, A. Kirilyuk, and T. Rasing, Phys. Rev. B **74**, 060403(R) (2006).
[40]H. Alloul, I. R. Mukhamedshin, G. Collin, and N. Blanchard, Europhys. Lett. **82**, 17002 (2008).
[41]J. Korringa, Physica (Amsterdam) **16**, 601 (1950).
[42]T. Moriya, J. Phys. Soc. Jpn. **18**, 516 (1963).
[43]E. Yusuf, B. J. Powell, and R. H. McKenzie, J. Phys.: Condens. Matter **21**, 195601 (2009).
[44]Note that we use a slightly different definition of χ_s than Ref. 43.
[45]A further reason could be an additional peak in the corresponding measurement at this precise doping,[2] which may or may not be of electronic nature, possibly influencing the Korringa ratio.

Getting back to Na_xCoO_2: Spectral and thermoelectric properties

Reprinted with permission from

L. Boehnke, and F. Lechermann
Physica Status Solidi A **211**, 1267 (2014).

The reference numbering used in this reprinted article is only valid within this specific article.

Phys. Status Solidi A **211**, No. 6, 1267–1272 (2014) / **DOI** 10.1002/pssa.201300197

physica status solidi a
www.pss-a.com
applications and materials science

Invited Article

Getting back to Na_xCoO_2: Spectral and thermoelectric properties

L. Boehnke and F. Lechermann*

Institut für Theoretische Physik, Universität Hamburg, Germany

Received 10 June 2013, revised 22 July 2013, accepted 4 March 2014
Published online 25 April 2014

Keywords density functional theory, dynamical mean-field theory, strong correlations, susceptibility, thermopower

* Corresponding author: e-mail frank.lechermann@physnet.uni-hamburg.de, Phone: +49 40 42838 7943, Fax: +49 40 42838 6798

Sodium cobaltate Na_xCoO_2 as dopable strongly correlated layered material with a triangular sublattice still poses a challenging problem in condensed matter. The intriguing interplay between lattice, charge, spin, and orbital degrees of freedom leads to a complex phase diagram bounded by a nominal Mott ($x=0$) regime and a band-insulating ($x=1$) phase. By means of the charge self-consistent density functional theory (DFT) plus dynamical mean-field theory (DMFT) scheme, built on a pseudopotential framework combined with a continuous-time quantum Monte-Carlo solver, we here study the one-particle spectral function $A(\mathbf{k}, \omega)$ as well as the thermopower $S(T)$. The computations may account for the suppression of the e'_g pockets in $A(\mathbf{k},\omega)$ at lower doping in line with photoemission experiments. Enhancement of the thermopower is verified within the present elaborate multi-orbital method to treat correlated materials. In addition, the two-particle dynamic spin susceptibility $\chi_s(\omega, \mathbf{q})$ is investigated based on a simplified tight-binding approach, yet by including vertex contributions in the DMFT linear response. Besides the identification of paramagnon branches at higher doping, a prominent high-energy antiferromagnetic mode close to $x=0.67$ is therewith identified in $\chi_s(\omega, \mathbf{q})$, which can be linked to extended hopping terms on the CoO_2 sublattice.

1 Introduction The quasi two-dimensional sodium cobaltate system Na_xCoO_2 marks one milestone in the investigation of realistic strongly correlated electron systems. It consists of stacked triangular CoO_2 layers, glued together by Na ions inbetween. Depending on the doping x, the nominal oxidation state of the cobalt ion lies between $Co^{4+}(3d^5)$ and $Co^{3+}(3d^6)$. While the $x=1$ compound is a band insulator with a filled low-spin $Co(t_{2g})$ subshell, for $x=0$ a single hole resides therein. Stimulated by findings of large thermoelectric response at higher doping x [1, 2] and superconductivity for $x\sim0.3$ upon intercalation with water [3], the phase diagram of Na_xCoO_2 attracted enormous interest, both experimentally as well as theoretically, in the pre-pnictide era of the early 2000 century. The relevance of strong correlation effects due to the partially filled Co($3d$) shell for $x<1$ has been motivated by several experiments, e.g. from optics [4], photoemission [5–8] and transport [9] measurements.

Although much progress has been made in the understanding of layered cobaltates, after more than 10 years of extensive research many problems are still open. We here want to address selected matters of debate, namely the nature of the low-energy electronic one-particle spectral function, the peculiarities of the dynamic spin response as well as the temperature- and doping-dependent behavior of the Seebeck coefficient.

2 Theoretical approach Effective single-particle methods based on the local density approximation (LDA) to density functional theory (DFT) are known to be insufficient to cover the rich physics of strongly correlated materials. Tailored model-Hamiltonian approaches to be treated within a powerful many-body technique such as dynamical mean-field theory (DMFT) are thus useful to reveal important insight in the dominant processes at high and low energy. Nowadays, the DFT + DMFT methodology (see, e.g. [10] for a review) opens the possibility to tackle electronic correlations with the benefit of the fully interlaced LDA materials chemistry.

In this work, a charge self-consistent DFT + DMFT scheme [11] built up on an efficient combination of a mixed-basis pseudopotential framework [12] with a hybridization-expansion continuous-time quantum Monte-Carlo solver [13–16] is utilized to retrieve spectral functions and the

thermopower. Thereby, the correlated subspace consists of the projected [17, 18] t_{2g} orbitals, i.e. a three-orbital many-body treatment is performed within the single-site DMFT part. The generic multi-orbital Coulomb interactions include density-density as well as spin-flip and pair-hopping terms, parametrized [19, 20] by a Hubbard $U = 5$ eV and a Hund's exchange $J = 0.7$ eV. Since the physics of sodium cobaltate is intrinsically doping dependent, we constructed Na pseudopotentials with fractional nuclear charge in order to cope therewith in DFT + DMFT. A simplistic structural approach was undertaken, utilizing a primitive hexagonal cell allowing for only one formula unit of Na_xCoO_2, with the fractional-charge Na in the so-called Na2 position. Thus, note that therefore the bilayer splitting does not occur in the electronic structure. Our calculations are straightforwardly extendable to more complex unit cells and geometries, however the present approach suits already the purpose of allowing for some general qualitative statements.

The resulting 3×3 DFT + DMFT Green's function in Bloch space with one correlated Co ion in the primitive cell hence reads here [11]

$$\mathbf{G}^{\mathrm{bl}}(\mathbf{k}, i\omega_n) = [(i\omega_n + \mu)\mathbf{1} - \varepsilon^{\mathrm{KS}}_{\mathbf{k}} - \mathbf{P}^{\dagger}(\mathbf{k}) \cdot \Delta\Sigma^{\mathrm{imp}}(i\omega_n) \cdot \mathbf{P}(\mathbf{k})]^{-1}, \quad (1)$$

where $\varepsilon^{\mathrm{KS}}_{\mathbf{k}}$ denotes the Kohn–Sham (KS) dispersion part, μ is the chemical potential and $\mathbf{P}(\mathbf{k})$ the t_{2g} projection matrix mediating between the Co correlated subspace and the crystal Bloch space. The impurity self-energy term $\Delta\Sigma^{\mathrm{imp}}$ includes the DMFT self-energy modified by the double-counting correction. For the latter the fully-localized form [21] has been utilized. To extract the one-particle spectral function $A(\mathbf{k}, \omega) = -\pi^{-1}\mathrm{Im}G^{\mathrm{bl}}(\mathbf{k}, \omega)$ as well as the thermopower, an analytical continuation of the impurity self-energy term $\Delta\Sigma^{\mathrm{imp}}$ in Matsubara space ω_n was performed via Padé approximation. Note that via the upfolding procedure within Eq. (1), the resulting real-frequency self-energy term in Bloch space carries k dependence, i.e. $\Delta\Sigma^{\mathrm{bl}} = \Delta\Sigma^{\mathrm{bl}}(\mathbf{k}, \omega)$.

For the investigation of the thermoelectric response, the Seebeck coefficient is calculated within the Kubo formalism from

$$S = -\frac{k_{\mathrm{B}} A_1}{|e| A_0}, \quad (2)$$

where the correlation functions A_n are given by

$$A_n = \sum_{\mathbf{k}} \int \mathrm{d}\omega \beta^n (\omega - \mu)^n \left(-\frac{\partial f_\mu}{\partial \omega}\right) \times \mathrm{Tr}[\mathbf{v}(\mathbf{k}) A(\mathbf{k}, \omega) \mathbf{v}(\mathbf{k}) A(\mathbf{k}, \omega)]. \quad (3)$$

Here, β is the inverse temperature, $\mathbf{v}(\mathbf{k})$ denotes the Fermi velocity calculated from the charge self-consistent KS part and f_μ marks the Fermi–Dirac distribution. Due to subtle refinements in the low-energy regime close to the Fermi level within the charge self-consistent DFT + DMFT scheme, computing A_n through Eq. (3) for the three-orbital system at hand is quite challenging. It requires great care both in the handling of the frequency dependence of the spectral function through the analytical continuation of the local self-energy term as well as the evaluation of the k sum. The difficulty with the latter is the sharp structure of the summand especially for low temperatures. Even a tetrahedron summation is problematic due to the double appearance of the spectral function in the sum [22]. We overcome this problem by using an adaptive numerical integration method separately for each A_n, where $\Delta\Sigma^{\mathrm{bl}}(\mathbf{k}, \omega)$, $\mathbf{v}(\mathbf{k})$ and $\varepsilon^{\mathrm{KS}}_{\mathbf{k}}$ are linearly interpolated in reciprocal space. Since all these quantities are relatively smooth in k, the resulting A_n show only weak dependence on the underlying mesh for these interpolations.

Finally, the expensive two-particle-based dynamic spin response with relevant local vertex corrections was studied. Thereby, a simplified single-band tight-binding parametrization [23] of the realistic dispersion, including hopping integrals up to third-nearest neighbor, entered the DMFT self-consistency cycle. For more details on the utilized DMFT + vertex technique see Refs. [16, 24].

3 One-particle spectral function The low-energy electronic states of Na_xCoO_2 close to the Fermi level ε_{F} have been subject to many discussions. LDA calculations for single-formula-unit cells reveal a threefold bandstructure of about 1.5 eV total bandwidth, dominantly originating from the Co $3d(t_{2g})$ states [25]. The resulting LDA Fermi surface (FS) consists of an a_{1g}-like hole sheet with additional e'_g-like hole pockets near the K-point of the hexagonal 1. Brillouin zone (BZ). For larger doping these hole pockets become more and more filled and their existence for $x \sim 0.6$ subtly depends on the very structural details [26]. Not only displays the measured spectral function $A(\mathbf{k},\omega)$ from angle-resolved photoemission (ARPES) experiments a much narrower dispersion very close to ε_{F}, but also the FS at lower doping lacks the hole-pocket sheets for any doping x [6, 27, 7, 8]. Usually, LDA works surprisingly well for the FS of strongly correlated metals, even if the method does not allow for the proper renormalization and the appearance of Hubbard sidebands. Hence, sodium cobaltate seems to belong to rare cases of correlated metals where the LDA FS topology does not agree with experiment.

Many attempts have been elaborated in order to either explain the non-existence of the hole pockets or to prove the ARPES data wrong. Without going into the very details of this rather long story, no definite final decision has been made on either line of argument. Concerning proper correlated methodologies, DFT + DMFT without charge self-consistency, i.e. in the traditional post-processing manner, may even *increase* the strength of the hole pockets (see, e.g. [28]). It appeared that the size of the $a_{1g} - e'_g$ crystal-field splitting plays an important role when turning on correlations [29, 28]. From an LDA + Gutzwiller study by Wan et al. [30] it became clear that charge self-consistency

may has a relevant influence on the correlated FS and the hole pockets indeed disappeared for $x > 0.3$ in their work.

In order to touch base with these results, we computed the one-particle spectral function $A(\mathbf{k},\omega)$ within charge self-consistent DFT + DMFT for $x = 0.3$ and $x = 0.7$. Thereby within our simplified structural treatment the apical oxygen position was chosen such to allow for a single-sheet a_{1g}-like hole FS within LDA at $x = 0.7$. Though the impact of charge order onto the spectral function is believed to be also important [31], we here neglect this influence and concentrate on the multi-orbital interplay and its impact on the correlated Fermi surface. Figure 1 shows the obtained three-orbital spectral functions close to the Fermi level. Note that there is also a lower Hubbard band, but due to the strong doping from half filling it is located in the energy range $[-6,-4]$ eV. As expected, the less-doped $x = 0.3$ case shows a stronger total renormalization of the t_{2g} derived manifold. The most important observation is the clear shift of the potential pocket-forming e'_g-like quasiparticle bands away from ε_F compared to the LDA result. This here amounts to a (nearly complete) vanishing of the pockets for $x = 0.3$, where they are still sizable in LDA. Even if there are some ambiguities concerning possible modifications due to structural details, the main trend that charge self-consistent DFT + DMFT (notably without invoking long-range order) tends to suppress the e'_g derived pockets is evident. Additionally the e'_g-like states exhibit a substantial broadening also with (nearly) total filling, a multi-orbital effect discussed already for filled t_{2g} states in $LaNiO_3$ [32]. This altogether brings the theoretical description in line with the available ARPES data. Thus, charge self-consistency can be an important ingredient in the calculations, accounting for shifts of the level structure in sensitive crystal-field environments.

4 Transport: Seebeck coefficient The increased thermoelectric response at larger doping x marks one of the Na_xCoO_2 key aspects [1, 2, 33, 34]. Although the more complex related so-called misfit cobaltates appear to display even larger thermopower and increased figure of merit (see, e.g. [35] for a recent review), the sodium cobaltate system still holds most of the main physics ready in its simplest structural form. There have been various theoretical modelings of the Seebeck coefficient for this system [36–42], ranging from the use of Heikes formula, Boltzmann equation approaches as well as Kubo formula oriented modelings. Albeit for a full account of thermoelectricity details may matter [41, 42], for the doping regime $0.6 < x < 0.75$ nearly all different theoretical descriptions yield thermopower values within the ranges of the experimental data. However open modeling questions remain for the highly increased Seebeck values in the regime of vary large doping $x > 0.8$ [34, 40] as well as for lower dopings $x \lesssim 0.5$, where, e.g. a nonmonotonic $S(T)$ with decreasing temperature is observed [33].

Here, we exhibit results for the thermopower as obtained within our charge self-consistent DFT + DMFT-based Kubo-formalism approach which builds up on the t_{2g} correlated subspace for Na_xCoO_2. Data is provided for $x = 0.7$ and $x = 0.75$ in Fig. 2, the other more challenging doping regimes concerning the thermoelectric response will be addressed in future studies. For instance, we expect that the low-lying e'_g bands leave some fingerprints in the thermopower for small x. Longer-ranged FM spin fluctuations and charge-ordering tendencies [31] may influence $S(T)$ for $x > 0.8$. Our in-plane Seebeck values are in good agreement with experimental data of Kaurav et al. [33]. The increased response for $x = 0.75$ compared to $x = 0.7$ is also verified, albeit the experimental tendency towards stronger enhancement with increased doping is still somewhat underestimated from theory. In addition to the in-plane values, Fig. 2 depicts the $S(T)$ tensor part along the c-axis of the system. Besides the n-like response with a change of sign, the absolute value becomes reduced at larger T, related to the different (rather incoherent) transport between layers at elevated temperature [5].

5 Two-particle function: dynamic spin susceptibility Besides the one-particle spectral properties and the thermopower, a further intriguing cobaltate issue is the magnetic behavior with doping. Within the frustrated triangular CoO_2 layers superexchange may dominate the

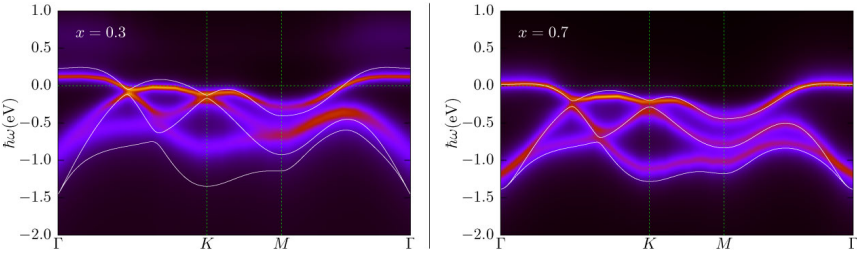

Figure 1 DFT + DMFT spectral function $A(\mathbf{k},\omega)$ for $x = 0.3$ (left) and $x = 0.7$ (right) at temperature $T = 290$ K. For comparison, the LDA band structure is drawn in white. The apical oxygen position was chosen such that an LDA single-sheet FS barely exists for $x = 0.7$.

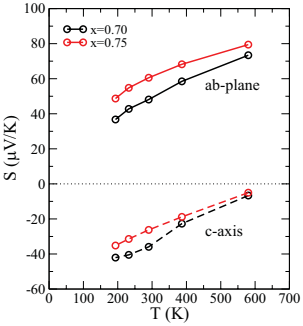

Figure 2 Seebeck coefficient $S(T)$ within charge self-consistent DFT + DMFT for larger doping. Full lines correspond to the in-plane thermopower, dashed lines to $S(T)$ along the c-axis.

low-doping regime due to nominal Mott proximity, but competing exchange processes set in at larger doping. The work by Lang et al. [43] based on nuclear-magnetic-resonance measurements nicely summarized the magnetic phase diagram of Na_xCoO_2 with temperature T, showing the inplane crossover from antiferromagnetic (AFM) to ferromagnetic (FM) correlations with the eventual onset of A-type AFM order for $x > 0.75$.

In line with the results for the spectral function we computed the spin susceptibility $\chi_s(\omega, \mathbf{q}, T)$ for an effective single-band model using DMFT with local vertex contributions [24]. This allows for the theoretical verification of the AFM-to-FM crossover. It can directly be retrieved from the shift of maxima in the static part $\chi_s(\omega = 0, \mathbf{q}, T)$ for $\mathbf{q}$ at the BZ K-point at small x towards maxima at $q = 0$ (Γ-point) at larger doping. Figure 3 displays the full dynamic spin susceptibility with increasing x in the paramagnetic regime. Below $x = 0.5$ the strong two-particle spectral intensity close to M and K at the BZ boundary is indeed visible. For rather large doping the intensity accumulates at small frequency ω near the Γ-point, with clear paramagnon branches due to the proximity towards in-plane FM order. We note that the vertex contributions are essential for the qualitative as well as quantitative signatures in the doping-dependent spin susceptibility [24].

Most interestingly, there also is a high-intensity mode near the K-point with maximum spectral weight well located around the commensurable doping $x = 0.67$ on the frustrated CoO_2 triangular lattice. The corresponding excitation energy of about 1 eV for $T = 580$K is decreasing with lowering the temperature. Thus, albeit the low-energy spin excitations for that larger doping have already shifted towards FM kind, a rather stable finite-ω AFM-like mode becomes available. This intriguing doping and frequency dependence of the effective exchange J can be linked to the specific hopping-integral structure of sodium cobaltate. In this respect, Fig. 4 shows the dynamic spin susceptibility at $x = 0.67$ for the Hubbard model on the triangular lattice with only nearest-neighbor hopping $-t$. While the FM paramagnon modes close to Γ seem even strengthened in that case, the high-energy feature close to K is now completely absent. It hence may be that the 1 eV scale for this excitation is linked to the energy difference between the correlated a_{1g} bonding-antibonding peaks (the upper one stemming from the higher hopping integrals). A Stoner-like spin-flip mechanism acting on the nonlocal doublet state at the commensurable $x = 0.67$ doping level [44] might be the second ingredient for the observed high-energy mode.

6 Summary We have presented a state-of-the-art DFT + DMFT investigation of the multi-orbital one-particle spectral properties as well as the thermoelectric behavior of Na_xCoO_2. The charge self-consistent scheme brings the one-particle spectral function concerning the correlated Fermi surface and the broadening of the occupied part in good

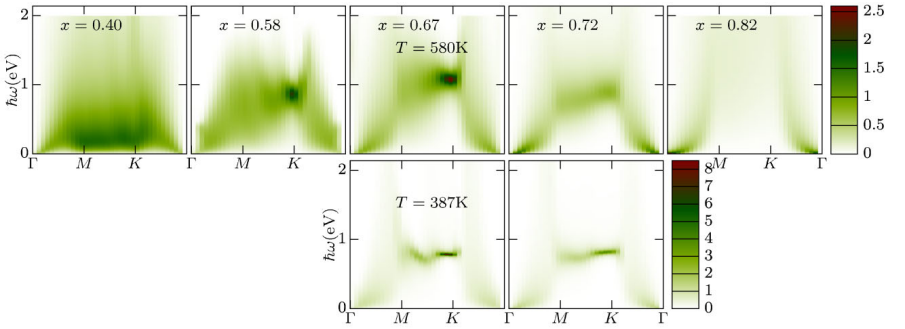

Figure 3 Doping-dependent dynamic spin susceptibility $\chi_s(\omega, \mathbf{q}, T)$. The lower row shows the results for reduced T for the same respective doping as directly above.

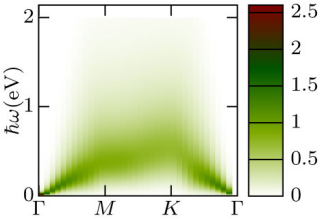

Figure 4 Dynamic spin susceptibility $\chi_s(\omega, \mathbf{q}, T = 580\,\mathrm{K})$ for only nearest-neighbor hopping $-t$ at $x = 0.67$.

agreement with available ARPES data. Further extensions of the realistic methodology towards the proper inclusion of charge-order effects, eventually with incorporating relevant intersite Coulomb terms, are still needed for a comprehensive understanding. Nonetheless the present framework is capable of addressing the temperature- and doping-dependent thermopower in line with experimental data for the larger doping regime. Detailed studies of the more critical regions in this respect at low and very high dopings are envisaged. Through the inclusion of sophisticated vertex contributions in a simplified tight-binding-based approach, details of the dynamic spin susceptibility, e.g. the prediction of a rather stable high-energy AFM-like mode close to $x = 0.67$, have been revealed. Additional experimental work is needed to verify our results and to stimulate future work. Eventually, the investigation of the direct impact of two-particle correlations on the one-particle spectrum is a challenging goal, but therefore it will be necessary to go beyond the local-correlation viewpoint of DMFT.

Acknowledgements We thank D. Grieger, A. I. Lichtenstein, and O. E. Peil for helpful discussions. Financial support from the DFG-SPP1386 and the DFG-FOR1346 is acknowledged. Computations were performed at the local computing center of the University of Hamburg as well as the North-German Supercomputing Alliance (HLRN) under the grant hhp00026.

References

[1] I. Terasaki, Y. Sasago, and K. Uchinokura, Phys. Rev. B **56**, R12685 (1997).
[2] T. Motohashi, E. Naujalis, R. Ueda, K. Isawa, M. Karppinen, and H. Yamauchi, Appl. Phys. Lett. **79**, 1480 (2001).
[3] K. Takada, H. Sakurai, E. Takayama-Muromachi, F. Izumi, R. A. Dilanian, and T. Sasaki, Nature (London) **422**, 53 (2003).
[4] N. L. Wang, P. Zheng, D. Wu, Y. C. Ma, T. Xiang, R. Y. Jin, and D. Mandrus, Phys. Rev. Lett. **93**, 237007 (2004).
[5] T. Valla, P. D. Johnson, Z. Yusof, B. Wells, Q. Li, S. M. Loureiro, R. J. Cava, M. Mikami, M. Y. Y. Mori, and T. Sasaki, Nature (London) **417**, 627 (2002).
[6] M. Z. Hasan, Y. D. Chuang, D. Qian, Y. W. Li, Y. Kong, A. Kuprin, A. V. Fedorov, R. Kimmerling, E. Rotenberg, K. Rossnagel, Z. Hussain, H. Koh, N. S. Rogado, M. L. Foo, and R. J. Cava, Phys. Rev. Lett. **92**, 246402 (2004).
[7] H. B. Yang, Z. Wang, and H. Ding, J. Phys. Condens. Matter **19**, 355004 (2007).
[8] J. Geck, S. V. Borisenko, H. Berger, H. Eschrig, J. Fink, M. Knupfer, K. Koepernik, A. Koitzsch, A. A. Kordyuk, V. B. Zabolotnyy, and B. Büchner, Phys. Rev. Lett. **99**, 046403 (2007).
[9] M. L. Foo, Y. Wang, S. Watauchi, H. W. Zandbergen, T. He, R. J. Cava, and N. P. Ong, Phys. Rev. Lett. **92**, 247001 (2004).
[10] G. Kotliar, S. Y. Savrasov, K. Haule, V. S. Oudovenko, O. Parcollet, and C. A. Marianetti, Rev. Mod. Phys. **78**, 865 (2006).
[11] D. Grieger, C. Piefke, O. E. Peil, and F. Lechermann, Phys. Rev. B **86**, 155121 (2012).
[12] B. Meyer, C. Elsässer, F. Lechermann, and M. Fähnle, FORTRAN 90, Program for Mixed- Basis-Pseudopotential Calculations for Crystals, Max-Planck-Institut für Metallforschung, Stuttgart, unpublished.
[13] A. N. Rubtsov, V. V. Savkin, and A. I. Lichtenstein, Phys. Rev. B **72**, 035122 (2005).
[14] P. Werner, A. Comanac, L. de' Medici, M. Troyer, and A. J. Millis, Phys. Rev. Lett. **97**, 076405 (2006).
[15] M. Ferrero and O. Parcollet, TRIQS: A Toolbox for Research in Interacting Quantum Systems.
[16] L. Boehnke, H. Hafermann, M. Ferrero, F. Lechermann, and O. Parcollet, Phys. Rev. B **84**, 075145 (2011).
[17] B. Amadon, F. Lechermann, A. Georges, F. Jollet, T. O. Wehling, and A. I. Lichtenstein, Phys. Rev. B **77**, 205112 (2008).
[18] V. I. Anisimov, D. E. Kondakov, A. V. Kozhevnikov, I. A. Nekrasov, Z. V. Pchelkina, J. W. Allen, S. K. Mo, H. D. Kim, P. Metcalf, S. Suga, A. Sekiyama, G. Keller, I. Leonov, X. Ren, and D. Vollhardt, Phys. Rev. B **71**, 125119 (2005).
[19] C. Castellani, C. R. Natoli, and J. Ranninger, Phys. Rev. B **18**, 4945 (1978).
[20] R. Frésard and G. Kotliar, Phys. Rev. B **56**, 12909 (1997).
[21] V. I. Anisimov, I. V. Solovyev, M. A. Korotin, M. T. Czyyk, and G. A. Sawatzky, Phys. Rev. B **48**, 16929 (1993).
[22] G. Palsson, Computational studies of thermoelectricity in strongly correlated electron systems, PhD thesis, New Brunswick, Rutgers, The State University of New Jersey (2001).
[23] H. Rosner, S. L. Drechsler, G. Fuchs, A. Handstein, A. Wälte, and K. H. Müller, Braz. J. Phys. **33**, 718 (2003).
[24] L. Boehnke and F. Lechermann, Phys. Rev. B **85**, 115128 (2012).
[25] D. Singh, Phys. Rev. B **61**, 13397 (2000).
[26] M. D. Johannes, D. A. Papaconstantopoulos, D. J. Singh, and M. J. Mehl, Europhys. Lett. **68**, 433 (2004).
[27] D. Qian, L. Wray, D. Hsieh, L. Viciu, R. J. Cava, J. L. Luo, D. Wu, N. L. Wang, and M. Z. Hasan, Phys. Rev. Lett. **97**, 186405 (2006).
[28] C. A. Marianetti, K. Haule, and O. Parcollet, Phys. Rev. Lett. **99**, 246404 (2007).
[29] F. Lechermann, S. Biermann, and A. Georges, Prog. Theor. Phys. Suppl. **160**, 233 (2005).
[30] G. T. Wang, X. Dai, and Z. Fang, Phys. Rev. Lett. **101**, 066403 (2008).
[31] O. E. Peil, A. Georges, and F. Lechermann, Phys. Rev. Lett. **107**, 236404 (2011).
[32] X. Deng, M. Ferrero, J. Mravlje, M. Aichhorn, and A. Georges, Phys. Rev. B **85**, 125137 (2012).
[33] N. Kaurav, K. K. Wu, Y. K. Kuo, G. J. Shu, and F. C. Chou, Phys. Rev. B **79**, 075105 (2009).

[34] M. Lee, L. Viciu, L. Li, Y. Wang, M. L. Foo, S. Watauchi, R. A. Pascal, R. J. Cava, and N. P. Ong, Nature Mater. **5**, 537 (2006).
[35] S. Hébert, W. Kobayashi, H. Muguerra, Y. Bréard, N. Raghavendra, F. Gascoin, E. Guilmeau, and A. Maignan, Phys. Status Solidi A **210**, 69 (2013).
[36] W. Koshibae and S. Maekawa, Phys. Rev. Lett. **87**, 236601 (2001).
[37] H. J. Xiang and D. J. Singh, Phys. Rev. B **76**, 195111 (2007).
[38] N. Hamada, T. Imai, and H. Funashima, J. Phys.: Condens. Matter **19**, 365221 (2007).
[39] K. Kuroki and R. Arita, J. Phys. Soc. Jpn. **76**, 083707 (2007).
[40] M. R. Peterson, B. S. Shastry, and J. O. Haerter, Phys. Rev. B **76**, 165118 (2007).
[41] P. Wissgott, A. Toschi, H. Usui, K. Kuroki, and K. Held, Phys. Rev. B **82**, 201106(R) (2010).
[42] G. Sangiovanni, P. Wissgott, F. Assaad, A. Toschi, and K. Held, Phys. Rev. B **86**, 035123 (2012).
[43] G. Lang, J. Bobroff, H. Alloul, G. Collin, and N. Blanchard, Phys. Rev. B **78**, 155116 (2008).
[44] C. Piefke, L. Boehnke, A. Georges, and F. Lechermann, Phys. Rev. B **82**, 165118 (2010).

Seven

Hidden spin-orbital hexagonal ordering induced by strong correlations in $LiVS_2$

$LiVS_2$ is numerically and conceptually by far the most demanding material that is dealt with in this work. The difficulty arises because several equally challenging aspects that can occur in the investigation of strongly correlated materials come together to mutually reinforce their respective complexity.

$LiVS_2$ features an intriguing ordered state that is based on an explicit participation of all three correlated orbital in the ${t_{2g}}^2$-shell. Experimentally, a $\sqrt{3} \times \sqrt{3}$-reconstruction of the quasi two-dimensional triangular layers in this material is observed [KUH$^+$09]. What however became clear only during this numerical investigation of the lattice susceptibilities is that this comes along with the formation of states intrinsically living on this reconstructed supercell, which voids a purely local (single-site) approximation for the determination of fluctuations even above the transition temperature. Yet, this investigation evaluates susceptibilities in this unordered phase to avoid a bias in the search for the divergent fluctuation. Ultimately, [BLKL14] uses the approach to deliberately break translational invariance of the two-particle Green's function and thus the susceptibility just slightly above the transition temperature while keeping the translational symmetry of the one-particle Green's function unbroken.

This leads a total of nine effective orbitals in the solution of the Bethe-Salpeter equation (BSE). At this point it is worthwhile to

cherish again the use of Legendre coefficients for the fermionic degrees of freedom in the handling of the two-particle quantities in the BSE. 30 Legendre coefficients were necessary for the representation of each fermionic degree of freedom for $T = 258$K, the temperature for which the supercell eigenmodes are shown in figure 5 and figure 6 of [BLKL14]. Thus, the matrices used in the inversion of the BSE even for the static case have a dimension of 4860×4860, which implies a memory-requirement of ≈ 360MB each, which makes this post-processing feasible on a ordinary desktop computer. Assuming a conservative guess of ≈ 300 Matsubara frequencies to gain a reasonable convergence (compare section 4.2), the required memory per matrix would reach ≈ 36GB.

A detailed account of the scientific goals of the investigation, the physical considerations and numerical calculations undertaken to reach those is given in the manuscript [BLKL14], which is reprinted in full in the following. Following that, a rough interpretation of the fluctuating eigenmode will be given in section 7.1, going a similar route as for the bilayer problem in chapter 5.

Hidden spin-orbital hexagonal ordering induced by strong correlations in $LiVS_2$

L. Boehnke, A. I. Lichtenstein, M. I. Katsnelson, and F. Lechermann
arXiv:1407.4795 [cond-mat.mtrl-sci] (2014).

The reference numbering used in this reprinted article is only valid within this specific article.

Hidden spin-orbital hexagonal ordering induced by strong correlations in $LiVS_2$

L. Boehnke,[1,*] A. I. Lichtenstein,[1] M. I. Katsnelson,[2] and F. Lechermann[1]

[1] *I. Institut für Theoretische Physik, Universität Hamburg, D-20355 Hamburg, Germany*
[2] *Institute for Molecules and Materials, Radboud University Nijmegen, NL-6525 AJ Nijmegen, The Netherlands*

The investigation of nature's various mechanisms to transform a given material from a metal to an insulator has been a salient research endeavor since the early area of quantum solid state physics. In seminal works, Slater and Mott developed two different routes for prominent driving forces in chemically ordered states that can result in an insulating phase. Either dominant exchange processes yield an magnetically ordered Slater insulator, or strong correlations localize electrons within a paramagnetic insulator of Mott type. In complex compounds with manifest multi-orbital character and apparent geometrical frustration the many-body physics underlying the competition between metallic and insulating state may be more intricate. Here we present a first-principles many-body analysis of multi-orbital lattice susceptibilities based on advanced correlated electronic structure methods to reveal a highly entangled spin-orbital hexagonal ordering (SOHO) originating in the metallic phase of the quasi-twodimensional compound $LiVS_2$ that eventually leads to an intriguing insulating phase at low temperature.

At low-enough temperature most solid-state systems enter a long-range ordered phase due to various instabilities. While the characterization of these ordered phases is in many cases obvious and an order parameter may be readily identified, for some materials a microscopic specification remains nebulous. Apart from the canonical magnetic, charge, orbital, structural and superconducting types of ordering more complicated phenomena have been discussed in certain materials. The famous 'hidden order' state in the heavy-fermion compound URu_2Si_2 [1–3] stands out as a prominent example thereof. As we will show, physics prevalent in the vanadium sulfide $LiVS_2$ can harbor hidden order with the need for a manifest multi-site description. This is due to the nature of interacting $3d$ electrons stemming from multi-orbital sites on a geometrically frustrated lattice. From model-Hamiltonian studies it is known that quantum $S = \frac{1}{2}$ spins on a frustrated lattice may give rise to many different stable phases, ranging from (anti)ferromagnets to (resonating) valence-bond solids [4]. Adding itinerancy and further orbital differentiation entangles charge, orbital, spin as well as lattice degrees of freedom in an intriguing way and allows for unusual metallicity with proximity to unconventional ordering modes.

The physics of the effective triangular-lattice compound $LiVS_2$ naturally addresses this sophisticated entanglement of different degrees of freedom. Within the $LiVX_2$, X=(O,S,Se) series the oxide is an insulator exhibiting an ordering transition at a critical temperature $T_c \sim 500$ K (compare Fig. 1). The selenide has metallic character throughout the studied temperature regime. Upon cooling only the sulfide displays a metal-insulator transition (MIT) at $T_{MIT} \sim 310$ K from a paramagnetic metal to an insulating state with vanishing uniform magnetic susceptibility [5, 6]. In the insulator a spin-peierls-like lattice distortion occurs [5], leading to a trimerization in the quasi-twodimensional arrangement of VS_6 octahedra. Orbital ordering has long been suggested to be a vital ingredient of the low-temperature phase in many layered vanadates [7] and experimental evidence appeared recently [8, 9]. Profound questions exist in view of the temperature depending electronic states and in general concerning the interplay of the various degrees of freedom in vicinity to the MIT in the case of $LiVS_2$. Namely the role of excitations and possible fingerprints of the ordered state within the metallic regime is of vital importance for the general understanding of metal-insulator transitions beyond the traditional Mott- and Slater-type scenarios. Moreover the VS_2-layer building block is also a object of interest in the context of novel time-dependent electronic structure studies [10].

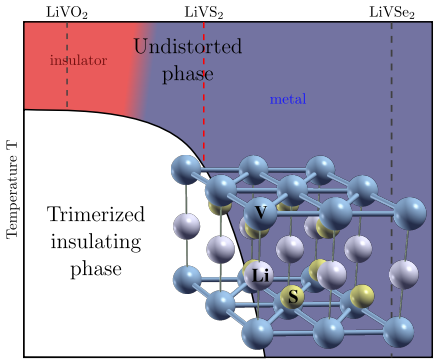

FIG. 1. Sketch of the generic $LiVX_2$, X=(O,S,Se) phase diagram (based on Ref. 5) with the $P\bar{3}m1$-$LiVS_2$ crystal structure in the metallic state as an inset.

It is important to realize that the MIT in $LiVS_2$ may not readily be understood from a weak-coupling nesting picture. At elevated temperatures large local V mo-

ments are revealed in the paramagnetic phase of $LiVO_2$ by x-ray-absorption spectroscopy [11]. After their finding of anomalous metallicity above the ordering transition, Katayama *et al.* [5] categorize the sulphur compound as a correlated paramagnetic metal at high T. Strong local Coulomb interactions within the nominal $3d^2$ valence of the V^{3+} ion are therefore a main driving force behind the materials' phenomenology. Previous model studies for these systems from the model many-body viewpoint were based on low-order perturbation arguments [7], on exact-diagonalization investigations [7, 11, 12] as well as on classical Monte-Carlo and Hartree-Fock examinations [13]. The first-principles electronic structure has also been addressed by density functional theory (DFT), and static strong-correlation aspects therein via the DFT+ Hubbard U methodology [12, 14]. For the intricate low-temperature trimerized phase of $LiVS_2$, the model approaches favored two possible orbitally-ordered spin-state candidates, that both account for the vanishing spin susceptibility. First, a trimer singlet state connecting to the experimentally revealed dominant high-spin $S = 1$ multiplet for the V ion in the metallic phase [7, 11]. Second, a trimer state with low-spin $S = 0$ for each V ion, i.e. violating Hund's rule [13]. Note that the latter proposition is different from a weak-coupling band-insulating state with unpolarized bonding orbitals.

In order to have a full account of the realistic quantum many-body problem, we go beyond the model perspective as well as static strong-correlation investigations. We show that by lowering the temperature T for $LiVS_2$ the optimal compromise between multi-orbital correlations driven by Hubbard U and Hund's J_H as well as the given hopping processes on the effective triangular lattice is provided by an even more challenging ordering beyond these suggestions. Namely, by means of advanced first-principles many-body theory a spin-orbital hexagonal ordering (SOHO) is identified to originate from the metallic high-symmetry phase. Therewith for multi-orbital frustrated lattice systems a conclusive connection is drawn between a local high-spin phase at elevated T and a global low-spin phase at low T.

LOCALIZED BASIS AND ONE-PARTICLE SPECTRUM

The $LiVS_2$ compound has the underlying $P\bar{3}m1$ space group (a=3.38 Å, c/a=1.82) [18] with an 1T-type ion-stacking along the c-axis. The sandwich VS_2 layer has ideal triangular symmetry. LDA calculations place the Fermi level ε_F within the isolated three-band manifold of dominant $3d(t_{2g})$ character and bandwidth $W \sim 2.1$ eV (see Fig. 2a). These bands host the two electrons of the low-spin V($3d^2$) filling. For this threefold a maximally-localized Wannier-function (WF) basis [19] may be derived with the low-energy WFs directed along the canonical directions towards neighboring vanadium ions (see Fig 2b). The nearest-neighbor (NN) hopping within this degenerate basis amounts to $t_{NN} = -290$ meV along the facing orbitals of the respective axes.

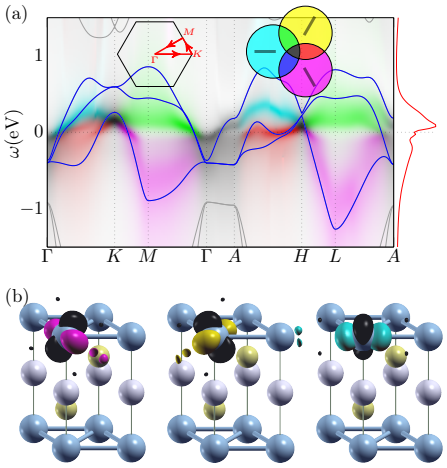

FIG. 2. (a) Low-energy interacting LDA+DMFT[15–17] spectral function of $LiVS_2$ slightly above the transition temperature with comparison to the LDA bands (full lines) shown along the path through the Brillouin zone noted in the left inset. The represented spectral weight differentiates between the three correlated-subspace contributions using an subtractive color scheme based on the color coding for the Wannier functions, which is shown in the right inset. (b) Low-energy degenerate t_{2g}-like Wannier functions (with specific color coding: magenta, yellow, cyan).

To include realistic electronic correlations beyond the static limit we continue the investigation in the state-of-the-art DFT + dynamical mean-field theory (DMFT) framework [15–17] by utilizing the derived WF basis as the correlated subspace. The resulting orbital-dependent strong electronic correlations significantly modify the LDA-derived electronic structure. Interestingly, since there are two electrons in three orbitals, $LiVS_2$ falls in the category of an Hund's metal where besides the Hubbard U the local interorbital (Hund's) exchange J_H has a dominant influence on the strong-correlation physics (see e.g. [20] for a recent review). Figure 2 displays band-narrowing, transfer of spectral weight as well as lifetime effects in the one-particle spectral function $A(\vec{k}, \omega)$ due to the rotational-invariant multi-orbital Coulomb interactions on each V site. Especially along ΓK and the corresponding AH direction at $k_z = 0.5$ in the Brillouin zone (BZ) the renormalization leads to intricate very low-

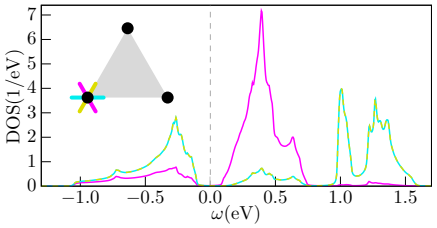

FIG. 3. Local t_{2g} LDA density of states of the insulating structurally distorted low-temperature compound. Local orbital ordering via the dominant occupation of the yellow and the cyan orbital (for the choice of the V site adumbrated in the inset) is observable.

energy susceptible many-body states close to $\varepsilon_{\rm F}$. Notably the electron pocket at Γ and the hole pocket at K get shifted towards the Fermi level. The WF-character contribution varies strongly in the inplane k directions and band-like coherency is quickly lost away from the Fermi level, specifically in the unoccupied higher-energy region.

It is evident that DFT+DMFT describes a strongly correlated metal at elevated temperatures. A large local magnetic moment on the V ions associated with $\langle S^2_{\rm loc}\rangle \sim 1.96$ is retrieved. As outlined, by lowering T an intriguing Mott scenario sets in that involves nearly all available system degrees of freedom. LDA calculations in the low-temperature $\sqrt{3}\times\sqrt{3}$ phase with the experimentally observed lattice distortion on the quasi-twodimensional triangular VS_2 lattice [6] indeed reveal an insulating state (see Fig. 3). This nonmagnetic band insulator in LDA displays a band gap of the order of 200 meV. On each V site of the isolated triangles, respectively, the t_{2g} orbitals pointing along the triangle edges are most strongly occupied. However this effective single-particle band-insulating solution is motivated from the sole observed symmetry reduction from the structural distortion. It cannot grasp the full truth, since e.g. the sophisticated fate of the high-T paramagnetic local spin degree of freedom close to and in the ordered phase is left unexplained from this simplistic viewpoint and thus fails to reveal the electronic mechanism behind the trimerization.

FROM TWO-PARTICLE SUSCEPTIBILITIES TO THE HIDDEN-ORDER PARAMETER

The remaining challenge to shed light on the $LiVS_2$ ordering relies in the combination of nonlocal physics, i.e. real-space order parametrization that involves correlations among different lattice sites, with manifest multi-orbital degrees of freedom. To tackle this we advance the DFT+DMFT approach by appending a two-particle-susceptibility formalism that includes generic multi-orbital vertex contributions. This allows to study quantum fluctuations leading to nonlocal ordering tendencies in the correlated metallic high-temperature regime above $T_{\rm MIT}$, in principle without breaking translational symmetry in real- or reciprocal space. Hence instead of addressing the broken-symmetry phase directly, we remain in the metallic state and examine multi-orbital two-particle response functions upon lowering the temperature. That approach is indeed adequate in the present context, since diffuse scattering hinting towards precursive manifestations of the ordered state has been noticed in the electron-diffraction pattern of metallic $LiVS_2$ [5].

In general, phase transitions are indicated by a divergence of the static susceptibility associated with the underlying ordering parameter and with a wave vector signaling the real-space pattern of the ordered phase. Beyond former single-band studies [21, 22], we here have access to the complete three-orbital particle-hole susceptibility tensor $\chi^{\sigma\sigma'}_{mm'm''m'''}(\vec{q},\omega)$ at finite temperature, with full generality concerning its frequency-dependent structure [23]. It allows an evaluation of all experimentally measurable susceptibilities and even explicit determination of dominant excitation modes.

In the case of models with a single correlated orbital per site, the longitudinal particle-hole channel allows for 2 susceptibilities, namely the ($\vec{q}$-dependent) spin- and charge response [23]. For a three-orbital t_{2g} shell however, there are 18 such independent possible susceptibilities and not much problem-tailored physical insight may be gained by monitoring each of those. A much more promising route to examine susceptibilities in multi-orbital materials is to focus in a first step on the eigenvalues/modes of the susceptibility tensor $\chi_{\alpha\beta}$ in the superindeces $\alpha = \{\sigma m m'\}$ and $\beta = \{\sigma' m'' m'''\}$ with $m, m' m'', m'''$=1,2,3 and $\sigma, \sigma' = \uparrow, \downarrow$. From such an analysis

$$\chi^{(l)}(\vec{q},\omega{=}0) = \left\langle \mathcal{T}_\tau \sum_\alpha \hat{v}^{(l)}_\alpha(\vec{q}) \sum_\beta \hat{v}^{\star(l)}_\beta(\vec{q}) \right\rangle \quad (1)$$

$$= \left\langle \mathcal{T}_\tau \hat{V}^{(l)}(\vec{q}) \hat{V}^{\star(l)}(\vec{q}) \right\rangle \quad (2)$$

is the lth eigenvalue and $\hat{V}^{(l)} = \sum_{\sigma m m'} v^{(l)}_{\sigma m m'} c^{\dagger\sigma}_m c^\sigma_{m'}$ is the corresponding eigenmode ($v^{(l)}_\alpha$ is the lth eigenvector of the susceptibility tensor $\chi_{\alpha\beta}$). This makes $V^{\rm max}$ the dominant fluctuating excitation upon approaching the phase transition and $\theta = \left\langle \hat{V}^{\rm max} \right\rangle$ a natural order parameter for the ordered phase. Here this eigenmode-assessment is elaborated for the realistic three-orbital manifold of $LiVS_2$.

Figure 4 shows the eigenvalue-evolution of $\chi^{\sigma\sigma'}_{mm'm''m'''}(K,\omega{=}0)$ with temperature. The K point

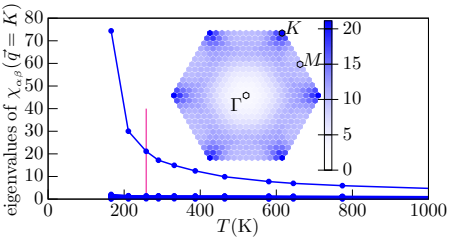

FIG. 4. Temperature dependence of all particle-hole-based susceptibility eigenvalues at the K point in the 1. Brillouin zone. The inset shows a contour plot of the largest eigenvalue throughout the Brillouin zone, emphasizing that relevant susceptibilities reside at the K point. The vertical line marks $T = 258$ K as the temperature used for the inset and for all other calculations throughout the work, if not stated otherwise.

being the position of the prominent maximum, as visible in the inset of Fig. 4. There a single eigenvalue diverges, indicating a phase transition at roughly $T_{\rm crit} \sim 150$ K, undershooting the experimentally observed transition temperature $T_{\rm MIT} \sim 310$ K. However this is expected [24], given the fact that our model neglects phonon contributions and thus does not allow for the lattice distortions that accompany the transition [5].

The eigenmode associated with the diverging eigenvalue $\chi^{\rm max}(K)$ can be identified as $\hat{V}^{(\rm max)}(K) \propto \hat{S}_z^{(\rm tot)}$. Thus the dominant multi-orbital K point instability towards $\sqrt{3}\times\sqrt{3}$ translational symmetry breaking of the frustrated triangular lattice has an intricate magnetic character. To reveal the details thereof one needs to go beyond the given susceptibility representation. The experimentally observed lattice reconstruction suggests a possible interatomic molecular-orbital like recombination within the triangular supercell, which is naturally not captured by studying the $\vec{q}$-dependence of single-site correlation functions. On the other hand, a thorough calculation of two-particle Green's functions for a full three-site triangular supercell with three orbitals per site is up to now infeasible.

Having uncovered the $\sqrt{3}\times\sqrt{3}$ ordering pattern, in a second step of our particle-hole susceptibility investigation we proceed to deliberately break translational symmetry of the lattice two-particle Green's function. Thereto we solve the supercell (SC) Bethe-Salpeter equation (BSE)

$$\widetilde{\chi}_{\rm SC}^{-1}(\vec{Q}{=}\Gamma) = \widetilde{\chi}_{\rm SC}^{(0)\,-1}(\vec{Q}{=}\Gamma) + \gamma_{\rm SC} \qquad (3)$$

on the $LiVS_2$ triangular lattice build from a minimal triangle three-site basis with superlattice wave vector $\vec{Q} = \Gamma$ (compare Fig. 6c). All quantities in eq. (3) carry the full inner fermionic degrees of freedom, with a Legendre representation replacing fermionic Matsubara frequencies [23] which renders this calculation both accurate and numerically feasible. The undistorted one-particle Green's function is used for the bare polarization $\widetilde{\chi}^{(0)}$ to take into account that our investigations still deal with temperatures *above* the transition to the disordered phase. The constructed irreducible supercell vertex function γ_c remains site-diagonal. That way we anticipate the translational symmetry breaking of the high-temperature susceptibility shown in Fig. 4.

Analysis of the 162 eigenmodes of the resulting supercell susceptibility tensor reveals two degenerate largest eigenvalues, being partners in a two-dimensional irreducible representation of the triangular building block. These eigenmodes are visualized in the right part of Fig. 5, for convenience rotated into the most prudent basis of the two-dimensional eigenspace, diagonalizing the 120° rotation, which results in a complex order parameter. Only one of the two eigenmodes is shown, its partner is its complex conjugated. Also, $v^{\rm max}_{\downarrow mm'} = -v^{\rm max}_{\uparrow mm'}$ as is typical for spin-like excitations. The interesting feature is the intricate orbital degree of freedom. The large diagonal parts with the $e^{i\frac{2}{3}\pi}$, i.e. 120°-degree, phase shift between lattice sites is reminiscent of a K-point excitation on a triangular lattice. The same pattern can be observed in models without orbital anisotropy. On the other hand, the appearance of relevant non site-diagonal elements reflects the building of a triangular supercell molecular orbital on the periodic supercell as sketched in Fig. 6a. A key feature of this ordering mode is the phase relation between the different onsite and intersite spin-orbital parts on the elementary triangle. As seen in Fig. 6a,b, the respective phases form a hexagon in the complex plane and hence the overall state may be accurately related to as 'spin-orbital hexagonal order (SOHO)'.

This traceless hidden-excitation mode does not imprint a finite magnetic moment to the supercell. Also applying a magnetic field to this robust system does not easily affect the total supercell spin arrangement. That renders our proposed order consistent with the observation of dramatic decrease of uniform magnetic susceptibility in the ordered phase [5] despite the large local magnetic moment in the disordered phase. In other words, the large vanadium local moment at elevated temperature becomes locked in a valence-bond-like fashion within the insulator, therefore not allowing for couplings to moderate applied magnetic fields.

It is important to explicitly break the translational symmetry within the BSE. An eigenmode analysis of a three-site supercell susceptibility obtained from a single-site BSE does not reveal the non-site-diagonal contributions.

As we concentrate on the structurally undistorted lattice, the observed fluctuating order maintains equal occupations of the orbitals. Orbital-symmetry breaking fol-

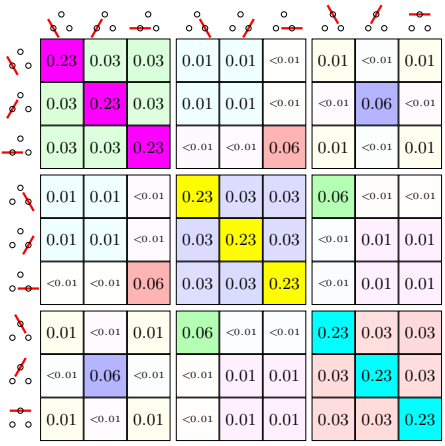

FIG. 5. Site-orbital resolved maximum eigenmode contributions. Only the ↑-part $v^{\max}_{\uparrow mm'}$ is shown with m and m' the adumbrated orbital indices on the supercell. Color codes the phase of the complex values according to Fig. 6b, saturation the absolute value. The ↓-part is obtained through $v^{\max}_{\downarrow mm'} = -v^{\max}_{\uparrow mm'}$.

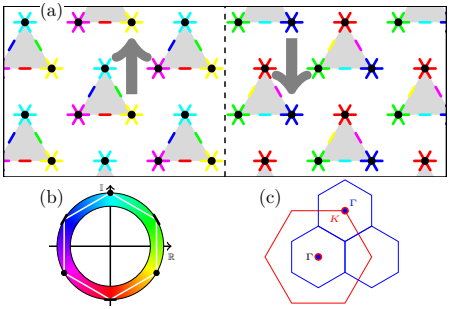

FIG. 6. Identified $LiVS_2$ order at low temperature. (a) Visualization of the maximum spin-orbital resolved eigenmode contribution $v^{\max}_{\sigma mm'}$ (compare Fig. 5) (left: $\sigma =\uparrow$, right: $\sigma =\downarrow$). (b) Colorcoding of the complex values used in Fig. 5 and in part a of this figure. Lines highlight the hexagonal phase relation between the major contributions to the order parameter. (c) Original lattice Brillouin zone (red) and superlattice Brillouin zone (blue). The original lattice K point coincides with the superlattices Γ point.

lows already on the LDA level (compare Fig. 3 and the corresponding discussion) as soon as the trimerization and the accompanying lattice distortion set in. The distinguished effective t_{2g} orbital which is weakly-occupied on each V atom in the insulating phase (e.g. the magenta orbital in Fig. 3) does not have relevant non site-diagonal elements (see Fig. 5). Thus it does not participate in the build-up of supercell molecular orbitals and we do not expect a relevant alteration from the fluctuating excitation to the realized broken translational-symmetry state.

After the characterization of the obtained complex ordering, we also want to touch base with the ordered-state propositions from previous works on the $LiVX_2$, (X=O,S) compounds. The present findings for the order parameter of the trimerization phase transition enables us to assess the overlap with other suggested ground states $|\psi\rangle$ by readily evaluating the ordering amplitude $\theta_{\text{trial}} = \left\langle\psi\middle|\hat{V}^{\max}\middle|\psi\right\rangle$. Specifically, the onsite low-spin scenario proposed by Yoshitake *et al.* [13] evaluates to zero, thus does not constitute a viable option. This is not surprising, because a key ingredient of our ordering mode is the intact local $S = 1$ vanadium spin. On the other hand, Pen *et al.* [11] proposed an onsite high-spin ordered state in the form of a product wave function of three local triplets on each equilateral triangle of V($3d^2$) ions. Indeed such a state yields a non-zero expectation value for the ordering amplitude θ_{trial}. But it does so solely based on the diagonal elements $v^{\max}_{\sigma mm}$ of the dominant fluctuating superlattice excitation, in line with the purely local picture. The relevant intersite terms are missing and thus that state serves only as an approximant to the true more complicate order. In the model picturing of [11] a strong Hund's J_{H} seems to overrule the nearest-neighbor intersite exchange J_{NN} (here not simply assumed to be in the Heisenberg-limit of the Hubbard model) in a complete fashion. Whereas our findings reveal a subtle interplay between local and nonlocal exchange processes that give rise to substantial interorbital intersite terms in the description of the ordered state.

CONCLUSIONS

The present work enriches the plethora of categories in the physics of metal-insulator transitions by revealing the challenging connection between the high-temperature metallic phase with large magnetic susceptibility and the low-temperature ordered phase with zero magnetic susceptibility in a frustrated multi-orbital compound subject to strong correlations. To this end, a powerful first-principles many-body analysis of multi-orbital lattice susceptibilities in the disordered state is introduced to investigate phase transitions in correlated materials. It complements existing approaches employed directly in the ordered phase and may be applied to further solid-state problems of strong correlations. For $LiVS_2$ a complex SOHO mode originating in the metal leads to a trimerized insulator with a unique electronic structure beyond

standard Mott-insulating mechanisms. The identified phase-sensitive $S_z^{(\mathrm{tot})} = 0$ ordered state generalizes the valence-bond concept of single-orbital $S = \frac{1}{2}$ systems to multi-orbital $S = 1$ problems on a frustrated lattice. Electron- or hole doping of that new state is believed to lead to fascinating metallicity with unique transport properties. Moreover investigating $LiVS_2$ under pressure or applying directional strain most likely results in emerging net-moment magnetism due to unlocking of spins on the equilateral base structure.

METHODS

The theoretical study builds up on crystal-structure data from experiment [18]. We employ the combination of density functional theory (DFT) with dynamical mean field theory (DMFT) (see [25] for a review)), i.e. the DFT+DMFT [15, 16] approach (see [17] for a review). The local density approximation (LDA) within a mixed-basis pseudopotential coding [26] is used to cope with the DFT part. Maximally-localized Wannier functions [19, 27] are employed to construct the low-energy Kohn-Sham Hamiltonian within the t_{2g}-like correlated subspace. Consequently the Kohn-Sham Hamiltonian given in the symmetry-adapted Wannier basis is tailored for the calculation as well as the interpretation of the physics. For the DMFT part an hybridization-expansion continuous-time (CT-Hyb) [28, 29] quantum Monte Carlo (QMC) impurity solver as implemented in the TRIQS package [30] is utilized. Therein advantage is taken of the orthogonal-polynomial representation for the one-particle and two-particle Green's functions [23]. A three-orbital Hubbard Hamiltonian in Slater-Kanamori parametrization with full rotational invariance is applied for the interactions in the correlated subspace. It reads [31]

$$\hat{H}_{\mathrm{int}} = (U - 3J_{\mathrm{H}})\frac{\hat{N}(\hat{N}-1)}{2} - 2J_{\mathrm{H}}\vec{S}^2 - \frac{J_{\mathrm{H}}}{2}\vec{L}^2 + \frac{5}{2}\hat{N} \quad (4)$$

with $\hat{N}$ is the total charge operator, $\vec{S}$ the spin- and $\vec{L}$ the angular momentum operators. We chose $U = 3.5$ eV and $J_{\mathrm{H}} = 0.7$ eV, appropriate for vanadium sulfides [32].

At DMFT self-consistency, also the full multi-orbital susceptibility tensor is evaluated in a DMFT-like approximation, e.g. assuming the locality of the two-particle particle-hole irreducible vertex in the Bethe-Salpeter equation (BSE) in this channel, as valid in the infinite-dimension limit [33]. This approximation has successfully been used for (effective) single-orbital problems [21, 22]. Note that already on the latter level the calculations are numerically extremely demanding. The inversion of the BSE requires the Monte-Carlo accumulation and the handling of the two-particle Green's function with its four orbital dependencies and full account of also the inner fermionic Matsubara frequencies. For the latter we employ the Legendre representation [23], as its better convergence helps tremendously in solving the superlattice BSE (eq. (3)).

In the BSE, the longitudinal and the transversal susceptibilities are decoupled, allowing a sole investigation of the longitudinal components (orbitally resolved $\hat{S}_z$ and $\hat{n}$-like excitations).

We thank H. Takagi for helpful discussions. The work benefits from financial support through the DFG-FOR1346 and the DFG-SFB925. Calculations were performed at the North-German Supercomputing Alliance (HLRN).

* lboehnke@physnet.uni-hamburg.de

[1] J. A. Mydosh and P. M. Oppeneer, Rev. Mod. Phys. **83**, 1301 (2011).
[2] P. Chandra, P. Coleman, and R. Flint, Nature **493**, 621 (2013).
[3] J. Mydosh and P. Oppeneer, Philosophical Magazine **0**, 1 (2014).
[4] H. T. Diep, *Frustrated Spin Systems* (World Scientific Publishing Company, 2005).
[5] N. Katayama, M. Uchida, D. Hashizume, S. Niitaka, J. Matsuno, D. Matsumura, Y. Nishihata, J. Mizuki, N. Takeshita, A. Gauzzi, M. Nohara, and H. Takagi, Phys. Rev. Lett. **103**, 146405 (2009).
[6] Y. Kawasaki, Y. Kishimoto, T. Tanaka, T. Ohno, S. Niitaka, N. Katayama, and H. Takagi, Journal of Physics: Conference Series **320**, 012028 (2011).
[7] H. F. Pen, J. van den Brink, D. I. Khomskii, and G. A. Sawatzky, Phys. Rev. Lett. **78**, 1323 (1997).
[8] T. M. McQueen, P. W. Stephens, Q. Huang, T. Klimczuk, F. Ronning, and R. J. Cava, Phys. Rev. Lett. **101**, 166402 (2008).
[9] T. Jin-no, Y. Shimizu, M. Itoh, S. Niitaka, and H. Takagi, Phys. Rev. B **87**, 075135 (2013).
[10] V. Brouet, J. Mauchain, E. Papalazarou, J. Faure, M. Marsi, P. H. Lin, A. Taleb-Ibrahimi, P. Le Fèvre, F. Bertran, L. Cario, E. Janod, B. Corraze, V. T. Phuoc, and L. Perfetti, Phys. Rev. B **87**, 041106 (2013).
[11] H. F. Pen, L. H. Tjeng, E. Pellegrin, F. M. F. de Groot, G. A. Sawatzky, M. A. van Veenendaal, and C. T. Chen, Phys. Rev. B **55**, 15500 (1997).
[12] Y. Guo, G. Zhang, X. Zhang, T. Jia, and Z. Zeng, Journal of Applied Physics **109**, 07E145 (2011).
[13] J. Yoshitake and Y. Motome, Journal of the Physical Society of Japan **80**, 073711 (2011).
[14] S. Y. Ezhov, V. I. Anisimov, H. F. Pen, D. I. Khomskii, and G. A. Sawatzky, EPL (Europhysics Letters) **44**, 491 (1998).
[15] V. I. Anisimov, A. I. Poteryaev, M. A. Korotin, A. O. Anokhin, and G. Kotliar, Journal of Physics: Condensed Matter **9**, 7359 (1997).
[16] A. I. Lichtenstein and M. I. Katsnelson, Phys. Rev. B **57**, 6884 (1998).
[17] G. Kotliar, S. Y. Savrasov, K. Haule, V. S. Oudovenko, O. Parcollet, and C. A. Marianetti, Rev. Mod. Phys. **78**, 865 (2006).

[18] B. van Laar and D. Ijdo, Journal of Solid State Chemistry **3**, 590 (1971).
[19] N. Marzari and D. Vanderbilt, Phys. Rev. B **56**, 12847 (1997).
[20] A. Georges, L. d. Medici, and J. Mravlje, Annual Review of Condensed Matter Physics **4**, 137 (2013), http://dx.doi.org/10.1146/annurev-conmatphys-020911-125045.
[21] T. Maier, M. Jarrell, T. Pruschke, and M. H. Hettler, Rev. Mod. Phys. **77**, 1027 (2005).
[22] L. Boehnke and F. Lechermann, Phys. Rev. B **85**, 115128 (2012).
[23] L. Boehnke, H. Hafermann, M. Ferrero, F. Lechermann, and O. Parcollet, Phys. Rev. B **84**, 075145 (2011).
[24] E. Pavarini, E. Koch, and A. I. Lichtenstein, Phys. Rev. Lett. **101**, 266405 (2008).
[25] A. Georges, G. Kotliar, W. Krauth, and M. J. Rozenberg, Rev. Mod. Phys. **68**, 13 (1996).
[26] B. Meyer, C. Elsässer, F. Lechermann, and M. Fähnle, "FORTAN 90 Program for Mixed-Basis-Pseudopotential Calculations for Crystals," Max-Planck-Institut für Metallforschung, Stuttgart.
[27] A. A. Mostofi, J. R. Yates, Y.-S. Lee, I. Souza, D. Vanderbilt, and N. Marzari, Computer Physics Communications **178**, 685 (2008).
[28] P. Werner, A. Comanac, L. de' Medici, M. Troyer, and A. J. Millis, Phys. Rev. Lett. **97**, 076405 (2006).
[29] E. Gull, A. J. Millis, A. I. Lichtenstein, A. N. Rubtsov, M. Troyer, and P. Werner, Rev. Mod. Phys. **83**, 349 (2011).
[30] M. Ferrero and O. Parcollet, "TRIQS: a Toolbox for Research in Interacting Quantum Systems," .
[31] L. de' Medici, J. Mravlje, and A. Georges, Phys. Rev. Lett. **107**, 256401 (2011).
[32] D. Grieger, L. Boehnke, and F. Lechermann, Journal of Physics: Condensed Matter **22**, 275601 (2010).
[33] V. Zlatic and B. Horvatic, Solid State Communications **75**, 263 (1990).

7.1 The fluctuation eigenbasis

[BLKL14] gives a representation of the fluctuation in terms of the t_{2g} states of the supercell sites (figure 5 of that publication). The structure of this has been discussed, most prominently the relevant offdiagonal components connecting facing orbitals between different sites of the supercell.

Going beyond the general remark that these components describe cluster-states as opposed to site-states (also compare chapter 5), this section will give a quantitative, yet approximate, evaluation of the eigenbasis of the dominant fluctuating mode.

To ease the interpretation of this eigenbasis, it is convenient to restrict the matrix in figure 5 of [BLKL14] to the diagonal elements and the six largest non-diagonal ones. This mainly discards site-diagonal orbital-offdiagonal elements (e.g. $\{\overset{\circ}{,}\overset{\circ}{,}\}$), which would obfuscate the relevant structure of eigenstates of the dominant fluctuating mode by introducing small admixtures of the different orbitals of the same site.

Leaving those aside, the task comes down to finding the eigenbases of the real part of the complex eigenmode

$$\Re S^{\max}_{mm'} = \Re(V^{\max}_{\uparrow mm'} - V^{\max}_{\downarrow mm'}) \tag{7.1}$$

$$= \begin{pmatrix} -0.40 & 0 & 0 & 0 & 0 & 0 & 0 & 0 & 0 \\ 0 & -0.40 & 0 & 0 & 0 & 0 & 0 & -0.10 & 0 \\ 0 & 0 & -0.40 & 0 & 0 & 0 & 0 & 0 & 0 \\ 0 & 0 & 0 & 0.40 & 0 & 0 & 0.10 & 0 & 0 \\ 0 & 0 & 0 & 0 & 0.40 & 0 & 0 & 0 & 0 \\ 0 & 0 & 0 & 0 & 0 & 0.40 & 0 & 0 & 0 \\ 0 & 0 & 0 & 0.10 & 0 & 0 & 0 & 0 & 0 \\ 0 & -0.10 & 0 & 0 & 0 & 0 & 0 & 0 & 0 \\ 0 & 0 & 0 & 0 & 0 & 0 & 0 & 0 & 0 \end{pmatrix}$$

and its imaginary part

$$\Im S^{\max}_{mm'} = \Im(V^{\max}_{\uparrow mm'} - V^{\max}_{\downarrow mm'}) \tag{7.2}$$

$$= \begin{pmatrix} -0.23 & 0 & 0 & 0 & 0 & 0 & 0 & 0 & 0 \\ 0 & -0.23 & 0 & 0 & 0 & 0 & 0 & 0.06 & 0 \\ 0 & 0 & -0.23 & 0 & 0 & -0.12 & 0 & 0 & 0 \\ 0 & 0 & 0 & -0.23 & 0 & 0 & 0.06 & 0 & 0 \\ 0 & 0 & 0 & 0 & -0.23 & 0 & 0 & 0 & 0 \\ 0 & 0 & -0.12 & 0 & 0 & -0.23 & 0 & 0 & 0 \\ 0 & 0 & 0 & 0.06 & 0 & 0 & 0.46 & 0 & 0 \\ 0 & 0.06 & 0 & 0 & 0 & 0 & 0 & 0.46 & 0 \\ 0 & 0 & 0 & 0 & 0 & 0 & 0 & 0 & 0.46 \end{pmatrix}$$

With the approximation to only include these elements, the eigenbases of $\Re S^{\max}_{mm'}$ and $\Im S^{\max}_{mm'}$ take the simple form that each eigenvector is a linear combination of at most two facing orbitals, e.g.

$$\cos(\alpha)\,\circ\,\circ + \sin(\alpha)\,\circ\,\circ$$

Instead of giving a table of the eigenvalues and vectors, it is more

Figure 7.1: The eigenbases of the real (left) and imaginary (right) part of the dominant fluctuation in $LiVS_2$

instructive to visualize them. This has been done in figure 7.1.

Each line in that figures represents one eigenvector, encoding all its information. The orientation of the line obviously identifies the

two facing orbitals, the position on the edge of the triangle encodes the phase of the superposition, going from $\alpha = 0$ if full relative weight is on one of the orbitals to $\alpha = \frac{\pi}{2}$ for the other.

If the constituents enter with equal sign, thus forming an even-like superposition, the line is shifted to the outside of the triangle, in the other case, for an odd-like superposition, the line is shifted to the inside of the triangle. Eigenvectors that are formed from just one site orbital are not shifted. Finally, the length of the line indicates the eigenvalue corresponding to the eigenvector, green for a positive eigenvalue, red for a negative one.

The 'outer' orbitals that do not have a facing neighbor within the supercell only ever appear isolated, a property that is also obvious from just inspecting equation (7.1) and equation (7.2) since they do not couple to other orbitals anymore in this approximation.

While merely illustrative due to its approximative nature, figure 7.1 helps to clarify the notion of the formation of cluster molecular orbital like states for the dominant order fluctuating mode. It becomes clear that while some states are still site-like, the order parameter carries inherently nonlocal contributions.

Figure 7.1 shows the eigenbasis of the real- and imaginary part of the complex eigenmode, therewith of two representatives of the manifold of easily excitable (and eventually self-exciting) states, hence figure 7.1 is basically showing the spin-imprint of the excitation, being periodically continued on the superlattice.

Whether one of these representatives or some other element of this manifold distinguishes itself to give an unambiguous ordered state upon divergence of the corresponding susceptibility, thus breaking apart the, or whether it persists and indeed the physics of the phase transition in $LiVS_2$ has an inherently complex valued order parameter when in more refined studies further effects like the supposedly important [KUH+09] electron-phonon coupling or the feedback of collective excitations on the quasi-particles is considered (e.g. using the dual fermion method [RKL08, TKH07]), is an interesting question, probably with impact way beyond this specific material, that should be

addressed in future work.

Eight

Conclusion

It is said that once you find the right language to talk about a phenomenon, you are almost guaranteed to find new physics [R.13].

The prime example is of course the incorporation of local temporal correlations within the dynamical mean field theory (DMFT), which proved to be the right language to talk about a wide class of effects based on strong correlation such as Mott physics.

The work presented in this thesis has contributed to the right language to talk about numerical aspects of the calculation of general lattice susceptibilities for strongly correlated models as well as their interpretation in context of experimental observables or inherent fluctuating modes.

The Legendre polynomial based basis has been developed and identified as the right language for the numerical treatment of those degrees of freedom of many-body Green's functions that do not themselves carry an immediate physical meaning. It was shown that for the one-particle Green's function and even more so for the two-particle Green's function, the unnecessary luxury to work in the analytically pleasant fermionic Matsubara frequency representation can be traded in for an numerically pleasant basis that greatly reduces systematic errors in the determination of physically meaningful observables and for two-particle quantities enables calculations in previously unreachable domains.

A decomposition of the orbital susceptibility tensor was introduced that highlights that while of course finding agreement with experimen-

tal observables in the investigation of strongly correlated realistically modeled materials is desirable, the right language to talk about dominant correlation regimes is not limited to that. Instead, it is possible to isolate the dominant fluctuating mode and directly base a physical interpretation on that quantity, possibly in terms of the eigenbasis of that mode.

Consequently, finding new physics is inevitable for the models and materials investigated here. For Sr_2RuO_4, the correlations are identified as purely spin-like, yet the orbital contributions contradict a plain nesting picture for the incommensurate peak in the spin susceptibility. Also, these orbital contributions at the other features in the Brillouin zone constitute interesting findings on their own, especially in direct comparison with the inelastic neutron scattering exeriments for this material.

While for Na_xCoO_2 the identification of the susceptibility eigenmodes trivially turns out as pure charge- and spin susceptibility, the richness of the phase diagram with doping more than makes up for that in terms of complexity. Using the susceptibility as the prime observable already is the right language in itself, given the experimental findings about the tuneability from anti- to ferromagnetic correlations with an non-trivial cross-over. That an unexpected high-energy mode in the dynamical spin susceptibility of yet not completely understood origin becomes visible in that data adds to the mystery but confirms that this is the right approach.

And finally, in $LiVS_2$ the right language to get insight about the nature of the ordered state upon cooling turns out to be to allow a correlation-level lattice reformation still in the undistorted phase, which allowed to identify the correlation eigenmode as an intrinsically non-local quantity.

Especially the last-mentioned material reached the limits of numerical feasibility, with its intriguing order fluctuations of three correlated orbitals at considerably low temperature and its inversion of an effective nine orbital Bethe-Salpeter equation. Hence, giving an outlook of prosperous further possible investigations will have to stay within this

realm until drastically higher computational resources are available.

Luckily, also this realm holds interesting physical challenges. For example, the story of the puzzling spin susceptibility in the $Sr_{n+1}Ru_nO_{3n+1}$ Ruddlesden-Popper series, of which only the $n = 1$ member was discussed in this thesis, is not yet fully told. Upon replacing strontium by calcium in this $n = 1$ member, eight more incommensurate peaks in the magnetic susceptibility appear [SFS+11], four each in q_x and q_y-direction, that seem related to the γ-sheet. Similar peaks have been observed in the $n = 2$ member [CFH+03], which in turn can be brought to exhibit an incommensurate peak on the diagonal path in the Brillouin zone by replacing a share of the ruthenium by titanium [SFP+09]. A thorough theoretical investigation that can not only map the spin susceptibility through the Brillouin zone but also attribute respective orbital contributions might shed some light on the mutual relations of effects in this materials system.

Finally, it will be a worthwhile task to apply the Legendre polynomial representation for the two-particle Green's function to dual fermion calculations, opening those to the same larger range of handleable materials including all of the above-mentioned. This will be interesting especially for Sr_2RuO_4, as it is unpredictable as of now, what surprises for the spectral function the coupling to the strong incommensurate collective spin excitation holds.

A

List of publications and author contributions

Publications discussed in this thesis

1. Orthogonal Polynomial Representation of Imaginary-Time Green's Functions
   L. Boehnke, H. Hafermann, M. Ferrero, F. Lechermann, O. Parcollet
   Physical Review B **84** 075145 (2011) (Editor's Suggestion)
   Reprinted on page 22

   This author participated in the development of the algorithms, implemented it, performed parts of the calculations and contributed to analysis and the preparation of the manuscript
   A part of this work was already discussed in this authors diploma thesis [Boe10]

2. Competing orders in Na_xCoO_2 from strong correlations on a two-particle level
   L. Boehnke, F. Lechermann
   Physical Review B **85** 115128 (2012)
   Reprinted on page 76

   This author performed the calculations and participated in the analysis and in the preparation of the manuscript

A part of this work was already discussed in this authors diploma thesis [Boe10]

3. Getting back to NaxCoO2: spectral and thermoelectric properties
   L. Boehnke and F. Lechermann
   Physica Status Solidi A **211**, 1267 (2014)
   Reprinted on page page 82

   This author participated in developing the algorithm, implemented it, participated in the analysis and in the preparation of the manuscript

4. Hidden spin-orbital hexagonal ordering induced by strong correlations in $LiVS_2$
   L. Boehnke, M. I. Katsnelson, A. I. Lichtenstein, F. Lechermann
   arXiv:1407.4795 [cond-mat.mtrl-sci] (2014)
   This manuscript is currently under consideration for publication
   Reprinted on page 92

   This author participated in developing the framework and the algorithms, implemented it, performed the calculations and participated in the analysis and in the preparation of the manuscript

Unrelated work

1. Electronic correlations in vanadium chalcogenides: BaVSe3 versus BaVS3
   D. Grieger, L. Boehnke and F. Lechermann
   Journal of Physics: Condensed Matter **22**, 275601 (2010).

2. Considerable non-local electronic correlations in strongly doped Na_xCoO_2

C. Piefke, L. Boehnke, A. Georges, F. Lechermann
Physical Review B **82** 165118 (2010).

3. Formation of orbital-selective electron states in LaTiO3/SrTiO3 superlattices
F. Lechermann, L. Boehnke and D. Grieger
Physical Review B **87**, 241101(R) (2013)

4. Electron correlation and magnetism at the LaAlO3/SrTiO3 interface: A DFT+DMFT investigation
F. Lechermann, L. Boehnke, D. Grieger and C. Piefke
Physical Review B **90**, 085125 (2014)

Bibliography

[AGD75] A. A. Abrikosov, L. P. Gor'kov, and I. E. Dzyaloshinski. *Methods of quantum field theory in statistical physics*. Courier Dover Publications, 1975.

[AIG+04] F. Aryasetiawan, M. Imada, A. Georges, G. Kotliar, S. Biermann, and A. I. Lichtenstein. Frequency-dependent local interactions and low-energy effective models from electronic structure calculations. *Physical Review B*, 70(19):195104, 2004.

[ALBvLM14] L.-F Arsenault, A. Lopez-Bezanilla, O. A. von Lilienfeld, and A. J. Millis. Machine learning for many-body physics: The case of the Anderson impurity model. *Physical Review B*, 90(15):155136, Oct 2014.

[APK+97] V. I. Anisimov, A. I. Poteryaev, M. A. Korotin, A. O. Anokhin, and G Kotliar. First-principles calculations of the electronic structure and spectra of strongly correlated systems: dynamical mean-field theory. *Journal of Physics: Condensed Matter*, 9(35):7359, 1997.

[AS10] A. Altland and B. D. Simons. *Condensed matter field theory*. Cambridge University Press, 2010.

[BGJV14] S. Backes, D. Guterding, H. O. Jeschke, and R. Valentí. Electronic structure and de Haas–van Alphen frequen-

cies in KFe_2As_2 within LDA+DMFT. *New Journal of Physics*, 16(8):083025, 2014.

[BHF+11] L. Boehnke, H. Hafermann, M. Ferrero, F. Lechermann, and O. Parcollet. Orthogonal polynomial representation of imaginary-time green's functions. *Physical Review B*, 84(7):075145, 2011.

[BHR+08] S. Brener, H. Hafermann, A. N. Rubtsov, M. I. Katsnelson, and A. I. Lichtenstein. Dual fermion approach to susceptibility of correlated lattice fermions. *Physical Review B*, 77(19):195105, 2008.

[BL12] L. Boehnke and F. Lechermann. Competing orders in Na_xCoO_2 from strong correlations on a two-particle level. *Physical Review B*, 85(11):115128, 2012.

[BL14] L. Boehnke and F. Lechermann. Getting back to Na_xCoO_2: Spectral and thermoelectric properties. *Physica Status Solidi A*, 211(6):1267, 2014.

[BL15] M. Behrmann and F. Lechermann. Large-amplitude spin oscillations triggered by nonequilibrium strongly correlated t_{2g} electrons. *Physical Review B*, 91(7):075110, Feb 2015.

[BLKL14] L. Boehnke, A. I. Lichtenstein, M. I. Katsnelson, and F. Lechermann. Hidden spin-orbital hexagonal ordering induced by strong correlations in $LiVS_2$. *arXiv preprint arXiv:1407.4795*, 2014.

[Boe10] L. Boehnke. Generalised susceptibilities in CTQMC, 2010. Diploma Thesis, Universität Hamburg.

[BSB+02] M. Braden, Y. Sidis, P. Bourges, P. Pfeuty, J. Kulda, Z. Mao, and Y. Maeno. Inelastic neutron scattering

study of magnetic excitations in Sr_2RuO_4. *Physical Review B*, 66(6):064522, 2002.

[BSS+04] M. Braden, P. Steffens, Y. Sidis, J. Kulda, P. Bourges, S. M. Hayden, N. Kikugawa, and Y. Maeno. Anisotropy of the incommensurate fluctuations in Sr_2RuO_4: A study with polarized neutrons. *Physical Review Letters*, 92(9):097402, 2004.

[CFH+03] L. Capogna, E. M. Forgan, S. M. Hayden, A. Wildes, J. A. Duffy, A. P. Mackenzie, R. S. Perry, S. Ikeda, Y. Maeno, and S. P. Brown. Observation of two-dimensional spin fluctuations in the bilayer ruthenate $Sr_3Ru_2O_7$ by inelastic neutron scattering. *Physical Review B*, 67(1):012504, 2003.

[DFM+12] X. Deng, M. Ferrero, J. Mravlje, M. Aichhorn, and A. Georges. Hallmark of strong electronic correlations in $LaNiO_3$: photoemission kink and broadening of fully occupied bands. *Physical Review B*, 85(12):125137, 2012.

[dMG11] L. de'Medici, J. Mravlje, and A. Georges. Janus-faced influence of Hund's rule coupling in strongly correlated materials. *Physical Review Letters*, 107(25):256401, 2011.

[FGKP13] A. Flesch, E. Gorelov, E. Koch, and E. Pavarini. Multiplet effects in orbital and spin ordering phenomena: A hybridization-expansion quantum impurity solver study. *Physical Review B*, 87(19):195141, 2013.

[FP] M. Ferrero and O. Parcollet. TRIQS: a Toolbox for Research in Interacting Quantum Systems.

[FWW+04] M. L. Foo, Y. Wang, S. Watauchi, H. W. Zandbergen, T. He, R. J. Cava, and N. P. Ong. Charge ordering, commensurability, and metallicity in the phase

diagram of the layered Na_xCoO_2. *Physical Review Letters*, 92(24):247001, 2004.

[GAC14] G. Giovannetti, M. Aichhorn, and M. Capone. Cooperative effects of Jahn-Teller distortion, magnetism, and Hund's coupling in the insulating phase of $BaCrO_3$. *Physical Review B*, 90(24):245134, Dec 2014.

[GK92] A. Georges and G. Kotliar. Hubbard model in infinite dimensions. *Physical Review B*, 45(12):6479, 1992.

[GKKR96] A. Georges, G. Kotliar, W. Krauth, and M. J. Rozenberg. Dynamical mean-field theory of strongly correlated fermion systems and the limit of infinite dimensions. *Reviews of Modern Physics*, 68(1):13, 1996.

[GML+11] E. Gull, A. J. Millis, A. I. Lichtenstein, A. N. Rubtsov, M. Troyer, and P. Werner. Continuous-time Monte Carlo methods for quantum impurity models. *Reviews of Modern Physics*, 83(2):349, 2011.

[GPPL12] D. Grieger, C. Piefke, O. E. Peil, and F. Lechermann. Approaching finite-temperature phase diagrams of strongly correlated materials: A case study for V_2O_3. *Physical Review B*, 86(15):155121, 2012.

[Gri13] D. Grieger. *Charge self-consistency in an LDA+DMFT framework*. PhD thesis, Hamburg, Universitaät Hamburg, 2013, 2013.

[HA13] L. Huang and B. Ao. Non-Fermi-liquid behavior in cubic phase $BaRuO_3$: A dynamical mean-field study. *Physical Review B*, 87(16):165139, 2013.

[HABW14] L. Huang, T. Ayral, S. Biermann, and P. Werner. Extended dynamical mean-field study of the Hubbard

model with long-range interactions. *Physical Review B*, 90(19):195114, Nov 2014.

[HAH08] S. Hochkeppel, F. F. Assaad, and W. Hanke. Dynamical-quantum-cluster approach to two-particle correlation functions in the Hubbard model. *Physical Review B*, 77(20):205103, 2008.

[Hau07] K. Haule. Quantum Monte Carlo impurity solver for cluster dynamical mean-field theory and electronic structure calculations with adjustable cluster base. *Physical Review B*, 75(15):155113, 2007.

[HBR+08] H. Hafermann, S. Brener, A. N. Rubtsov, M. I. Katsnelson, and A. I. Lichtenstein. Cluster dual fermion approach to nonlocal correlations. *JETP letters*, 86(10):677–682, 2008.

[HBS+14] C. Heil, L. Boeri, H. Sormann, W. von der Linden, and M. Aichhorn. Effect of the iron valence in the two types of layers in $LiFeO_2Fe_2Se_2$. *Physical Review B*, 90(16):165122, Oct 2014.

[HD12] L. Huang and L. Du. Kernel polynomial representation of imaginary-time green's functions. *arXiv preprint arXiv:1205.2791*, 2012.

[HKL09] H. Hafermann, M. I. Katsnelson, and A. I. Lichtenstein. Metal-insulator transition by suppression of spin fluctuations. *EPL (Europhysics Letters)*, 85(3):37006, 2009.

[HLR+09] H. Hafermann, G. Li, A. N. Rubtsov, M. I. Katsnelson, A. I. Lichtenstein, and H. Monien. Efficient perturbation theory for quantum lattice models. *Physical Review Letters*, 102(20):206401, 2009.

[HPW12] H. Hafermann, K. R. Patton, and P. Werner. Improved estimators for the self-energy and vertex function in hybridization-expansion continuous-time quantum Monte Carlo simulations. *Physical Review B*, 85(20):205106, 2012.

[HRZ13] J.-W. Huo, T. M. Rice, and F.-C. Zhang. Spin density wave fluctuations and p-wave pairing in Sr_2RuO_4. *Physical Review Letters*, 110(16):167003, 2013.

[HvLK+14] H. Hafermann, E. G. C. P. van Loon, M. I. Katsnelson, A. I. Lichtenstein, and O. Parcollet. Collective charge excitations of strongly correlated electrons, vertex corrections, and gauge invariance. *Physical Review B*, 90(23):235105, Dec 2014.

[HW12] L. Huang and Y. Wang. Dynamical screening in strongly correlated metal $SrVO_3$. *EPL (Europhysics Letters)*, 99(6):67003, 2012.

[HWD12] L. Huang, Y. Wang, and X. Dai. Pressure-driven orbital selective insulator-to-metal transition and spin-state crossover in cubic CoO. *Physical Review B*, 85(24):245110, 2012.

[HWW14] L. Huang, T. O. Wehling, and P. Werner. Electronic excitation spectra of the five-orbital Anderson impurity model: From the atomic limit to itinerant atomic magnetism. *Physical Review B*, 89(24):245104, 2014.

[IKK+11] K. Iida, M. Kofu, N. Katayama, J. Lee, R. Kajimoto, Y. Inamura, M. Nakamura, M. Arai, Y. Yoshida, M. Fujita, et al. Inelastic neutron scattering study of the magnetic fluctuations in Sr_2RuO_4. *Physical Review B*, 84(6):060402, 2011.

[Jar92] M. Jarrell. Hubbard model in infinite dimensions: A quantum Monte Carlo study. *Physical Review Letters*, 69(1):168, 1992.

[JMHM01] M. Jarrell, T. Maier, C. Huscroft, and S. Moukouri. Quantum Monte Carlo algorithm for nonlocal corrections to the dynamical mean-field approximation. *Physical Review B*, 64(19):195130, 2001.

[KA14] J. Kuneš and P. Augustinskỳ. Excitonic instability at the spin-state transition in the two-band Hubbard model. *Physical Review B*, 89(11):115134, 2014.

[KL10] M. I. Katsnelson and A. I. Lichtenstein. Theory of optically forbidden d–d transitions in strongly correlated crystals. *Journal of Physics: Condensed Matter*, 22(38):382201, 2010.

[Koh99] W. Kohn. Nobel lecture: Electronic structure of matter-wave functions and density functionals. *Reviews of Modern Physics*, 71:1253–1266, Oct 1999.

[KR12] I. S. Krivenko and A. N. Rubtsov. Analysis of the nature of the peak structure of Hubbard subbands using the quantum Monte Carlo method. *JETP letters*, 94(10):768–773, 2012.

[KSH+06] G. Kotliar, S. Y. Savrasov, K. Haule, V. S. Oudovenko, O. Parcollet, and C. A. Marianetti. Electronic structure calculations with dynamical mean-field theory. *Reviews of Modern Physics*, 78(3):865, 2006.

[KUH+09] N. Katayama, M. Uchida, D. Hashizume, S. Niitaka, J. Matsuno, D. Matsumura, Y. Nishihata, J. Mizuki, N. Takeshita, A. Gauzzi, et al. Anomalous metallic

state in the vicinity of metal to valence-bond solid insulator transition in $LiVS_2$. *Physical Review Letters*, 103(14):146405, 2009.

[Kun11] J. Kuneš. Efficient treatment of two-particle vertices in dynamical mean-field theory. *Physical Review B*, 83(8):085102, 2011.

[KW12] A. Koga and P. Werner. Dynamical properties of ultracold fermions with attractive interactions in an optical lattice. In *Journal of Physics: Conference Series*, volume 391, page 012144. IOP Publishing, 2012.

[LA11] D. J. Luitz and F. F. Assaad. Calculation of dynamical susceptibilities in the 2d Hubbard model: A dynamical cluster approach study. Frühjahrstagung der Deutschen Physikalischen Gesellschaft, 2011.

[LBA+08] G. Lang, J. Bobroff, H. Alloul, G. Collin, and N. Blanchard. Spin correlations and cobalt charge states: Phase diagram of sodium cobaltates. *Physical Review B*, 78(15):155116, 2008.

[LK98] A. I. Lichtenstein and M. I. Katsnelson. Ab initio calculations of quasiparticle band structure in correlated systems: LDA++ approach. *Physical Review B*, 57(12):6884, 1998.

[LLFH11] G. Li, M. Laubach, A. Fleszar, and W. Hanke. Geometrical frustration and the competing phases of the Sn/Si (111) 3×3 R 30° surface systems. *Physical Review B*, 83(4):041104, 2011.

[LLM08] G. Li, H. Lee, and H. Monien. Determination of the lattice susceptibility within the dual fermion method. *Physical Review B*, 78(19):195105, 2008.

[Lui11] David Luitz. private communication, 2011.

[MAM+11] J. Mravlje, M. Aichhorn, T. Miyake, K. Haule, G. Kotliar, and A. Georges. Coherence-incoherence crossover and the mass-renormalization puzzles in Sr_2RuO_4. *Physical Review Letters*, 106(9):096401, 2011.

[MELFed] B. Meyer, C. Elsässer, F. Lechermann, and M. Fähnle. *FORTRAN 90 Program for Mixed-Basis-Pseudopotential Calculations for Crystals*. Max-Planck-Institut für Metallforschung, Stuttgart, unpublished.

[MHY+94] Y. Maeno, H. Hashimoto, K. Yoshida, S. Nishizaki, T. Fujita, J. G. Bednorz, and F. Lichtenberg. Superconductivity in a layered perovskite without copper. *Nature*, 372(6506):532–534, 1994.

[MJPH05] T. Maier, M. Jarrell, T. Pruschke, and M. H. Hettler. Quantum cluster theories. *Reviews of Modern Physics*, 77(3):1027, 2005.

[MK07] C. A. Marianetti and G. Kotliar. Na-induced correlations in Na_xCoO_2. *Physical Review Letters*, 98(17):176405, 2007.

[MS99] I. I. Mazin and D. J. Singh. Competitions in layered ruthenates: ferromagnetism versus antiferromagnetism and triplet versus singlet pairing. *Physical Review Letters*, 82(21):4324, 1999.

[MV89] W. Metzner and D. Vollhardt. Correlated lattice fermions in $d = \infty$ dimensions. *Physical Review Letters*, 62(3):324, 1989.

[MV97] N. Marzari and D. Vanderbilt. Maximally localized generalized Wannier functions for composite energy bands. *Physical review B*, 56(20):12847, 1997.

[NA14] M. Nuss and M. Aichhorn. Effective model for the electronic properties of quasi-one-dimensional purple bronze $Li_{0.9}Mo_6O_{17}$ based on ab initio calculations. *Physical Review B*, 89(4):045125, 2014.

[NAAvdL12] M. Nuss, E. Arrigoni, M. Aichhorn, and W. von der Linden. Variational cluster approach to the single-impurity Anderson model. *Physical Review B*, 85(23):235107, 2012.

[NS00] K.-K. Ng and M. Sigrist. Anisotropy of the spin susceptibility in the normal state of Sr_2RuO_4. *Journal of the Physical Society of Japan*, 69(11):3764–3765, 2000.

[NSA14] Y. Nomura, S. Sakai, and R. Arita. Multiorbital cluster dynamical mean-field theory with an improved continuous-time quantum Monte Carlo algorithm. *Physical Review B*, 89(19):195146, 2014.

[Pav14] Eva Pavarini. Linear response functions. In E. Pavarini, E. Koch, V. Vollhardt, and A. I. Lichtenstein, editors, *DMFT at 25: Infinite Dimensions*, volume 4 of *Modelling and Simulation*, chapter 6. Forschungszentrum Jülich GmbH, 2014.

[PW92] J. P. Perdew and Y. Wang. Accurate and simple analytic representation of the electron-gas correlation energy. *Physical Review B*, 45(23):13244, 1992.

[R.13] Achim R. Summary: Phenomenology. Korrelationstage 2013, Dresden, 2013.

[RKL08] A. N. Rubtsov, M. I. Katsnelson, and A. I. Lichtenstein. Dual fermion approach to nonlocal correlations in the Hubbard model. *Physical Review B*, 77(3):033101, 2008.

[RKLG09] A. N. Rubtsov, M. I. Katsnelson, A. I. Lichtenstein, and A. Georges. Dual fermion approach to the two-dimensional Hubbard model: Antiferromagnetic fluctuations and Fermi arcs. *Physical Review B*, 79(4):045133, 2009.

[RVT12] G. Rohringer, A. Valli, and A. Toschi. Local electronic correlation at the two-particle level. *Physical Review B*, 86(12):125114, 2012.

[SBB+99] Y. Sidis, M. Braden, P. Bourges, B. Hennion, S. NishiZaki, Y. Maeno, and Y. Mori. Evidence for incommensurate spin fluctuations in Sr_2RuO_4. *Physical Review Letters*, 83(16):3320, 1999.

[SFP+09] P. Steffens, J. Farrell, S. Price, A. P. Mackenzie, Y. Sidis, K. Schmalzl, and M. Braden. Incommensurate magnetic ordering in Ti-doped $Sr_3Ru_2O_7$. *Physical Review B*, 79(5):054422, 2009.

[SFS+11] P. Steffens, O. Friedt, Y. Sidis, P. Link, J. Kulda, K. Schmalzl, S. Nakatsuji, and M. Braden. Magnetic excitations in the metallic single-layer ruthenates $Ca_{2-x}Sr_xRuO_4$ studied by inelastic neutron scattering. *Physical Review B*, 83(5):054429, 2011.

[SH14] A. Sotnikov and W. Hofstetter. Magnetic ordering of three-component ultracold fermionic mixtures in optical lattices. *Physical Review A*, 89(6):063601, 2014.

[SYŞ+13] H. Sims, E. R. Ylvisaker, E. Şaşıoğlu, C. Friedrich, S. Blügel, and W. E. Pickett. Effect of local electron-

electron correlation in hydrogen-like impurities in Ge. *Physical Review B*, 87(19):195120, 2013.

[TKH07] A. Toschi, A. A. Katanin, and K. Held. Dynamical vertex approximation: A step beyond dynamical mean-field theory. *Physical Review B*, 75(4):045118, 2007.

[VS77] H. J. Vidberg and J. W. Serene. Solving the Eliashberg equations by means of N-point Padé approximants. *Journal of Low Temperature Physics*, 29(3-4):179–192, 1977.

[WCD+06] P. Werner, A. Comanac, L. De'Medici, M. Troyer, and A. J. Millis. Continuous-time solver for quantum impurity models. *Physical Review Letters*, 97(7):076405, 2006.

[WL93] Le. Walz and F. Lichtenberg. Refinement of the structure of Sr_2RuO_4 with 100 and 295 K X-ray data. *Acta Crystallographica Section C: Crystal Structure Communications*, 49(7):1268–1270, 1993.

[WLH+14] A. Wilhelm, F. Lechermann, H. Hafermann, M. I. Katsnelson, and A. I. Lichtenstein. From Hubbard bands to spin-polaron excitations in the doped Mott material Na_xCoO_2. *arXiv preprint arXiv:1408.2152*, 2014.

[WM06] P. Werner and A. J. Millis. Hybridization expansion impurity solver: General formulation and application to Kondo lattice and two-orbital models. *Physical Review B*, 74(15):155107, 2006.

[WTSH11] P. Wissgott, A. Toschi, G. Sangiovanni, and K. Held. Effects of electronic correlations and disorder on the thermopower of Na_xCoO_2. *Physical Review B*, 84(8):085129, 2011.

[XRvR+13] N. Xu, P. Richard, A. van Roekeghem, P. Zhang, H. Miao, W.-L. Zhang, T. Qian, M. Ferrero, A. S. Sefat, S. Biermann, et al. Electronic band structure of $BaCo_2As_2$: A fully doped ferropnictide analog with reduced electronic correlations. *Physical Review X*, 3(1):011006, 2013.

[ZH90] V. Zlatic and B. Horvatic. The local approximation for correlated systems on high dimensional lattices. *Solid State Communications*, 75(3):263–267, 1990.

Danksagung/Acknowledgments

First of all I'd like to thank my supervisor, Frank Lechermann, for coming up with this interesting research proposition, insisting on the focus on realistic applications and providing me with organizational and personal means to fulfill this task. I'd like to thank Alexander Lichtenstein and Michael Potthoff for many valuable discussions and scientific input.

I'd like to thank Michel Ferrero and Olivier Parcollet for providing the TRIQS-code that was the base for most developments and calculations presented here and for collaborating on the Legendre basis project, that enabled the subsequent projects. Also, I'd like to thank Hartmut Hafermann who joined in to that project just at the right time to contribute his ideas and work.

I'd like to thank Alexander Lichtenstein and Mikhail Katsnelson for their support and discussions on $LiVS_2$ who contributed physical insight from their far reaching experience with quantum magnetism.

I'd like to thank Christoph Piefke and Hugo Strand for proofreading parts of this thesis.

Ich danke der Forschergruppe 1346 "Dynamical Mean-Field Approach with Predictive Power for Strongly Correlated Materials" der Deutschen Forschungsgemeinschaft nicht nur für die finanzielle Unterstützung meiner Dissertationszeit sondern besonders auch für die Veranstaltung mehrerer Herbstschulen, Klausurtagungen und Konferenzen, die eine große Hilfe dabei waren, den weiteren Blick um die spezielle Aufgabe zu erhalten. Ich danke dem Norddeutschen Verbund

für Hoch- und Höchstleistungsrechner (HLRN) für das Bereitstellen der erheblichen Rechenkapazitäten, ohne die ein Großteil der numerischen Arbeit nicht hätte stattfinden können.

Ich danke meinen Kollegen in Hamburg, allen voran Christoph Piefke. Es war mir eine Ehre, absurde Ideen und die Welt zu diskutieren. Außerdem danke ich Daniel Grieger, der leider viel zu früh die Gruppe ins Ausland verlassen hat. Ohne ihn lief vieles unrunder. Ich danke Malte Behrmann, Alexander Hampel, Michael Obermayer und Sergej Schuwalow für eine wertvolle Arbeitsumgebung und vieles persönliches darüber hinaus. Und ich danke Raphael Richter, der einen Teil meiner Arbeit in Hamburg fortsetzen wird. Außerdem danke ich Maximilian Aulbach, Mohammad Sayad, Daniel Hirschmeier, Burkhard Sachs, Aljoscha Wilhelm, Friedrich Krien, Maria Valentyuk, Malte Harland, Sergey Brener und Igor Krivenko für die verschiedensten physikalischen und nicht physikalischen Diskussionen.

Ich danke Bodo Krause-Kyora und Michael Vedmedenko dafür, dass immer alles funktioniert hat technisch oder schnell funktionierend gemacht wurde.

Ich danke meinen Eltern, die mich früh ans Entdecken herangeführt haben und eine Wertschätzung von Wissen vermitteln konnten und meinen Schwiegereltern, die mir viel Freiraum geschaffen haben, den ich mit dieser Dissertation ausfüllen konnte.

Ich danke Wilfried Marx und Kurt Scharnberg, die mir beide geholfen haben wissenschaftliche Themen für mich zu entdecken, wenn auch zu sehr unterschiedlichen Zeitpunkten meines Werdegangs.

Ich danke meinem Schwager Daniel Gruber, der als Nichtphysiker mit ehrlichem Interesse meine Dissertation gelesen und Ausdruck korrigiert hat.

Ich danke meinem Hund Kibo, der mich oft in das Institut begleitet hat und dann immer verlässlich darauf bestanden hat, dass man auch zu angemessener Zeit auf den heimischen Balkon wechseln kann.

Am meisten danke ich natürlich meiner Frau, Yuan, die mich immer, besonders auch in der Endphase$^{\mathrm{TM}}$ meiner Dissertation unterstützt hat.